ANTHROPOGENIC AND NATURAL NITROGEN OXIDES EMISSIONS OVER THE UNITED STATES: COMPREHENSIVE EVALUATIONS AND IMPLICATIONS FOR SURFACE OZONE PREDICTION

A Dissertation
Presented to
The Academic Faculty

By

Jianfeng Li

In Partial Fulfillment
Of the Requirements for the Degree
Doctor of Philosophy in the
School of Earth and Atmospheric Sciences

Georgia Institute of Technology

May 2019

ANTHROPOGENIC AND NATURAL NITROGEN OXIDES EMISSIONS OVER THE UNITED STATES: COMPREHENSIVE EVALUATIONS AND IMPLICATIONS FOR SURFACE OZONE PREDICTION

Approved by

Dr. Yuhang Wang, Advisor
School of Earth & Atmospheric Sciences
Georgia Institute of Technology

Dr. L. Greg Huey
School of Earth & Atmospheric Sciences
Georgia Institute of Technology

Dr. Rodney Weber
School of Earth & Atmospheric Sciences
Georgia Institute of Technology

Dr. Nga Lee Ng
School of Chemical & Biochemical Engineering
Georgia Institute of Technology

Dr. Jennifer Kaiser
School of Civil & Environmental Engineering
Georgia Institute of Technology

Date Approved: March 26, 2019

To my parents

ACKNOWLEDGEMENTS

I sincerely appreciate the tremendous support of many individuals during my Ph.D. degree studies.

I want to thank my advisor, Dr. Yuhang Wang, for his support and guidance with his scientific enthusiasm throughout my Ph.D. I appreciate my Ph.D. thesis committee members, Dr. Greg Huey, Dr. Rodney Weber, Dr. Nga Lee Ng, and Dr. Jennifer Kaiser, for their review of my thesis and for their comments and suggestions.

Thanks to all the current members and alumni of Dr. Yuhang Wang's group for their contributions to REAM development and help on scientific research and daily life. I enjoy my time working with Dr. Ziming Ke, Dr. Yufei Zou, Dr. Yuzhong Zhang, Dr. Yongjia Song, Dr. Ruixiong Zhang, Dr. Ye Cheng, Qiyang Yan, Hang Qu, Aoxing Zhang, and Kezhen Chong. Thank Dr. Dexian Chen — never forget the day when I first came to Atlanta, and you took me to the Westmar Lofts and Walmart.

My thesis is based on a large number of observations from other institutes. I want to thank Chun Zhao for providing the PNNL NEI2011 emission inventory, which is essentially the basis of all my studies. Thank Yuzhong Zhang and Jenny Fisher for providing the updated GEOS-Chem chemistry mechanism files. Thank Andrew J. Weinheimer from NCAR, Edward Celarier and Jay Herman from NASA, Raymon M. Hoff and Ruben Delgado from the University of Maryland, Anne M. Thompson from the Pennsylvania State University, Travis Knepp from the Science Systems and Applications,

Inc, Russell W. Long from EPA for providing measurements during the DISCOVER-AQ campaign. Thank Benjamin Wells, Alison Eyth, Lee Tooly from EPA, the EPA MOVES team, Betty Carter from COORDINATING RESEARCH COUNCIL, INC., Brain McDonald from NOAA, and Zhe Jiang from University of Science and Technology of China for helping me an understanding of the NEI MOVES mobile source emissions. Thank William Koshak from NASA for providing lightning observations.

Finally, I want to express my deepest gratitude to my parents for their continued support, endless love and encouragement.

TABLE OF CONTENTS

LIST OF TABLES

LIST OF FIGURES

LIST OF SYMBOLS AND ABBREVIATIONS

Symbols

c	concentrations
CH_2O/HCHO	formaldehyde
CO	carbon monoxide
CO_2	carbon dioxide
E	Emissions
HNO_3	nitric acid
HO_2	the hydroperoxyl radical
K_{zz}	eddy diffusivity coefficients
MoO_x	molybdenum oxide
N_2O_5	dinitrogen pentoxide
NO	nitric oxide
NO_2	nitrogen dioxide
NO_2*	Excited NO_2
NO_3	nitrate radical
NO_x	nitrogen oxides
NO_y	active nitrogen compounds
NO_z	non-NO_x active nitrogen compounds
O_3	ozone
OH	hydroxyl radical
PAN	peroxyacetyl nitrates

$P(O_3)$	O_3 production rate
RO_2	alkyl peroxy radicals
SO_2	sulfur dioxide
β	ratio of nitrogen oxides emission change to the change of nitrogen dioxide tropospheric vertical column densities
γ	ratio of nitrogen oxides emissions change to the change of nitrogen dioxide surface concentrations
Ω	vertical column densities

Abbreviations

AMF	Air Mass Factor
BEHR	Berkeley High-Resolution NO_2 tropospheric vertical column density products
BVOC	biogenic volatile organic compounds
CAMS	the Compact Atmospheric Multispecies Spectrometer
CAPE	convective available potential energy
CAPS	Cavity Attenuated Phase Shift Spectroscopy
CEMS	Continuous Emission Monitoring Systems
CFSv2	the NCEP coupled forecast system model version 2 products
CG	Cloud-Ground lightning
CMAQ	the Community Multiscale Air Quality
CONCEPT MV	CONsolidated Community Emissions Processor Tool, Motor Vehicle
DISCOVER-AQ	Deriving Information on Surface conditions from Column and Vertically Resolved Observations Relevant to Air Quality

DMF	downdraft mass flux
DOAS	Differential Optical Absorption Spectroscopy
DOMINO	Dutch OMI NO_2 product
ELF	the Elastic Lidar Facility
EPA	the Environmental Protection Agency
FEM	Federal Equivalent Method
FRM	Federal Reference Method
GMI	the Global Modeling Initiative model
GEOS-Chem	a global 3-D model
GOME-2	Global Ozone Monitoring Experiment – 2
GOME-2A	Global Ozone Monitoring Experiment – 2 aboard METOP-A
GOME-2B	Global Ozone Monitoring Experiment – 2 aboard METOP-B
HDT	heavy-duty trucks
IC	Intra-Cloud lightning
IMAGESv2	the Intermediate Model of Global Evolution of Species version 2
INTEX-A	the Intercontinental Chemical Transport Experiment North America campaign
KF	Kain-Fritsch convection scheme
KNMI	the Royal Netherlands Meteorological Institute
LAI	Leaf Area Index
LDV	low-duty vehicles
LT	Local time
MAX-DOAS	Multi Axis Differential Optical Absorption Spectroscopy
MCMA	the Mexico City Metropolitan Area

MDA8	Maximum daily 8-hour average ozone mixing ratio
MEGAN	the Model of Emissions of Gases and Aerosols from Nature
MOD09A1	MODIS land surface reflectance product
MODIS	Moderate Resolution Imaging Spectroradiometer
MOVES	Motor Vehicle Emissions Simulator
NASA	the National Aeronautics and Space Administration
NATIVE	Nittany Atmospheric Trailer and Integrated Validation Experiment
NCAR	The US National Center for Atmospheric Research
NCEP	National Centers for Environmental Prediction
NEI2008	the 2008 National Emission inventory
NEI2011	the 2011 National Emission inventory
NEI2014	the 2014 National Emission inventory
NLDN	National Lightning Detection Network
NOAA	the National Oceanic and Atmospheric Administration
OMI	the Ozone Monitoring Instrument
OMNO2	the Aura Ozone Monitoring Instrument Nitrogen Dioxide Standard Product
PANDORA	the Pandora Spectrophotometer
PBL	Planetary boundary layer
PBLH	Planetary boundary layer height
PNNL	the Pacific Northwest National Laboratory
QA4ECV	Quality Assurance for Essential Climate Variables
RCI	Relative Confidence Interval
SCIAMAHCY	SCanning Imaging Absorption SpectroMeter for

	Atmospheric CHartography
SCD	slant column densities
SEAC^{4}RS	Studies of Emissions, Atmospheric Composition, Clouds and Climate Coupling by Regional Surveys
SMOKE	Sparse Matrix Operator Kernel Emissions
SZA	solar zenith angle
TKE	Turbulent Kinetic Energy
TM4	the Tracer Model, version 4
TM5-MP	a new version of the Tracer Model version 5
TVCD	tropospheric vertical column densities
UMF	updraft mass flux
VCD	vertical column densities
VMR	Volume Mixing Ratio
WRF	the Weather Research and Forecasting model
YL	the Yienger and Levy soil NO_x emission scheme
YSU	Yonsei University planetary boundary layer scheme

SUMMARY

Nitrogen oxides (NO_x = NO + NO_2) play a crucial role in the formation of ozone and has significant impacts on the production of secondary organic and inorganic aerosols, thus affecting human health, global radiation budget, and climate. Accurate knowledge of NO_x emissions is essential for relevant scientific research and air pollution control policies. This thesis evaluates current estimates of anthropogenic and natural NO_x emissions over the United States and improves model's prediction of surface ozone concentrations by using a 3-D Regional chEmistry and trAnsport Model (REAM) and various types of observations and investigate the impact of thunderstorms on surface NO_x and O_3 concentrations.

The diurnal cycle of NO_2 is a function of emissions, advection, deposition, vertical mixing, and chemistry. Its observations, therefore, provide useful constraints in our understanding of these factors. The REAM simulated diurnal cycles are evaluated by using the DISCOVER-AQ campaign measurements, EPA Air Quality System (AQS) observations, and OMI and GOME-2A tropospheric vertical column densities (TVCDs) products in July 2011 over the Baltimore-Washington region. The model simulations are in reasonably good agreement with the observations except that PANDORA measured NO_2 TVCD show much less variation in the early morning and late afternoon than simulated in the model. High resolution (4 km in the horizontal) model simulations are also performed to examine the effects of emission distributions. The overestimation of NO_2 concentrations from the 4-km REAM simulation in contrast to the well reproduction

of observations by the 36-km REAM suggests that the 2011 National Emission Inventory (NEI2011) provide a good estimate of NO_x emissions at the 36-km scale but can't resolve NO_x emission distributions at the 4-km resolution. By analyzing model simulations with the observations, the thesis shows that the diurnal emission profile of NO_x is different over the weekend from the weekdays and that weekend emissions are about 1/3 lower than weekdays.

Observed ozone concentrations can be used to evaluate NO_x and volatile organic compound (VOC) emissions by using their relationships with ozone concentrations. The thesis shows that the time when ozone reaches its daily maximum (peak time) is also related to NO_x and VOC emissions. Through model sensitivity analyses of REAM in July 2011 over the contiguous United States (CONUS), it is found that ozone peak values are more sensitive to NO_x emissions while ozone peak time is more sensitive to VOC emissions in the eastern United States. By such relationships and the comparison between observations and model results, we find that the underestimation of soil NO_x emissions leads to a low bias of simulated ozone peak value in the South, while the overestimation of biogenic isoprene emissions results in earlier than observed ozone peak time in the Central, South and Southeast regions. The simulated formaldehyde columns, which are higher than satellite measurements, confirm the latter.

We illustrate the nonlinear relationships among NO_x emissions, NO_2 TVCDs, and NO_2 surface concentrations using the simulations of REAM for July 2011 over the CONUS. The variations of NO_2 surface concentrations and TVCDs are generally consistent and reflect well anthropogenic NO_x emission variations for high-NO_x emission

regions. For low-NO_x emission regions, however, nonlinearity in the emission-TVCD relationship makes it difficult to use satellite observations to infer anthropogenic NO_x emission changes. The analysis is extended to 2003 – 2017. Similar variations of NO_2 surface measurements and coincident satellite NO_2 TVCDs over urban regions are in sharp contrast to the large variation differences between surface and satellite observations over rural regions. We find a continuous decrease of anthropogenic NO_x emissions after 2011 by examining surface and satellite measurements in CONUS urban regions, but the decreasing rate is lower by 9% - 46% than the pre-2011 period.

By comparing observed ΔO_3 (hourly change of O_3 concentrations) and ΔNO_x with/without lightning events, we find that generally, thunderstorms decreased ΔO_3 in the daytime due to the dominant role of solar radiation reduction reaching the surface and increased ΔO_3 during the nighttime due to convective downdrafts and increased nocturnal boundary layer mixing. With our adjustment of downdraft mass fluxes (DMFs) and eddy diffusivity coefficients during nighttime thunderstorm events which are underestimated by the Weather Research Forecast (WRF) model, REAM well reproduces the observed characteristics and produces a bimodal post-convection lightning NO_x shape with one peak near the surface. Sensitivity simulations show that lightning NO_x contributes 2.4 – 3.6 ppb to MDA8 in the southeast U.S.

CHAPTER 1. INTRODUCTION

1.1 Overview

Nitrogen oxides ($NO_x = NO_2 + NO$) are among the most important trace gases in the atmosphere, not only because of their direct detrimental impact on human respiratory systems [*Greenberg et al.*, 2016; *Greenberg et al.*, 2017; *Heinrich et al.*, 2013; *Weinmayr et al.*, 2009], but also their fundamental roles in the formation of ozone, acid rain, and fine particles which are unfavorable to human health, ecosystem stabilities, and climate change [*Crouse et al.*, 2015; *Fisher et al.*, 2016; *Kampa and Castanas*, 2008; *Liu et al.*, 2012a; *Myhre et al.*, 2013; *Ng et al.*, 2017; *Pandey et al.*, 2005; *Peng et al.*, 2016; *Seinfeld and Pandis*, 2016; *Singh and Agrawal*, 2007]. NO_x is emitted by both anthropogenic and natural sources with a global estimate of 48.8 Tg N yr^{-1}, of which about 77% are from human activities, including 28.3 Tg N yr^{-1} from fossil fuel combustion and industrial processes, 3.7 Tg N yr^{-1} from agriculture activities, and 5.5 Tg N yr^{-1} from biomass and biofuel burning [*Seinfeld and Pandis*, 2016]. Soil and lightning contribute to the rest 23% of the global NO_x emissions.

United States is usually a high-NO_x emission region, especially for urban regions, suffering from surface O_3 pollutions and photochemical smog raised by NO_x. Since the regulations of the Environmental Protection Agency (EPA) on emission standards in the 1990s, U.S. NO_x emissions have reduced by over 50% [*EPA*, 2018]. On the basis of the 2014 National Emission Inventory (NEI2014), 3.85 Tg N and 0.24 Tg N of anthropogenic and natural NO_x, respectively, were emitted from the U.S. in 2014.

However, recent studies excite broad concerns about the accuracy of NEI NO_x emissions. *Anderson et al.* [2014], *Canty et al.* [2015], and *Travis et al.* [2016] suggested that on-road mobile sources in the NEI NO_x emissions inventories were overestimated by around 50% - 70% in 2007 and 2011 through analyses of surface, aircraft, and satellite measurements. *McDonald et al.* [2018] also found the overestimation of NEI mobile NO_x emissions compared to their estimates based on fuel consumptions. Conversely, *Dallmann and Harley* [2010] suggested that on-road mobile NO_x emissions from NEI2005 were 15% lower than fuel-derived on-road NO_x emissions. Moreover, *Salmon et al.* [2018] examined the NO_x/CO_2, CO/CO_2, and CO/NO_x ratios during the Wintertime INvestigation of Transport, Emissions, and Reactivity (WINTER) campaign in February-March 2015 over the northeastern United States and found that NO_x emissions from NEI2011 and NEI2014 were in agreement with the aircraft observation-derived emissions.

On the other hand, *Miyazaki et al.* [2017] and *Jiang et al.* [2018] found that the U.S. NO_x emissions derived from satellite NO_2 tropospheric vertical column densities (TVCDs), including OMI (the Ozone Monitoring Instrument), SCIAMACHY (SCanning Imaging Absorption SpectroMeter for Atmospheric CHartography), and GOME-2A (Global Ozone Monitoring Experiment – 2 onboard METOP-A), were almost flat from 2010 - 2015 and suggested that the decrease of NO_x emissions was only significant before 2010. However, EPA NO_x emission trend datasets [*EPA*, 2018] show a continuous decrease of NO_x emissions after 2010. And, fuel-based emission estimates in Los Angeles also showed a steady decrease of NO_x emissions after 2000 and a small impact of the Great Recession (from December 2007 to June 2009) on NO_x emission decrease

trend [*Hassler et al.*, 2016]. The ongoing reduction of vehicle exhaust emission factors [*McDonald et al.*, 2018] was another supporter for the continuous decrease of U.S. NO_x emissions.

Considering the importance of accurate knowledge of NO_x emissions on relevant scientific research and the implementation of air quality policies, it is urgent to evaluate U.S. NO_x emissions comprehensively with more datasets and approaches, which is the primary goal of this thesis (**Chapter 2** – **Chapter 4**).

As anthropogenic NO_x emissions continue decreasing on the basis of EPA datasets [*EPA*, 2018], natural sources play a more and more important role on regulating surface NO_x and O_3 concentrations, especially over rural regions. Unlike soil NO_x emissions which are emitted near the surface and play a similar chemical role as anthropogenic NO_x emissions, lightning NO_x, associated with thunderstorms (deep convection), play a distinct but crucial role in tropospheric chemistry and climate due to their direct emissions of lightning NO_x, their key impact on pollutant re-distributions in the atmosphere, and the effect of cumulus clouds on solar radiance balance. Lightning NO_x, with annual global emissions of 2 – 8 Tg N [*Huntrieser et al.*, 2002; *Miyazaki et al.*, 2014; *Schumann and Huntrieser*, 2007; *Seinfeld and Pandis*, 2016], is the primary source of upper tropospheric NO_x [*S. Choi et al.*, 2014], which contributed to 60% - 75% of summertime 300 hPa NO_x over the eastern United States during 2004 – 2006 [*Allen et al.*, 2010; *C. Zhao et al.*, 2009a] and about 40% of total reactive odd nitrogen (NO_y) in the northern midlatitude (30°N) upper troposphere (500 hPa – 200 hPa) from 1990 – 1999 [*Grewe*, 2007], and 19% - 31% (15 – 24 ppbv) of upper tropospheric O_3 over the eastern United States in the summer

[*Allen et al.*, 2010; *Allen et al.*, 2012; *Grewe*, 2007; *L. Wang et al.*, 2013; *C. Zhao et al.*, 2009a].

Updrafts and downdrafts from thunderstorms are important factors redistributing air pollutants in the troposphere. On the one hand, pollutants and ozone precursors in the boundary layer, such as NO_x, volatile organic compounds (VOC), and CO, can be transported to upper troposphere by convective updrafts [*Dickerson et al.*, 1987; *Huntrieser et al.*, 2002]. On the other hand, convective downdrafts transport air with lightning NO_x and high-O_3 concentrations in the upper troposphere to the lower troposphere [*Luo et al.*, 2017; *Ott et al.*, 2010], which may affect surface NO_x and O_3 concentrations [*Allen et al.*, 2012; *Bharali et al.*, 2015; *Kar and Liou*, 2014]. However, the impacts of thunderstorms on surface NO_x and O_3 are much smaller than on upper troposphere and highly uncertain. Previous studies focused on the contribution of lightning NO_x to surface NO_x and O_3 but ignored the contribution of downdrafts [*Allen et al.*, 2012; *Koshak et al.*, 2014]. As an expected continuous decrease of anthropogenic NO_x emissions and a projected increase of lighting activities and severe thunderstorms [*Diffenbaugh et al.*, 2013; *Romps et al.*, 2014], the impacts of thunderstorms on surface NO_x and O_3 concentrations would be expected to be more and more significant. Therefore, it is necessary to investigate the effect of thunderstorm downdraft on surface NO_x and O_3 and improve our understanding of the impact of thunderstorms on surface NO_x and O_3, which is the second goal of this thesis (**Chapter 5**).

1.2 Outline of the thesis

Chapter 1 introduces the background and motivations of this study. The purpose of this thesis is to evaluate current estimates of anthropogenic and natural NO_x emissions over the United States and investigate the effect of thunderstorms on surface NO_x and O_3 by using a 3-D Regional chEmistry and trAnsport Model (REAM) and various types of observations.

Chapter 2 examines the diurnal cycles of surface NO_2 concentrations, NO_2 vertical profiles, and NO_2 TVCDs in July 2011 over the Baltimore-Washington, D.C. region. The REAM simulated diurnal cycles on weekdays and weekends at 36-km and 4-km scales are evaluated with surface, aircraft, and satellite measurements from the 2011 DISCOVER-AQ (Deriving Information on Surface conditions from Column and Vertically Resolved Observations Relevant to Air Quality) campaign. We find that REAM reproduces well the observations at the 36-km scale but overestimates NO_2 concentrations and TVCD at the 4-km scale, which means NEI2011 provide reasonable estimates of anthropogenic NO_x emissions at the 36-km scale but is unable to resolve the NO_x emission distributions at the 4-km scale.

Chapter 3 extended the 36-km evaluation of NO_x emissions to the contiguous United States (CONUS) through comparisons of simulated and observed O_3 peak values and peak time in July 2011. Through REAM sensitivity simulations with different NO_x and VOC emission scenarios, we find that VOC and NO_x emissions affect O_3 peak time oppositely over the eastern United States and O_3 peak time provides another independent constraint on NO_x emission evaluations. Comparisons of simulated and observed O_3 peak values and

peak time show that NEI2011 provides good estimates of anthropogenic NO_x emissions over the CONUS but soil NO_x emissions from the Yienger and Levy (YL) scheme are underestimated, and biogenic isoprene emissions from the Model of Emissions of Gases and Aerosols from Nature (MEGAN) are overestimated by 27.1% ± 21.5%.

Chapter 4 investigates the anthropogenic NO_x emission trend from 2003 – 2017 by using NO_2 surface measurements and satellite TVCD datasets. By examining the nonlinear relationships among NO_x emissions, NO_2 TVCDs, and NO_2 surface concentrations using the REAM simulations for July 2011 over the CONUS and NO_2 surface and coincident satellite measurements from 2003 - 2017, we find that satellite NO_2 TVCDs provide much better information of anthropogenic NO_x emission variations over urban than rural regions. And, NO_2 surface observations, satellite TVCD datasets, and updated EPA NO_x emissions show consistent variations from 2003 – 2017 over the urban regions of CONUS, which confirms the continuous decrease of anthropogenic NO_x emissions after 2011 but with the decreasing rate slowing down by 9% - 46% than the pre-2011 period.

Chapter 5 explores the impacts of thunderstorms and lightning NO_x on surface O_3 concentrations through comparisons of ΔNO_x and ΔO_3 (the hourly change of NO_x and O_3 concentrations) with/without lightning events during June – August in 2011. We find that thunderstorms generally decrease ΔO_3 in the daytime but increase ΔO_3 during the nighttime. REAM captures the decrease of ΔO_3 in the daytime but fails to reproduce the nighttime increase characteristics due to underestimated downdraft mass fluxes (DMFs) from the Kain-Fritsch (KF) scheme and the missing of mechanical vertical mixing induced by thunderstorms during the nighttime. The REAM simulation with updated DMFs and

nighttime vertical mixing reproduce well the observed thunderstorm features of ΔO_3. With the updated DMFs, REAM produces a bimodal post-convection lightning NO_x profile with one peak near the surface in contrast to a previous unimodal post-convection profile peaking at about 6-km. The adjusted DMFs significantly improve (by about 100%) the impact of thunderstorms/lightning NO_x on MDA8 (maximum daily 8-hour average O_3 concentrations) over the CONUS, especially in Arizona, Utah, and the southeastern United States.

Chapter 6 gives a summary of the study and recommendations for future research.

CHAPTER 2. Diurnal cycles of NO_2 during DISCOVER-AQ 2011: Comprehensive evaluations and implications for NO_x emissions

2.1 Introduction

Nitrogen oxides (NO_x = NO + NO_2) are among the most important trace gases in the atmosphere as their crucial role in the formation of ozone (O_3) and secondary aerosols and their involved in the chemical transformation of other atmospheric species, such as carbon monoxide (CO) and volatile organic compounds (VOC) [*Fisher et al.*, 2016; *Liu et al.*, 2012a; *Ng et al.*, 2017; *Peng et al.*, 2016; *Seinfeld and Pandis*, 2016]. NO_x is emitted by both anthropogenic activities and natural sources. Anthropogenic sources account for about 77% of the total NO_x emissions, and fossil fuel combustion and industrial processes are the primary anthropogenic sources which contribute to about 75% of the anthropogenic emissions [*Seinfeld and Pandis*, 2016]. Other important anthropogenic sources include agriculture and biomass and biofuel burning. Soils and lightning are two major natural emitters. Most NO_x is emitted as NO, which is then easily oxidized to NO_2 by oxidants, such as O_3, the hydroperoxyl radical (HO_2), and alkyl peroxy radicals (RO_2).

The diurnal variations of NO_2, which are controlled by continuous comprehensive physical and chemical processes, conversely reflect the temporal patterns of these underlying factors, such as NO_x emissions, chemistry, deposition, advection, diffusion, and convection. Therefore, the NO_2 diurnal cycles can be used to evaluate our understanding of NO_x related chemistry and physics processes, which has been widely

applied in researches. For example, *Jones et al.* [2000] investigate the diurnal cycles of NO and NO_2 and find that photochemistry-induced snowpack production may be a significant contributor to lowering troposphere NO_x in the Antarctic. *Frey et al.* [2013] show the asymmetry of the diurnal cycle of NO_2 with minimum concentrations at local noon on the Antarctic Plateau and indicate that strong convective mixing in the boundary layer induces the minimum NO_2 concentrations at noon. *Brown et al.* [2004] analysis the diurnal patterns of NO_3, NO_x, N_2O_5, HNO_3, OH, and O_3 and find that the predominant nighttime sink of NO_x through the hydrolysis of N_2O_5 has an efficiency on par with daytime photochemical conversion over the ocean surface off the New England coast. *Van Stratum et al.* [2012] show that entrainment and boundary layer growth in daytime influence NO_x diurnal cycles the same order as chemical transformations in Spain. *David and Nair* [2011] find that the diurnal pattern of NO_x at a tropical coastal station in India is closely associated with sea breeze and land breeze which affect the availability of NO_x through transport. They also think that seasonal monsoon can strongly influence the magnitude of NO_2 diurnal cycles through transport. The monsoon effect on NO_2 diurnal cycles is also observed in China by *Tu et al.* [2007].

Not only are surface NO_2 diurnal cycles concerned, but also the daily variations of NO_2 vertical column densities (VCD) are investigated. *Boersma et al.* [2008] compare NO_2 tropospheric VCD (TVCD) retrieved from OMI (the Ozone Monitoring Instrument) and SCIAMACHY (SCanning Imaging Absorption SpectroMeter for Atmospheric CHartography) around the world, and find that the diurnal patterns of different types of NO_x emissions can strongly affect the NO_2 TVCD variations between OMI and SCIAMACHY. They find that strong afternoon fire activity results in an increase of NO_2

TVCD from 10:00 LT (local time) to 13:30 LT over tropical biomass burning regions. *Boersma et al.* [2009] further investigate the NO_2 TVCD change from SCIAMACHY to OMI in different seasons in Israeli cities and find that: 1) there is a slight increase of NO_2 TVCD from SCIAMACHY to OMI in winter due to increased NO_x emissions from 10:00 LT to 13:30 LT and sufficiently weak photochemical sink; 2) the TVCD from OMI are lower than SCIAMACHY in summer due to strong photochemical sink of NO_x. All these above researches, however, are limited in observations, and they exploit only surface or satellite measurements. Comprehensive analyses of NO_2 diurnal cycles over the eastern United States are still unavailable.

DISCOVER-AQ (https://discover-aq.larc.nasa.gov/), which stands for Deriving Information on Surface conditions from Column and Vertically Resolved Observations Relevant to Air Quality, is a four-year project to enhance the understanding of the relationship between surface air pollutants and space observations. The first DISCOVER-AQ deployment was conducted in the Baltimore-Washington metropolitan region in the summer of 2011 (Figure 2.8.a). In this campaign, a NASA P-3B aircraft flew spirally over six air quality monitoring sites (Aldino, Edgewood, Beltsville, Essex, Fairhill, and Padonia) and the Chesapeake Bay [*Lamsal et al.*, 2014], and accomplished 244 valid measurements of NO_2 profiles on 14 flight days in July. Ground-based instruments below the mission spirals were deployed to measure NO_2 surface concentrations, NO_2 VCD, and other physical properties of the atmosphere [*Anderson et al.*, 2014; *A. J. Reed et al.*, 2015; *Sawamura et al.*, 2014]. Satellite NO_2 VCD products, OMI and GOME-2A (Global Ozone Monitoring Experiment – 2 aboard METOP-A), containing VCD information at13:30 LT (OMI) and 9:30 LT (GOME-2A), can be used to assess VCD measurements

from ground-based spectrometer systems — Pandora. With these simultaneous measurements of NO_2 VCD, surface NO_2, and vertically resolved distributions of NO_2 as they evolved throughout the day, the DISCOVER-AQ 2011 campaign, therefore, gives us a chance to evaluate NO_2 diurnal variabilities comprehensively.

Section 2.2 will describe the above datasets in detail. A Regional chEmistry and trAnsport Model (REAM), which will also be introduced in section 2.2, is applied to reproduce the NO_2 measurements during the DISCOVER-AQ campaign in July 2011. The evaluations of the simulated diurnal cycles of surface NO_2 concentrations, NO_2 vertical profiles, and NO_2 TVCD will be fully discussed in section 2.3 through comparison with observations. Section 2.3 will also investigate the differences between NO_2 diurnal cycles on weekdays and weekends and their applications to NO_x emission characteristics. Moreover, we will assess the impact of NO_x emission distributions on NO_2 diurnal cycles in section 2.3 through comparison between a 36-km resolution REAM simulation and a 4-km resolution REAM simulation. Finally, we will summarize the study in section 2.4.

2.2 Datasets and model description

2.2.1 REAM

REAM has been widely applied in many studies [*Alkuwari et al.*, 2013; *Cheng et al.*, 2017; *Cheng et al.*, 2018; *Y. Choi et al.*, 2008a; *Y. Choi et al.*, 2008b; *Gu et al.*, 2014; *Gu et al.*, 2013; *Koo et al.*, 2012; *Liu et al.*, 2014; *Liu et al.*, 2012b; *Yuhang Wang et al.*, 2007; *Q. Yang et al.*, 2011; *R. Zhang et al.*, 2017b; *R. Zhang et al.*, 2018; *Y. Zhang et al.*, 2016; *C. Zhao and Wang*, 2009; *C. Zhao et al.*, 2009a; *C. Zhao et al.*, 2010]. The model

has a horizontal resolution of 36 km and 30 vertical layers in the troposphere. Meteorology fields are from a Weather Research and Forecasting (WRF, version 3.6) model simulation with the Yonsei University (YSU) planetary boundary layer (PBL) scheme. The WRF simulation is initialized and constrained by the NCEP coupled forecast system model version 2 (CFSv2) products (http://rda.ucar.edu/datasets/ds094.0/) [*Saha et al.*, 2011]. The chemistry mechanism is based on GEOS-Chem v11.01 with updated aerosol uptake of isoprene nitrates [*Fisher et al.*, 2016]. A 2° × 2.5° GEOS-Chem simulation provides the chemistry boundary conditions and initiations. Anthropogenic emissions on weekdays are from the National Emission Inventory 2011 (NEI2011) from the Pacific Northwest National Laboratory (PNNL). The diurnal profile of weekday NO_x emissions in the DISCOVER-AQ campaign region (marked as six slate gray grids in Figure 2.8.b) is displayed in Figure 2.1, while the weekend emissions will be discussed in section 2.3.2. Biogenic VOC emissions are from MEGANv2.10 [*Guenther et al.*, 2012]. REAM simulates boundary layer mixing by using eddy diffusivity coefficients (named exchange coefficients in WRF) (k_{zz}, m/s^2), which reflects the impact of boundary layer stability on turbulent mixing [*Y. Zhang et al.*, 2016].

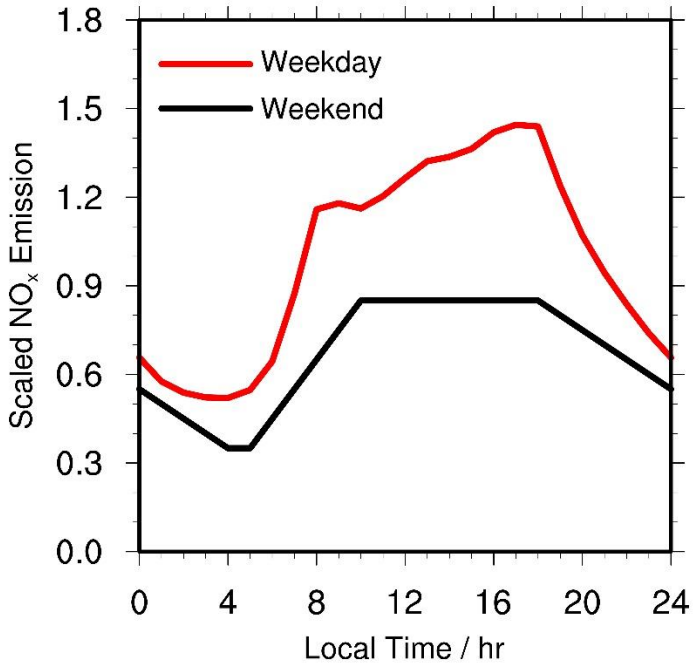

Figure 2. 1 Relative diurnal profiles of weekday and weekend NO_x emissions in the DISCOVER-AQ campaign region.

2.2.2 NO_2 TVCD from space — OMI and GOME-2A

The OMI instrument aboard the sun-synchronous NASA EOS Aura satellite with an equator-crossing time of around 13:45 LT, which was developed by the Finnish Meteorological Institute and the Netherlands Agency for Aerospace Programs, employs hyperspectral imaging to observe solar backscatter radiation in the visible and ultraviolet bands [*Levelt et al.*, 2006a; *Russell et al.*, 2012]. The radiance measurements are used to derive trace gases concentrations in the atmosphere, such as O_3, NO_2, HCHO, and SO_2. OMI has a nadir resolution of 13 km × 24 km and provides nearly global coverage in one day.

Two widely-used archives of OMI NO_2 VCD products are available: NASA OMNO2 (v 2.1) (https://disc.gsfc.nasa.gov/Aura/data-holdings/OMI/omno2_v003.shtml) and KNMI DOMINO (v 2.0) (http://www.temis.nl/airpollution/no2.html). Although both apply a Differential Optical Absorption Spectroscopy (DOAS) algorithm to derive NO_2 slant column densities, they have significant differences in stratospheric and tropospheric NO_2 slant column densities (SCD) separation, NO_2 vertical profiles, and air mass factor calculation (AMF) [*Boersma et al.*, 2011; *Bucsela et al.*, 2013; *Chance*, 2002; *Oetjen et al.*, 2013; *van der A et al.*, 2010]. Both OMNO2 and DOMINO had been extensively evaluated with field measurements and models [*Boersma et al.*, 2011; *Boersma et al.*, 2009; *Hains et al.*, 2010; *Huijnen et al.*, 2010; *Ionov et al.*, 2008; *Irie et al.*, 2008; *Lamsal et al.*, 2014; *Oetjen et al.*, 2013]. The estimated uncertainty of DOMINO TVCD product is 1.0×10^{15} molecules/cm^2 + 25% [*Boersma et al.*, 2011], while the uncertainty of OMNO2 TVCD product is from about 30% under clear-sky conditions to about 60% under cloudy conditions [*Lamsal et al.*, 2014; *Oetjen et al.*, 2013; *Tong et al.*, 2015]. In this study, to reduce uncertainties, we only accepted TVCD data with effective cloud fractions less than 0.2 (corresponding to cloud radiance fractions approximately < 50%). Besides, those data affected by row anomaly were excluded (http://projects.knmi.nl/omi/research/product/rowanomaly-background.php).

It is noteworthy that both DOMINO and OMNO2 calculated air mass factors (AMF) by using a prior NO_2 vertical profiles with coarse resolutions: DOMINO used TM4 model results with a resolution of 3° × 2° [*Hains et al.*, 2010], while OMNO2 used monthly mean values from the Global Modeling Initiative (GMI) model with a resolution of 2° × 2.5°. The under-sampling of a prior NO_2 profiles may cause misrepresentation on

the spatial and temporal characteristics of NO_2 at satellite pixel scales. Therefore, in this study, we also updated the OMI retrieval with daily REAM profiles (13:00 LT – 14:00 LT) by using the KNMI algorithm and evaluated the effect of a prior profiles on the retrieval. In the retrieval, we removed satellite scenes with effective cloud fractions over than 0.2 or contaminated by row anomaly.

The GOME-2 instrument embarked on the polar-orbiting MetOp-A satellite (known as GOME-2A) launched on 2006 is an improved version of GOME-1 launched in 1995 and has an overpass time of 9:30 LT and a spatial resolution of 80×40 km^2 [*Munro et al.*, 2006; *Peters et al.*, 2012]. GOME-2A measures backscattered solar radiation in the range from 240 nm to 790 nm which is used for VCD retrieval of trace gases, such as O_3, NO_2, BrO, and SO_2 [*Munro et al.*, 2006]. We used the GOME-2A NO_2 VCD product archived on http://www.temis.nl/airpollution/no2col/no2colgome2_v2.php. The algorithm from this product is the same as that for KNMI DOMINO [*Boersma et al.*, 2004; *Boersma et al.*, 2011]. GOME-2A derived NO_2 VCD have been validated with SCIAMACHY and MAX-DOAS measurements [*Irie et al.*, 2012; *Peters et al.*, 2012; *Richter et al.*, 2011]. The same as DOMINO, we ignored pixels with effective cloud fractions greater than 0.2 and redid the GOME-2A retrieval with REAM daily NO_2 profiles (9:00 LT – 10:00 LT).

2.2.3 Ground-based NO_2 VCD measurements — Pandora

Pandora is a small direct sun spectrometer system, which measures sun and sky radiance from 270 to 530 nm in 0.5 nm steps with a 1.6° field of view and allows the retrieval of the total VCD of NO_2 with a clear-sky precision of about 2.7×10^{14}

molecules/cm^2 and an nominal accuracy of 2.7×10^{15} molecules/cm^2 [*Herman et al.*, 2009; *Lamsal et al.*, 2014]. There are 12 Pandora sites available in the Discover-AQ campaign: six of them were the same as the P-3B aircraft spiral sites (Aldino, Edgewood, Beltsville, Essex, Fairhill, and Padonia), while the other six sites were Naval Academy (Annapolis Maryland) (USNA), University of Maryland College Park (UMCP), University of Maryland Baltimore County (UMBC), Smithsonian Environmental Research Center (SERC), Oldtown in Baltimore (Oldtown), and Goddard Space Flight Center (GSFC). In this study, we exclude the USNA site as its measurements are conducted on a ship ("Pandora(w)" in Figure 2.8.b) and there are no other surface observations in the "Pandora(w)" grid. Based on our calculations, the USNA site has minimal impacts on the following evaluation of NO_2 TVCD and won't change our conclusions. Also, we ignored Pandora measurements with solar zenith angles (SZA) greater than 80°. Besides, we ignored any hour with less than three valid measurements available to reduce the uncertainties of the hourly averages due to the significant variations of Pandora observations.

It should be noted that Pandora measured total NO_2 VCD, and we need to subtract stratosphere NO_2 VCD from the total VCD to get TVCD. Stratosphere NO_2 VCD shows clear diurnal cycles with an increased trend during daytime due to the photolysis of N_2O_5 [*Brohede et al.*, 2007; *Dirksen et al.*, 2011; *Kurzeja*, 1975; *Peters et al.*, 2012; *Sen et al.*, 1998]. Figure 2.9 shows the stratospheric NO_2 VCD variations from 5:00 – 20:00 LT in mid-latitude regions (46° N, 117.5° W) in the US in July 2011 from the GMI model [*Spinei et al.*, 2014], as well as coincident satellite stratospheric NO_2 VCD (Figure 2.9.a) and satellite stratospheric NO_2 VCD in the DISCOVER-AQ campaign region (about

39.5° N, 76° W) (Figure 2.9.b). The significant increase of stratospheric NO_2 VCD from GOME-2A to OMI (Figures 2.9.a and 2.9.b) is consistent with the increasing trend in the daytime from the GMI model. As GOME-2A and OMI only provide stratospheric NO_2 VCD at 9:30 LT and 13:30 LT, the DISCOVER-AQ campaign region (39.5° N) has a latitude close to the GMI region (46° N), and satellite stratospheric NO_2 VCD show differences of fewer than 0.5×10^{15} molecules/cm^2 between the DISCOVER-AQ region and the GMI region, we used the GMI stratospheric NO_2 VCD in Figure 2.9 to calculate the Pandora NO_2 TVCD in this study. The stratospheric NO_2 VCD discrepancies between the GMI estimates and satellite products won't change the pattern of Pandora NO_2 TVCD diurnal variations and won't affect our conclusions in this study.

2.2.4 Surface NO_2 and O_3 measurements

The principle to measure NO_x is based on the chemiluminescence of electronically excited NO_2^* which results from the reaction of NO with O_3, and the strength of the chemiluminescence from the decay of NO_2^* to NO_2 is proportional to the number of NO molecules present before reaction with O_3 [*C. Reed et al.*, 2016]. We can measure NO_2 concentrations by this method by converting NO_2 to NO first. Two widely used approaches to convert NO_2 to NO are catalytic reactions (typically on the surface of heated molybdenum oxide (MoO_x) substrate) and photolytic processes [*Lamsal et al.*, 2015; *C. Reed et al.*, 2016]. However, for the catalytic method, not only NO_2 but also NO_z (non-NO_x active nitrogen compounds, such as PAN, HNO_3, organic nitrate compounds, etc.) can be reduced to NO on the heated surface, which thus causes the overestimation of NO_2. The magnitude of the overestimation depends on not only the relative fraction of NO_z to the total active nitrogen compounds but also the reduction

efficiency of NO_z to NO, both of which are highly uncertain for different ambient and experiment conditions. While for the photolytic approach, it employs broadband photolysis of ambient NO_2 and eliminates the reduction of NO_z to NO, therefore offers right NO_2 measurements with better accuracy [*Lamsal et al.*, 2015].

The EPA AQS (Air Quality System) monitoring network provides hourly NO_2 and O_3 measurements over the United States. There are 11 NO_x monitoring sites in the DISCOVER-AQ campaign region, including those from AQS network and those deployed in the campaign. Nine of them measure NO_2 by using the EPA-designated NO_2 chemiluminescence automated Federal Reference Method (FRM) which applied catalysts to convert NO_2 to NO. The other two sites (Edgewood and Padonia) contains NO_2 measurements from both the catalytic approach and the photolytic method. FRM measured NO_2 should be first converted to true NO_2 because of the overestimation of NO_2 caused by the reduction of NO_z to NO.

Four types of stationary FRM instruments were available in the above 11 monitoring sites during the campaign: Thermo Electron 42C-Y NO_y analyzer, Thermo Model 42C NO_x analyzer, Thermo Model 42I-Y NO_y analyzer, and Ecotech Model 9841/9843 T-NO_y. Besides, a mobile platform — NATIVE (http://ozone.met.psu.edu/Native/), which stands for Nittany Atmospheric Trailer and Integrated Validation Experiment, was also deployed to measure NO and NO_y ($NO_y = NO_z + NO_x$) through a Thermo Electron 42C-Y NO_y analyzer (http://www.agriculturedefensecoalition.org/sites/default/files/pdfs/33A_2006_NASA_NATIVE_Battelle_NATIVE_Schedule_2006.pdf) in the Edgewood site. The photolytic

measurements of NO_2 in Edgewood and Padonia were from Teledyne API model 200eup photolytic NO_x analyzers. We used the ratios of NO_2 from the photolytic analyzer to NO_2 from the coincident FRM analyzers to convert FRM NO_2 to true NO_2 in other monitoring sites. Figure 2.2 shows the monthly averaged diurnal cycles of these ratios for different FRM instruments during the campaign. The ratios were lowest at noon and highest in the early morning (Figure 2.2), which indicates the high fraction of NO_z to the total active nitrogen compounds at noon due to strong photochemistry reactions and the low fraction in the early morning due to high NO_x emissions and weak chemistry production of NO_z.

For each NO_2 monitoring site, as long as photolytic measurements were available, we used the photolytic measurements; if there were no photolytic measurements, we scaled the FRM measurements by the ratios of the corresponding instruments in Figure 2.2. Thermo Model 42I-Y NO_y analyzer was used only in Padonia where photolytic measurements were available, so we didn't calculate the ratios for the Thermo Model 42I-Y NO_y analyzer in this study.

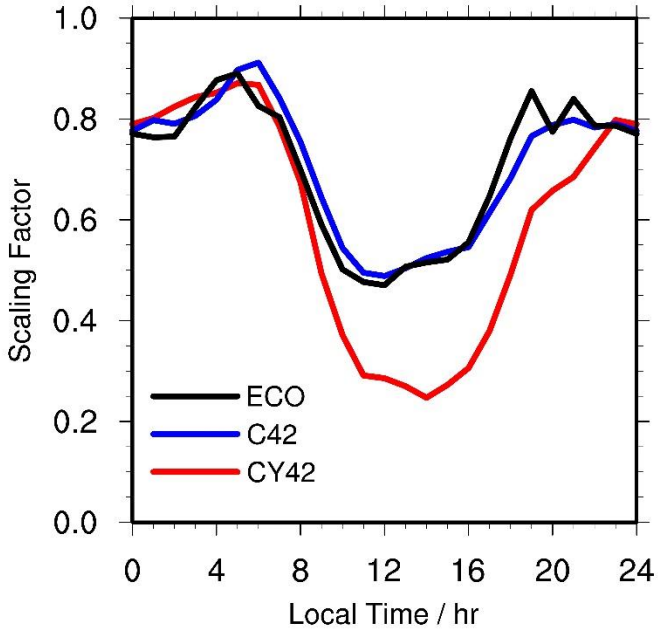

Figure 2. 2 Hourly ratios of NO_2 from different FRM instruments to NO_2 from the Teledyne API model 200 eup photolytic NO_x analyzer in 2011 July. "CY42" is calculated by NO_2 measurements from the Thermo Electron 42C-Y NOy analyzer and the Teledyne API model 200eup photolytic NO_x analyzer in Edgewood. "C42" is based on the Thermo Model 42C NO_x analyzer and the Teledyne API model 200eup photolytic NO_x analyzer in Padonia, while "ECO" is from the Ecotech Model 9841/9843 T-NO_y analyzer and the photolytic NO_x analyzer in Padonia.

Besides, 19 surface O_3 monitoring sites were available in the DISCOVER-AQ campaign region. These monitoring sites measure O_3 by a Federal Equivalent Method (FEM) with an uncertainty of 5 ppb, and the FEM is based on the UV absorption of O_3 (https://www.arb.ca.gov/aaqm/qa/qa-manual/vol4/chapter6o3.pdf). The locations of NO_2 and O_3 monitoring sites are displayed in Figure 2.8.b.

2.2.5 Aircraft measurements of NO_2

In this study, we used the NO_2 mixing ratios measured by the National Center for Atmospheric Research (NCAR) 4-channel chemiluminescence instrument (P-CL)

onboard the P-3B aircraft. The instrument has a NO_2 measurement uncertainty of 10% - 15% and a 1 second, one sigma detection limit of 30 pptv (https://discover-aq.larc.nasa.gov/pdf/2010STM/Weinheimer20101005_DISCOVERAQ_AJW.pdf).

NO_2 measurements from aircraft spirals provide us with NO_2 vertical profiles. Figure 2.8.b shows the locations of the aircraft spirals used in this study. We didn't use the Chesapeake Bay observations as it is over the ocean. Only six vertical profiles are available from the Chesapeake Bay measurements, and their contributions to the averaged vertical profiles are minimal. Finally, we got 238 vertical profiles in the daytime and no data during the nighttime in July 2011.

The aircraft measurements generally covered altitudes from about 400 m in the boundary layer to 3.63 km in the free troposphere. We binned these measurements to REAM levels. In order to make up the missing observations between the surface and 400 m, we did quadratic polynomial fitting by using aircraft data below 1 km and surface measurements from coincident ground-based instruments. As shown in Figures 2.5.a and 2.5.b in section 2.3.1.2 and section 2.3.2, the fitting values are in reasonable agreement with the corresponding aircraft observations.

2.3 Results and discussion

Industrial activities and traffic, which are the dominant anthropogenic NO_x emissions over the United States, are reduced during weekends, which leads to significantly lower (20% - 50%) NO_x emissions on weekends than on weekdays [*Beirle et al.*, 2003; *Boersma et al.*, 2009; *Y. Choi et al.*, 2012; *DenBleyker et al.*; *Kaynak et al.*, 2009]. The

temporal characteristics of traffic on weekends are also different from weekdays, especially in urban regions: weekday traffic shows clear morning and afternoon rush-hour peaks, while weekend traffic is roughly evenly distributed in the daytime [*DenBleyker et al.*]. Therefore, it is necessary to separate weekdays from weekends for our analyses and evaluations of NO_2 diurnal variations. We will first discuss weekday NO_2 diurnal cycles in section 2.3.1.

2.3.1 Weekday diurnal cycles of NO_2

2.3.1.1 Effect of vertical mixing in the boundary layer on diurnal variations of surface NO_2 and O_3

Figures 2.3.a and 2.3.b displays the observed and simulated diurnal cycles of surface NO_2 and O_3 concentrations on weekdays in July 2011 in the DISCOVER-AQ campaign region. REAM with raw k_{zz} significantly overestimates NO_2 and underestimated O_3 during the nighttime, although it captures the basic patterns of the diurnal cycles of surface NO_2 and O_3 — a peak of O_3 and a minimum of NO_2 around noontime (Figures 2.3.a and 2.3.b). NO_2 and O_3 have different vertical profiles in the lower troposphere during the nighttime: NO_2 has a negative gradient relative to altitude while it is positive for O_3, which is due to their different sources and sinks. NO_2 mainly comes from NO_x emissions which is concentrated near the surface. O_3 is produced only in the daytime through the photochemistry of VOC and NO_x. At night O_3 is removed mainly by reactions with NO ($O_3 + NO \rightarrow O_2 + NO_2$) and NO_2 ($NO_2 + O_3 \rightarrow NO_3 + O_2$) and dry deposition, both of which happened dominantly near the surface, so O_3 is consumed most near the surface, which induces the lowest O_3 concentrations near the ground. Vertical mixing can undermine these vertical gradients through mixing high-concentration gases

with low-concentration gases, which will decrease NO_2 concentrations but increase O_3 concentrations near the surface. Therefore, the overestimation of NO_2 and the underestimation of O_3 during the nighttime may be the result of too weak vertical mixing in REAM.

During the Discover-AQ campaign, vertical wind velocities in REAM was almost 0 at night and have little impact on vertical mixing. The nighttime vertical mixing is mainly attributed to turbulence which is simulated by k_{zz}. k_{zz} is a function of PBL height (PBLH, which was referred as mixing depth as described in http://wiki.seas.harvard.edu/geos-chem/index.php/Boundary_layer_mixing) in the YSU scheme [*Hong et al.*, 2006; *Hu et al.*, 2013; *Shin and Hong*, 2011]. However, it had been noticed that YSU scheme in WRF might underestimate nighttime vertical mixing or PBLH [*Breuer et al.*, 2014; *Hu et al.*, 2012], which is consistent with Figure 2.4 showing that k_{zz}-determined mixing depth from WRF are significantly lower than Lidar observations in the late afternoon and at night at the UMBC site. The Lidar mixing depths were derived from the Elastic Lidar Facility (ELF) attenuated backscatter signals by using the covariance wavelet transform method and had been validated against radiosonde measurements, Radar wind profiler observations, and Sigma Space mini-micropulse lidar data [*Compton et al.*, 2013].

Therefore, we update k_{zz} in REAM (the method is described in the supplement), which significantly improves the PBLHs in the late afternoon and at night (Figure 2.4). Then NO_2 concentrations decrease significantly, and O_3 concentrations increase significantly during the nighttime for the REAM simulation with updated k_{zz} (Figures

2.3.a and 2.3.b) — the prediction of O_3 and NO_2 is much improved in REAM. All the following discussions will be based on the REAM simulation with updated k_{zz}.

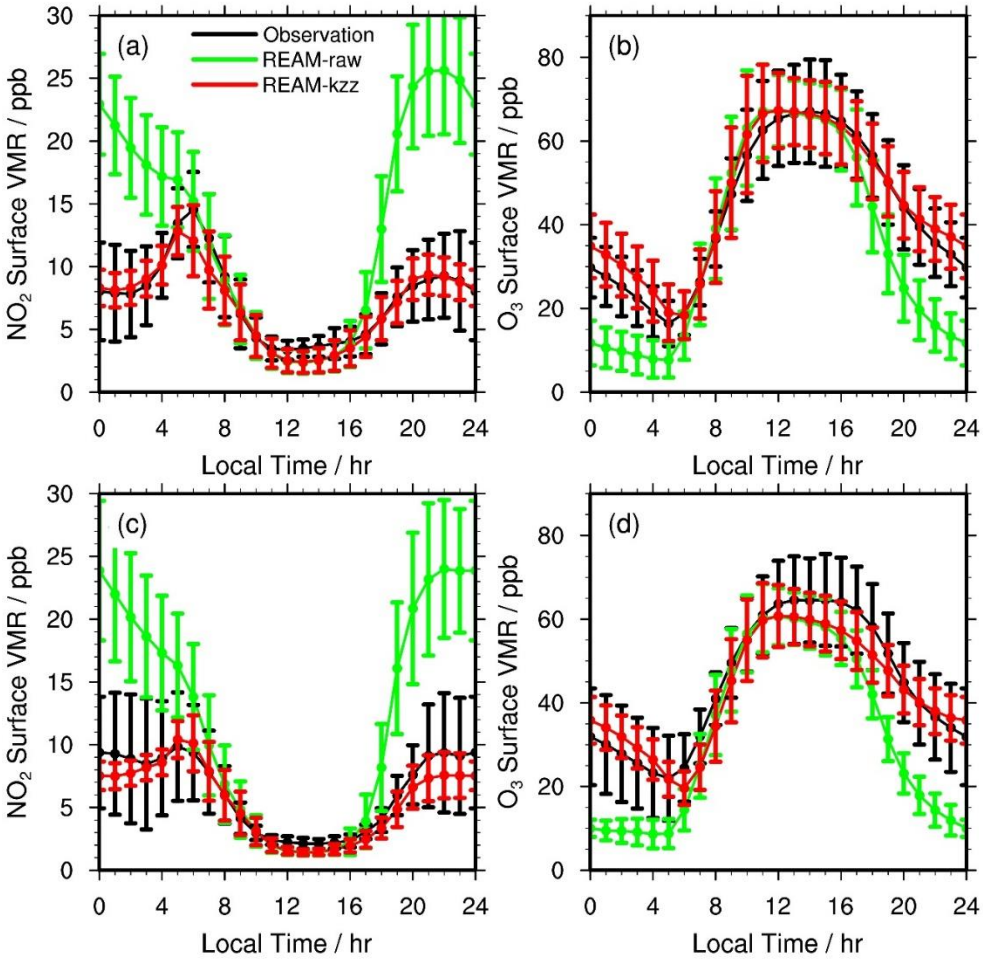

Figure 2. 3 Diurnal cycles of surface NO_2 (a, c) and O_3 (b, d) on weekdays (a, b) and weekends (c, d) during the DISCOVER-AQ campaign in the campaign region. "REAM-raw" denotes the REAM simulation with unchanged k_{zz}, and "REAM-kzz" is the REAM simulation with updated k_{zz}.

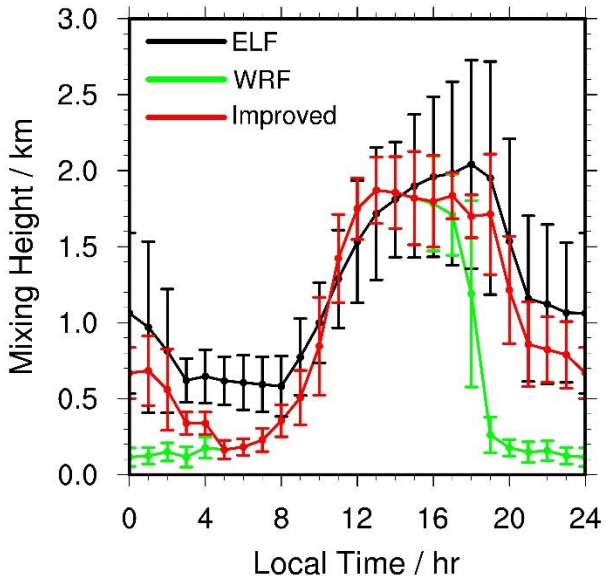

Figure 2. 4 ELF observed PBLH diurnal cycles at the UMBC site during the Discover-AQ campaign and corresponding WRF k_{zz}-determined PBLH diurnal cycles. "ELF" denotes ELF derived PBLHs by using the covariance wavelet transform method. "WRF" denotes the PBLHs calculated by k_{zz} and "Improved" denotes PBLHs derived from updated k_{zz}.

The diurnal cycles of surface NO_2 in Figure 2.3.a are consistent with our current knowledge of chemistry and physics mechanisms and are in good agreement with previous researches [*Anderson et al.*, 2014; *David and Nair*, 2011; *Gaur et al.*, 2014; *Reddy et al.*, 2012]. As shown in Figure 2.3.a, surface NO_2 peaks in the morning (about 6:00 – 7:00 LT) and again at early night (20:00 – 23:00 LT). Each peak is caused mainly by a low NO_2 loss rate and relatively weak vertical mixing. The high emissions from the early morning and evening rush-hours are also contributors to the two peaks. Daytime surface NO_2 concentrations are relatively lower compared to nighttime, and NO_2 concentrations reach a minimum around noontime. This is because, on the one hand, the sink of NO_2 through the reaction of NO_2 and OH becomes stronger as solar radiation increases in the daytime, which becomes strongest around noontime; on the other hand,

vertical mixing strengthens as solar radiation become stronger causing a thicker PBLH, and vertical mixing transfers near-surface NO_2 into higher altitudes. During the nighttime, surface NO_2 concentrations have less significant variations compared to daytime, and the nighttime peak is weak. This nighttime pattern was mainly controlled by the following 3 factors: (1) NO_x emissions are decreasing during the nighttime until they reach a minimum at around 4:00 LT in the next day (Figure 2.1); (2) PBLH is reduced (Figure 2.4), and vertical mixing becomes weaker, which causes the accumulation of NO_2 near the surface; (3) N_2O_5 hydrolysis is the main sink path of NO_x at night. Before the nighttime peak, weak N_2O_5 hydrolysis and vertical mixing cause the rising of surface NO_2, and the decrease of NO_x emissions cannot offset this effect until at the nighttime peak when the above 3 factors were completely balanced. After the nighttime peak, as N_2O_5 hydrolysis increases to its maximum and keeps almost constant, gradually decreasing NO_x emissions and slowly weakened vertical mixing resulted in the slight variation of surface NO_2 concentrations and steady-decreasing O_3 concentrations (Figures 2.3.a and 2.3.b).

2.3.1.2 Diurnal variations of NO_2 vertical profiles

Figures 2.5.a and 2.5.c display the temporal variations of observed and simulated NO_2 vertical profiles in the daytime of weekdays during the DISCOVER-AQ campaign. REAM well reproduces the observed characteristics of NO_2 vertical profiles in the daytime which are dominated by vertical mixing and OH concentrations. In the early morning (6:00 a.m. - 8:00 a.m.), k_{zz} is little and vertical mixing is weak, so NO_2, which is mainly from surface NO_x sources, is concentrated in the surface layer. Also, OH concentrations induced by solar radiation are deficient, and NO_2 sink path through the

reaction of NO_2 and OH is suppressed. As a result, NO_2 mixing ratios in the lower layers are significantly higher than those from 9:00 a.m. – 5:00 p.m. After 8:00 a.m., as vertical mixing becomes stronger, NO_2 mixing ratios below about 500 m are significantly reduced, while those above the height are conversely increased. This decreased gradient is primarily attributed to stronger vertical mixing, although enhanced OH concentrations is also a factor. The effect of OH concentrations is reflected by a comparison between 12:00 p.m. – 2:00 p.m. and 3:00 p.m. – 5:00 p.m.: NO_2 vertical profiles during these two periods are similar in shape but the profile of 3:00 p.m. – 5:00 p.m. has higher NO_2 mixing ratios than that of 12:00 p.m. – 2:00 p.m. This is because OH concentrations from 3:00 p.m. – 5:00 p.m. are lower than those from 12:00 p.m. – 2:00 p.m., which inhibits the sink of NO_2. From 3:00 p.m. to 5:00 p.m., we find a tiny tail in the REAM profile but not in the aircraft fitting profile (Figures 2.5.a and 2.5.c). One possible reason is the biases of the surface NO_2 observations due to the uncertainties of scaling FRM measurements in section 2.2.4, as aircraft measured NO_2 mixing ratios from 400 m to 1 km show a tail trend but the surface NO_2 observation, which is even lower than the 400 m aircraft measurement, breaks the trend. Another possible reason is the relatively weak vertical mixing in the late afternoon in REAM, which may be still not strong enough to fully mix low-layer air with high-layer air even though we have updated k_{zz} in REAM (Figure 2.4).

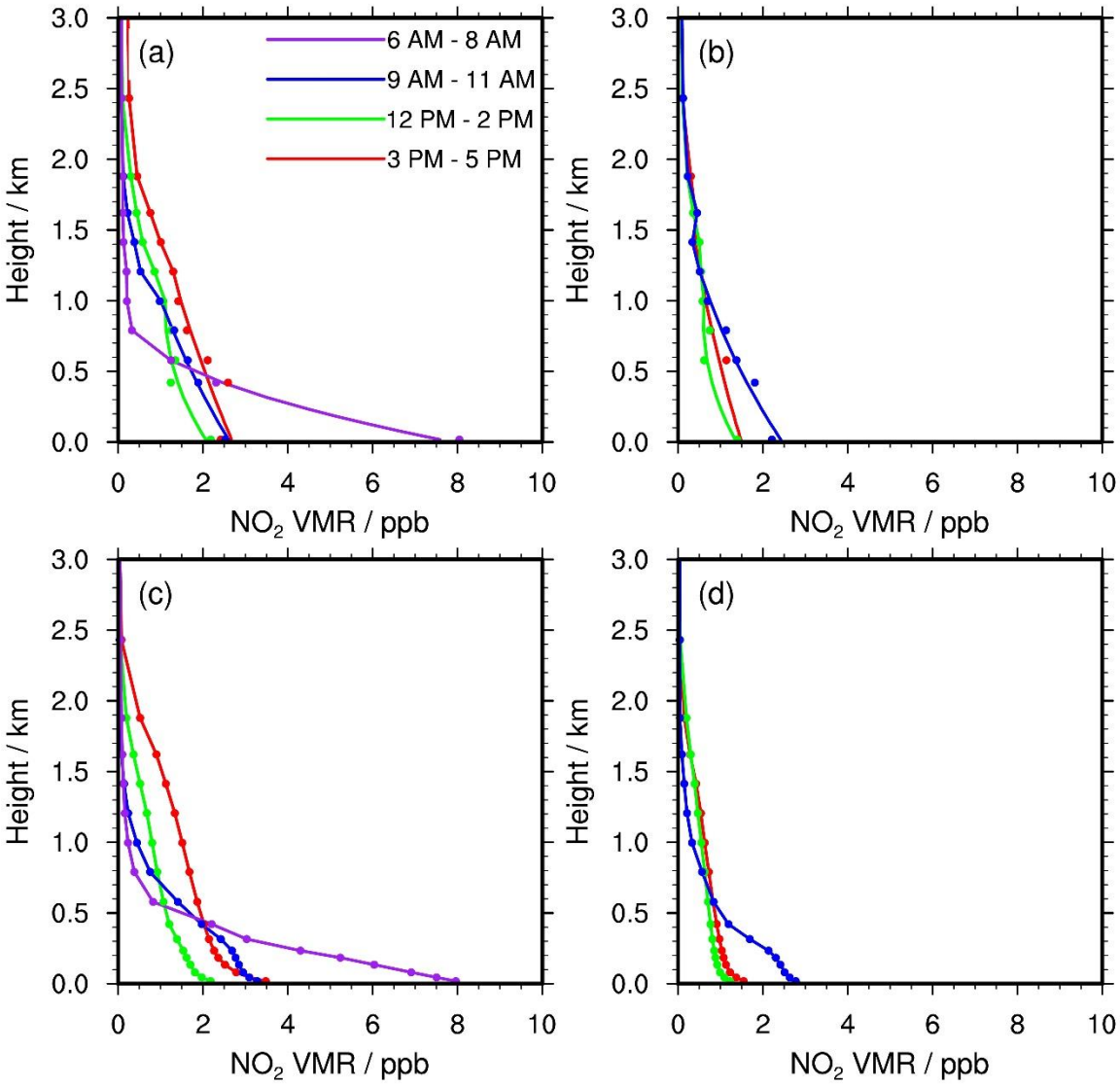

Figure 2. 5 Diurnal variations of NO_2 vertical profiles on weekdays (a, c) and weekends (b, d) from the aircraft (a, b) and REAM (c, d) during the DISCOVER-AQ campaign.

2.3.1.3 Diurnal cycles of NO_2 TVCD

We find that four Pandora sites during the campaign had their instruments located significantly above the ground surface: UMCP, about 20 m; UMBC, about 30 m; SERC, about 40 m; GSFC, about 30 m. While for all other Pandora sites, the instruments were only about 1.5 m high. In the morning, a large quantity of NO_2 stays in the near-surface

layers (Figures 2.5.a and 2.5.c). As shown in Figure 2.10.a, according to the REAM results, about 5% - 20% NO_2 are missing in the Pandora TVCD observations at 6:00 a.m. at the four mentioned sites. Consequently, we can't ignore the missing NO_2 below the instruments for the four Pandora sites. We add the missing NO_2 to the original Pandora TVCD and find that the TVCD averages from all the 11 Pandora sites increase about 0.3 $\times 10^{15}$ molecules / cm^2 in the early morning and are almost the same as before in the midday and the afternoon (Figure 2.10.b). After the averaging, the missing part of NO_2 below instruments is not a big issue for our following analyses but may be an important factor for single-site Pandora comparisons in future researches.

The diurnal variations of NO_2 TVCD from satellites, updated Pandora, REAM, and the aircraft on weekdays are shown in Figure 2.6.a. We calculate aircraft derived TVCD by using equation (2.1):

$$TVCD_{aircraft}(t) = \frac{\sum c_{aircraft}(t) \times \rho_{REAM}(t) \times V_{REAM}(t)}{A_{REAM}} \quad (2.1),$$

where t stands for time; $c_{aircraft}$ (v/v) stands for the NO_2 mixing ratio at each level from the fitted aircraft vertical profile at time t; ρ_{REAM} ($molecules / cm^3$) is the density of air from REAM at the corresponding level; V_{REAM} (cm^3) stands for the relevant air volume of REAM; A_{REAM} (cm^2) is the surface area of REAM grids. In the calculation, we only use NO_2 below 3.63 km because few aircraft measurements are available above this height in the campaign. According to the REAM results, 84% of tropospheric NO_2 are located below 3.63 km which is consistent with the GMI model with 85% - 90% tropospheric NO_2 concentrated below 5 km [*Lamsal et al.*, 2014]. Therefore, our calculated aircraft NO_2 VCD roughly represent NO_2 TVCD.

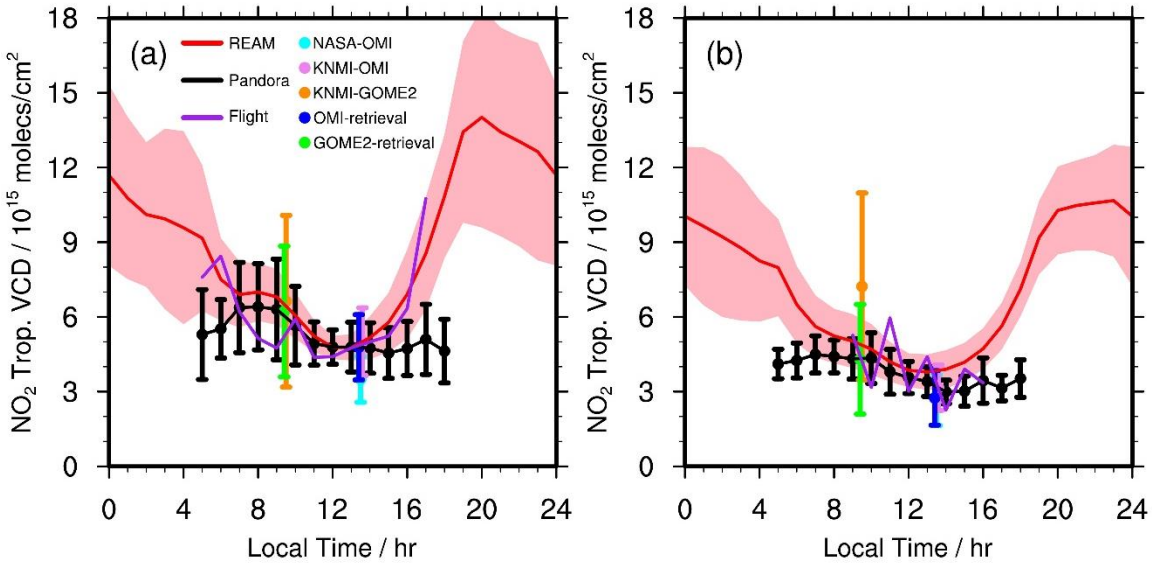

Figure 2. 6 Diurnal variations of NO_2 TVCD on weekdays (a) and weekends (b) during the DISCOVER-AQ campaign. "Pandora" refers to updated Pandora TVCD which included the NO_2 VCD below the Pandora instruments; "Flight" denotes calculated NO_2 VCD from the fitted aircraft vertical profiles. "NASA-OMI" is the OMI NO_2 TVCD retrieved by NASA; "KNMI-OMI" is the OMI NO_2 TVCD from KNMI; "KNMI-GOME2" is the GOME-2A NO_2 TVCD from KNMI. "OMI-retrieval" and "GOME2-retrieval" denote OMI and GOME-2A TVCD retrieved by using the KNMI algorithm but with REAM daily vertical profiles.

As shown in Figure 2.6.a, although Pandora, aircraft, and satellite products only provide daytime TVCD measurements, they are generally in reasonable agreement with REAM. Both GOME-2A and OMI products are very close to REAM, Pandora, and aircraft TVCD except that NASA-derived OMI TVCD are some lower than other datasets (still within uncertainties) which may be partly due to biased a prior vertical profiles from the GMI model in the NASA retrieval in the campaign [*Lamsal et al.*, 2014]. TVCD derived by using REAM NO_2 vertical profiles are quite comparable to those from KNMI,

which indicated that the TM4 model from KNMI provided reasonable estimates of a prior NO_2 vertical profiles on weekdays in the campaign region in summer.

We find evident decreases from GOME-2A to OMI in Figure 2.6.a, which is consistent with Pandora and REAM, while aircraft observations roughly capture this feature but show large variations because of the limitations of aircraft measurements and the uncertainties of the procedures we apply on the data. The trending feature is also consistent with the decreasing NO_2 VCD from SCIAMACHY to OMI in summer [*Boersma et al.*, 2008; *Boersma et al.*, 2009] as SCIAMACHY and GOME-2A have close overpass time (SCIAMACHY, 10:00 LT; GOME-2A, 9:30 LT). Enhanced OH concentrations from photochemistry dominantly induce the decreasing NO_2 TVCD from GOME-2A to OMI by increasing the sink of NO_2 through the reaction between OH and NO_2.

Between 7:00 LT and 9:00 LT, Figure 2.6.a shows almost constant TVCD for REAM and Pandora, which is due to the balance between increasing NO_x emissions and enhanced OH-related sink — horizontal advection and deposition also contribute to the balance but not as important as the previous two factors. We find in Figure 2.6.a that Pandora TVCD have entirely different characteristics from REAM and aircraft derived TVCD during 5:00 LT – 7:00 LT and 14:00 LT – 18:00 LT. During 5:00 LT – 7:00 LT, Pandora has an increasing trend, while REAM and aircraft derived TVCD decrease significantly from 5:00 LT to 7:00 LT. From 14:00 LT to 18:00 LT, Pandora TVCD have little variations, but REAM and aircraft derived TVCD rise remarkably. Based on our current knowledge, as shown in Figure 2.11, as OH concentrations decrease significantly

and NO_x emissions change little in the late afternoon, NO_2 TVCD should increase sufficiently [*Boersma et al.*, 2008; *Boersma et al.*, 2009]. On the other hand, from 5:00 LT to 7:00 LT, although NO_x emissions increase, the chemistry sinks of NO_x increase more (Figure 2.11) and NO2 TVCD should reduce. So we suggest that Pandora may not well capture the characteristics of NO_2 TVCD during these two periods due to the following three factors. (1) Pandora is a pretty small instrument and is sensitive to local conditions, which may misrepresent the properties of the 36 km grids in REAM — this is similar to the effect of buildings on local surface solar fluxes [*B. Zhao et al.*, 2016]. (2) SZAs in the early morning and the late afternoon are relatively larger which may enhance the uncertainties of Pandora [*Herman et al.*, 2009], even though we have excluded Pandora measurements with SZA > 80°. (3) Pandora has few observations in the early morning, which may misrepresent the TVCD trend during that period.

REAM nighttime TVCD are relatively larger than its daytime TVCD, which is mainly attributed to less NO_x sink. Although nighttime NO_x emissions are significantly lower than daytime, the nighttime sink through chemistry is much smaller than the daytime (Figure 2.11). It seems to be inconsistent with *Tsai et al.* [2014] and *Brown et al.* [2004] which suggest that the contribution of nocturnal chemistry to NO_x removal in a 24 period can reach up to about 60%. However, in their studies, only NO_x sinks near the surface were considered, and the sinks in the higher portion of the PBL is missing in their calculations, which is vital in the daytime because of well-mixed PBL. Based on the REAM simulation, N_2O_5 hydrolysis and the reaction of NO_2 and OH are the dominant sink paths for NO_x at night and in the daytime, respectively. N_2O_5 hydrolysis accounts for

about half of the total nighttime sink of NO_x, while the reaction of NO_2 and OH contributes to approximately 50% of the whole daytime NO_x sink.

TVCD diurnal variations also reflect the function of vertical mixing. Figure 2.7 shows the daytime NO_2 VCD variations at different heights, and aircraft-derived datasets and coincident REAM datasets are quite comparable. As shown in Figure 2.7, the entire TVCD display a "U" pattern from 5:00 LT to 17:00 LT. However, the TVCD above 400 m have a significant increasing trend during the period. The TVCD below 400 m show a decreasing trend from 5:00 LT to 13:00 LT, almost no variations from 13:00 LT to 16:00 LT, and a sharp increase from 16:00 LT to 17:00 LT. As analyzed above, as vertical mixing become stronger after sunrise, high-NO_2 air in the lower layers is mixed with low-NO_2 air in the upper layers, which enhances the NO_2 content in the upper layers but reduces it in the lower layers. This effect is so strong above 400 m that even though NO_2 chemistry sinks increase from sunrise to noontime, the NO_2 TVCD above 400 m are still increasing. Conversely, the TVCD below 400 m decrease remarkably during this period due to both the vertical mixing effect and the increasing NO_2 chemistry sinks. From 13:00 LT to 17:00 LT, vertical mixing doesn't change much as k_{zz} already reaches to high ranges, and reduced chemistry sinks dominate the increasing trend of the TVCD above 400 m, which is most significant from 16:00 LT to 17:00 LT. The VCD below 400 m are almost the same from 13:00 LT to 16:00 LT, indicating the balance between vertical mixing, horizontal advection, chemistry sinks, dry depositions, and NO_x emissions. The sharp jump of the TVCD below 400 m from 16:00 LT – 17:00 LT is also due to the dramatically reduced OH concentrations and chemistry sinks.

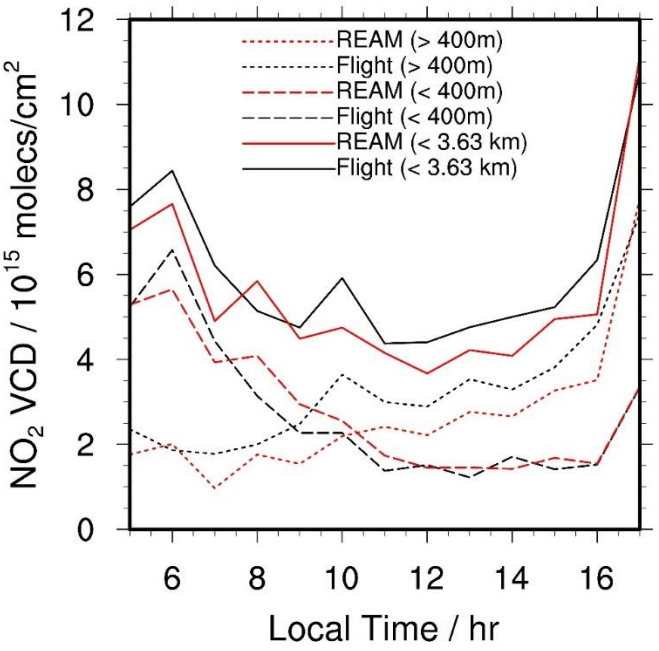

Figure 2. 7 Hourly variations of NO_2 TVCD at different heights. "Flight" denotes aircraft measurements derived NO_2 TVCD, and "REAM" denotes coincident REAM simulated TVCD.

2.3.1.4 Applications to NO_x emissions

As the REAM simulation is in reasonable agreement with the observed diurnal cycles of surface NO_2 and O_3, NO_2 vertical profile, NO_2 TVCD, we suggest that NEI2011 provides a reasonable estimate of NO_x emissions. It is consistent with *Salmon et al.* [2018] which found NEI 2011 and NEI 2014 were in agreement with aircraft observation-derived NO_x emissions, which is again confirmed through the investigation of observed and NEI NO_x/CO_2, CO/NO_x, and CO/CO_2 ratios, during the Wintertime INvestigation of Transport, Emissions, and Reactivity (WINTER) campaign in February – March 2015 around the Washington, D.C.-Baltimore area. However, our evaluation of NEI NO_x emissions is different from *Travis et al.* [2016] and *Anderson et al.* [2014].

Travis et al. [2016] compared the GEOS-Chem simulation results with observations of NO_x and its oxidation products from the SEAC^{4}RS campaign, nitrate wet deposition fluxes from the National Acid Deposition Program (NADP) network, and NO_2 TVCD from OMI, and found that NEI2011 overestimates mobile and industrial NO_x emissions by 30% - 60%. The GEOS-Chem used by *Travis et al.* [2016] had almost the same chemistry mechanism as REAM and had a horizontal resolution of 0.25° × 0.3125° which is also close to REAM (36 km × 36 km). We attribute the discrepancies between *Travis et al.* [2016] and our study to the region discrepancies of NO_x emissions and uncertainties of measurements. *Anderson et al.* [2014] evaluated NEI2011 emissions with the observed concentration ratios of CO to NO_y and CO to NO_x from the same DISCOVER-AQ campaign and found that NEI overestimates NO_x emissions by 51% - 70% in Maryland in the summer of 2011. Besides the uncertainties of transferring concentrations ratios of CO/NO_y or CO/NO_x to emission ratios of CO/NO_x due to different lifetimes of CO, and NO_x and NO_y, and the neglect of transport effect, the observed concentration ratios reflect local conditions more. With a horizontal resolution of 36 km, REAM can't assess high-resolution local emissions accurately. Therefore, we conduct a REAM simulation experiment with a horizontal resolution of 4 km in Section 2.3.3, which will show consistent results with *Anderson et al.* [2014].

2.3.2 Weekend diurnal cycles of NO_2

Because of the absence of weekend emissions in our NEI2011, we build up weekend emission inventories based on previous researches [*Beirle et al.*, 2003; *Boersma et al.*, 2009; *Y. Choi et al.*, 2012; *DenBleyker et al.*; *Kaynak et al.*, 2009] which find that weekend NO_x emissions are 20% - 50% lower than weekday emissions and weekend

NO_x emission diurnal cycle is different from weekday's. In this study, we set weekend NO_x emissions 1/3 lower than weekday emissions and less day-night variations on weekends than on weekdays (Figure 2.1).

Figures 2.3.c, 2.3.d, 2.5.b, 2.5.d, and 2.6.b show the weekend diurnal cycles of NO_2. The improvement of k_{zz} also takes effect on weekend diurnal cycles (Figures 2.3.c and 2.3.d). Generally, the REAM simulation is comparable to observations on weekends. The diurnal cycles of surface NO_2 and O_3 concentrations on weekends (Figures 2.3.c and 2.3.d) have the same patterns as those on weekdays (Figures 2.3.a and 2.3.b). However, weekend surface NO_2 concentrations are significantly lower than weekday concentrations in the daytime and comparable to weekday concentrations during the nighttime, which reflects the significant different daytime NO_x emissions but similar nighttime NO_x emissions between weekdays and weekends (Figure 2.1). Although the number of weekend aircraft observations are limited, the impact of vertical mixing on NO_2 vertical profiles is clearly shown on the transition from 9:00 a.m. – 11:00 a.m. to 12:00 p.m. – 2:00 p.m. in Figures 2.5.b and 2.5.d. The enhanced NO_2 mixing ratios during 3:00 p.m. – 5:00 p.m. due to decreasing photochemistry sinks is also shown on weekends but not as much as on weekdays because of low NO_x emissions on weekends. For weekend TVCD, they show a similar diurnal pattern as weekdays but with significantly lower magnitudes (Figure 2.6.b). REAM TVCD on weekends are quite comparable to satellite products, Pandora, and aircraft observations in most time except that, as on weekdays, Pandora TVCD have much less variation in the early morning and late afternoon than REAM and aircraft datasets which can be explained by the same reasons as on weekdays. Besides, KNMI derived GOME-2A TVCD at 9:30 a.m. are much larger than other datasets which

might be due to biased NO_2 a prior profiles from the TM4 model on weekends, as the GOME-2A retrieval by using REAM profiles shows comparable NO_2 TVCD to Pandora, REAM and aircraft datasets.

2.3.3 The effect of model resolutions on NO_2 diurnal cycles

NEI2011 has an initial resolution of 4 km, which gives us a chance to evaluate the impact of model resolutions on NO_2 diurnal cycles. By using the 4-km emission inventories, we set up a 4-km REAM with boundary and initial concentrations from the above 36-km REAM simulation. Figure 2.12 shows the NO_x emission diurnal cycles in the 4-km DISCOVER-AQ campaign region (it is different from the above 36-km region as now the 11 Pandora sites are in 11 grids of the 4-km REAM and they compose the 4-km DISCOVER-AQ campaign region). Figures 2.13 – 2.15 compare the observed and simulated diurnal cycles of surface NO_2 concentrations, NO_2 vertical profiles, and NO_2 TVCD for the 4-km REAM. The NO_2 surface concentrations and TVCD are significantly higher than observations, although they are still comparable within uncertainties and they have similar diurnal shapes (Figures 2.13 and 2.15). And the 4-km REAM NO_2 surface concentrations and TVCD are also higher than the 36-km REAM results around noontime. We find the NO_x emission rate in the 4-km DISCOVER-AQ region is about 34% higher than that in the 36-km DISCOVER-AQ region, which may be the main reason for the high NO_2 surface concentrations and TVCD in the 4-km REAM. If we re-grid the 4-km REAM results into the grids of the 36-km REAM, the re-gridded surface NO_2 and TVCD will be close to the 36-km REAM results (Figure 2.16). Therefore, the NEI2011 may not well reveal the spatial distributions of NO_x emissions at 4 km scale, but it provided good estimates at 36 km scale. The distribution issue for high-resolution NO_x

emission inventories is corroborated by comparison of the NO_x emission inventory derived from the CONsolidated Community Emissions Processor Tool, Motor Vehicle (CONCEPT MV) v2.1 and that estimated by the Sparse Matrix Operator Kernel Emissions (SMOKE) v3.0 model with the Motor Vehicle Emissions Simulator (MOVES) v2010a [*DenBleyker et al.*]. CONCEPT with finer vehicle activity information as input produced a wider-spread but less-concentrated running exhaust NO_x emissions compared to MOVES in the Denver urban area in July 2008 [*DenBleyker et al.*]. This may be why *Anderson et al.* [2014] show different results from our 36-km simulations, as described in section 2.3.1.4. In their study, they use in-situ observations and a nested CMAQ with the highest resolution of 1.33 km which pretty much represents potentially high-biased local conditions. It is very hard to build up a reliable emission inventories for the whole United States with such a high resolution with current available datasets as the significant inhomogeneity of NO_x emissions [*Marr et al.*, 2013], but we can still expect significant improvements of the temporal-spatial distributions of NO_x emissions in the near future as GPS-based information start to be used in the NEI estimates [*DenBleyker et al.*, 2017].

Besides, although the 4-km REAM captures the evolution characteristics of NO_2 vertical profiles in the daytime (Figure 2.14), its vertical mixing is too strong in the late afternoon, and the atmosphere is almost completely mixed in the boundary layer from 15:00 LT to 18:00 LT. We don't find significant difference between the nested 4-km WRF simulation and the 36-km WRF simulation but we notice that vertical velocities (w) in the late afternoon are much larger in the 4-km simulation than the 36-km simulation, which may be the reason able to explain the fully mixed boundary layer based on our sensitivity test. As the phenomenon is most significant in the late afternoon, it may be

related to deep/shallow convection. We suggest that deactivating convection at the 4-km scale may be not a good choice and appropriate convection parameterization may be still necessary for 4-km simulations to stablenize the atmosphere [*Zheng et al.*, 2016].

2.4 Conclusion

This study evaluated the simulated diurnal cycles of surface NO_2, NO_2 vertical profiles, and NO_2 TVCD from REAM with observations from air quality monitoring sites, aircraft, Pandora, OMI, and GOME-2A during the Discover-AQ 2011 campaign. In the REAM simulation, we find the boundary layer heights from the WRF simulation are significantly lower than ELF Lidar measurements after sunset. We increase k_{zz} in the late afternoon and during the nighttime, which significantly improves the comparison of PBLH between REAM with observations and eliminates the discrepancies of surface NO_2 and O_3 concentrations between REAM and observations.

Our 36-km REAM simulation well reproduces the observed diurnal cycles of surface NO_2, NO_2 vertical profiles, and NO_2 TVCD on both weekdays and weekends. However, 1), we find Pandora TVCD show much less variation than aircraft-derived and REAM-simulated TVCD, which may be due to the uncertainties of Pandora measurements with large SZAs and the strong sensitivity of Pandora to local conditions. 2), the weekday OMI NO_2 TVCD derived by NASA are somewhat lower than the KNMI OMI product, aircraft-derived TVCD, Pandora, and REAM results, which may be caused by unaccurate a prior vertical profiles used in the NASA retrieval. 3), the weekend OMI NO_2 TVCD derived by KNMI are larger than those from Pandora, aircraft, REAM, and the OMI retireval with REAM NO_2 vertical profiles, which indicates the TM4 model for the

KNMI retrieval may provide biased estimates of the a prior NO_2 vertical profiles in the weekend morning. Besides, we find that observed NO_2 concentrations in the boudary layer and NO_2 TVCD on weekends are significantly lower than on weekdays. To reproduce the weekend observations, REAM should have NO_x emissions one-third lower on weekends than on weekdays and less daytime variation on weekends than on weekdays.

We finally investigate the impact of model resolutions on NO_2 diurnal cycles by comparing a REAM simulation with a resolution of 36 km and another REAM simulation with a resolution of 4 km. There are no significant differences for the characteristics of NO_2 diurnal cycles, but we find the 4-km simulation results are significantly higher than observations and the 36-km model results. And if we re-grid the 4-km simulation results into the 36-km model grids, the re-gridded 4-km results are comparable to the 36-km REAM results. Therefore, the NEI2011 may not well capture the distributions of NO_x emissions at 4 km scale but provide good estimates of NO_x emissions at 36 km scale. In addition, we find that the effect of vertical wind velocities is not ignorable in the 4-km simulation, which are large enough to completely mix the boundary layer in the late afternoon which is inconsistent with aircraft observations. The 4-km simulation need more improvement and is the aim of future researches.

In summary, the evaluation generally comfirms our current understanding of NO_x chemistry and physcis in mesoscale chemistry and transport model and provide useful results for advanced model development.

2.5 Supporting materials

2.5.1 Method to update eddy diffusivity coefficients (k_{zz}, m/s^2)

Generally, k_{zz} decreases since late afternoon when solar radiation is reduced significantly. The decreasing rate is most significant from sunset to around 21:00 LT, and then k_{zz} decreases relatively slowly. In the boundary layer in our WRF simulation, k_{zz} decrease faster at high altitudes than near the surface but k_{zz} can't be reduced to lower values than its threshold in each model layer (we determine the planetary boundary layer height based on these thresholds in this study). And k_{zz} in urban regions decreases more slowly than in rural regions. Besides, k_{zz} has a "C" shape of vertical profile in the boundary layer with low k_{zz} values near the surface and at the upper levels of the boundary layer. In order to keep the above characteristics of k_{zz} and slow down the decreasing rate of k_{zz} since late afternoon, we update k_{zz} in the boundary layer by using the following equations.

$when\ k_{zz}(t,l) \geq 0.01\, m/s^2$,

$$k_{zz}(t+\Delta t,l) = \max\left(k_{zz}(t,l) \bullet \alpha(l)^{EF \bullet \beta(t+\Delta t)}, WRF.k_{zz}(t+\Delta t,l)\right) \quad (2.2)$$

$when\ k_{zz}(t,l) < 0.01\, m/s^2$,

$$k_{zz}(t+\Delta t,l) = \max\left(k_{zz}(t,l), WRF.k_{zz}(t+\Delta t,l)\right) \quad (2.3)$$

Where l denotes model vertical levels less than 15 (≈ boundary layer top at 15:00 LT); t is the current time, while Δt is an updating time step (= 0.5 *hours*); α is a coefficient dependent on model levels; β is a coefficient dependent on time; EF is a coefficient related to land types, and EF is 1 for urban regions and 2 for other land types; $WRF.k_{zz}$ is

the original k_{zz} from the WRF simulation. Equations (2.2) and (2.3) calculate k_{zz} at next time step with current k_{zz}. The equations are only active when t > 15:00 LT and t < 5:00 LT which is intended to update k_{zz} in the late afternoon and at night. The updated k_{zz} values are decreasing more slowly than the original WRF values since later afternoon and satisfy the characteristics described above.

2.5.1 Supporting figures

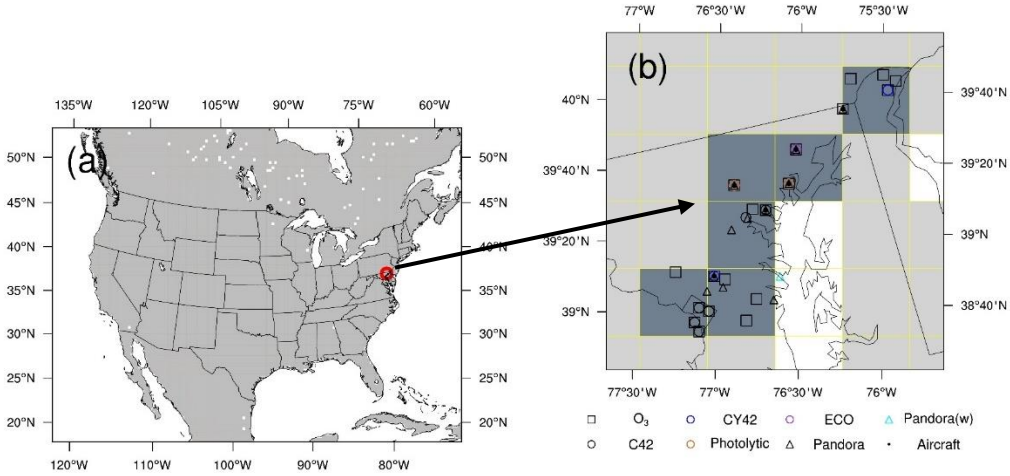

Figure 2. 8 (a), the location of the DISCOVER-AQ campaign; (b), locations of surface and aircraft observations during the campaign. Gray in (a) and slate gray and light gray (b) are the land surface, and white denotes water. We mark the DISCOVER-AQ campaign region as the six slate gray grids in (b). We exclude "Pandora(w)" in this study as it is a shipping site over the water.

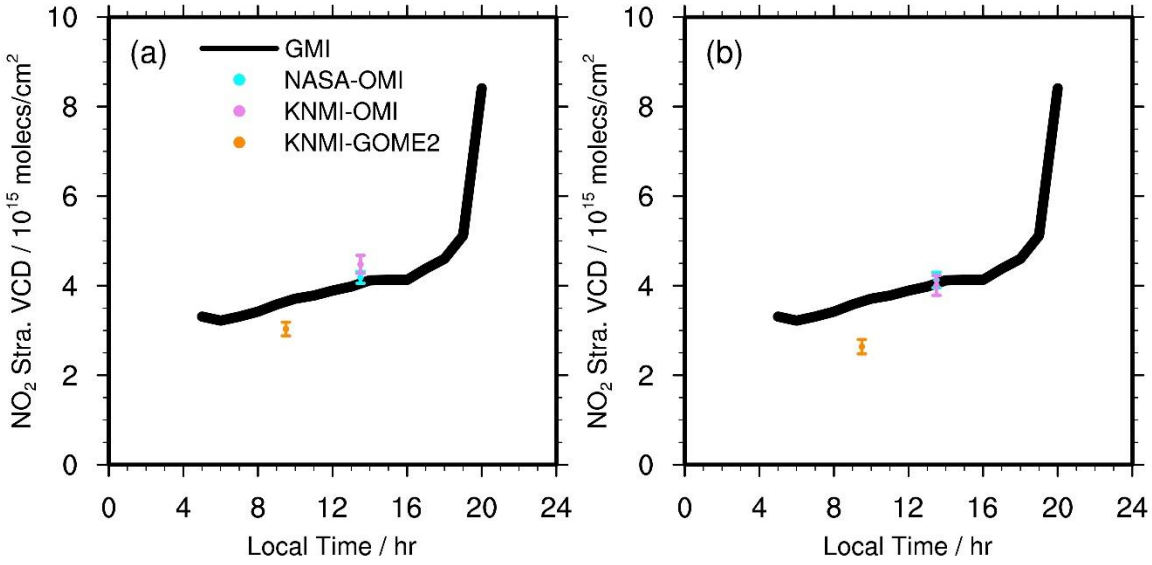

Figure 2. 9 Diurnal profiles of stratospheric NO_2 VCD at 46° / 117.5°W from the GMI model in July 2011, and (a) coincident satellite stratospheric NO_2 VCD and (b) satellite stratospheric NO_2 VCD in the DISCOVER-AQ campaign region in July 2011. "NASA-OMI" denotes the OMI NO_2 VCD from NASA, "KNMI-OMI" denotes the OMI NO_2 VCD from KNMI, and "KNMI-GOME2" denotes the GOME-2A NO_2 VCD from KNMI.

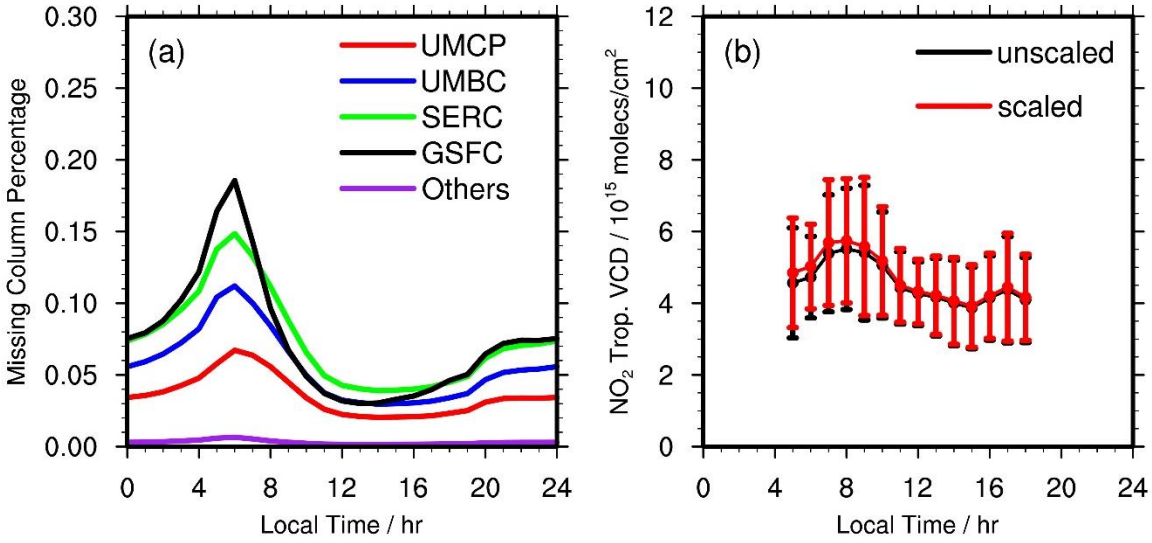

Figure 2. 10 (a), the percentages of NO_2 TVCD below Pandora instruments in REAM in July 2011; (b), the comparison between original Pandora TVCD and updated Pandora TVCD which add the VCD below the Pandora instruments to the original Pandora

TVCD. This figure uses monthly average in July and doesn't separate weekdays and weekends.

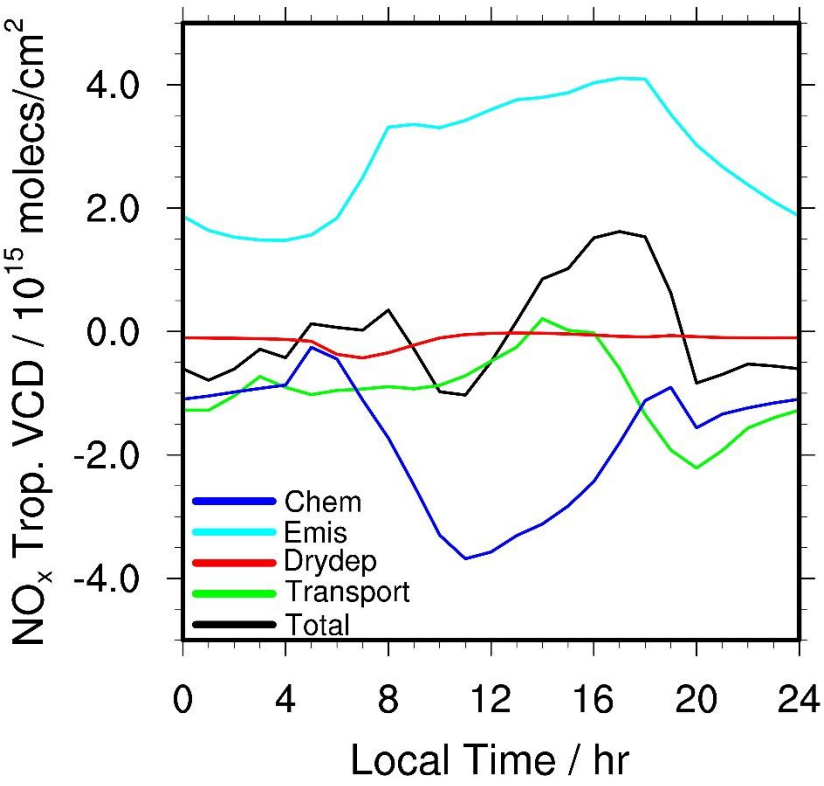

Figure 2. 11 Weekday diurnal cycles of NO_x chemistry, emissions, dry depositions, transport, and ∆(TVCD) in the DISCOVER-AQ campaign region in July 2011. "Chem" refers to NO_x chemistry productions; "Emis" refers to NO_x emissions; "Drydep" denotes NO_x dry depositions; "Transport" includes NO_x horizontal advection, lightning NO_x production, and wet deposition (convection and turbulence diffusion don't affect NO_x TVCD). "Total" is the hourly change of NO_x TVCD - ∆(TVCD).

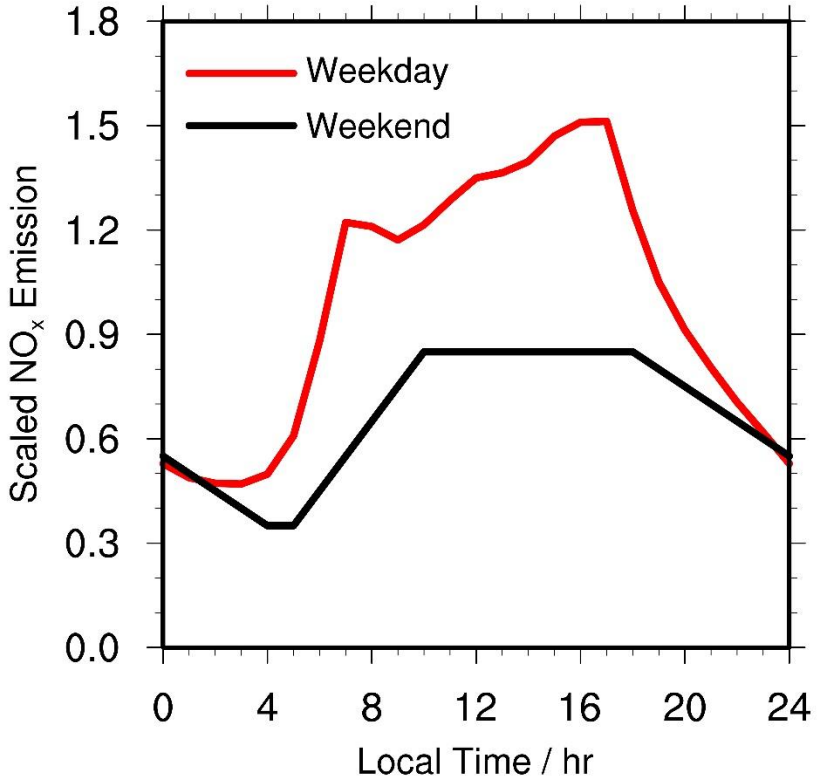

Figure 2. 12 Relative diurnal profiles of NO_x emissions on weekdays and weekends at 4 km scale.

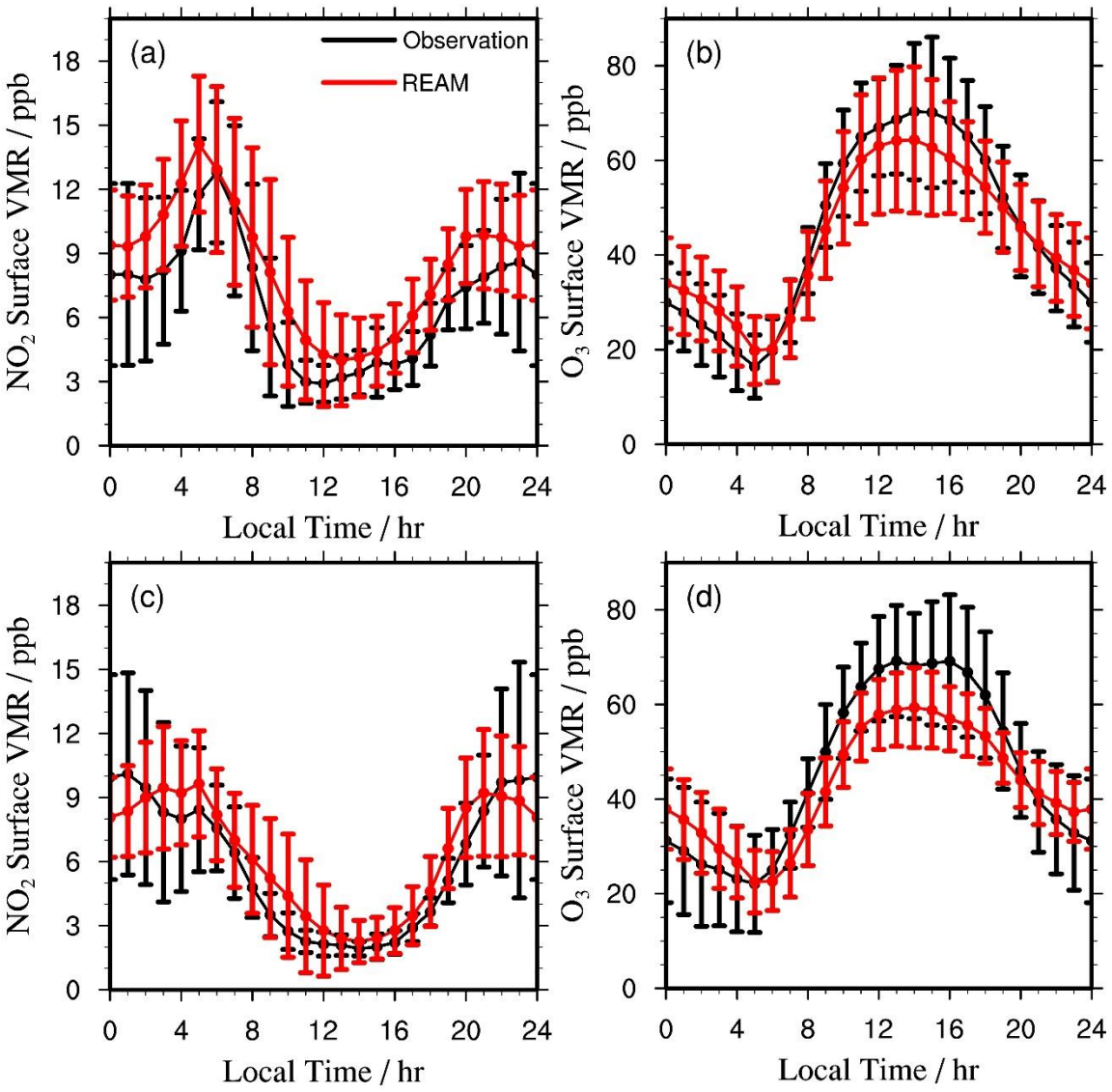

Figure 2. 13 Diurnal cycles of surface NO_2 (a, c) and O_3 (b, d) concentrations on weekdays (a, b) and weekends (c, d) at 4 km scale.

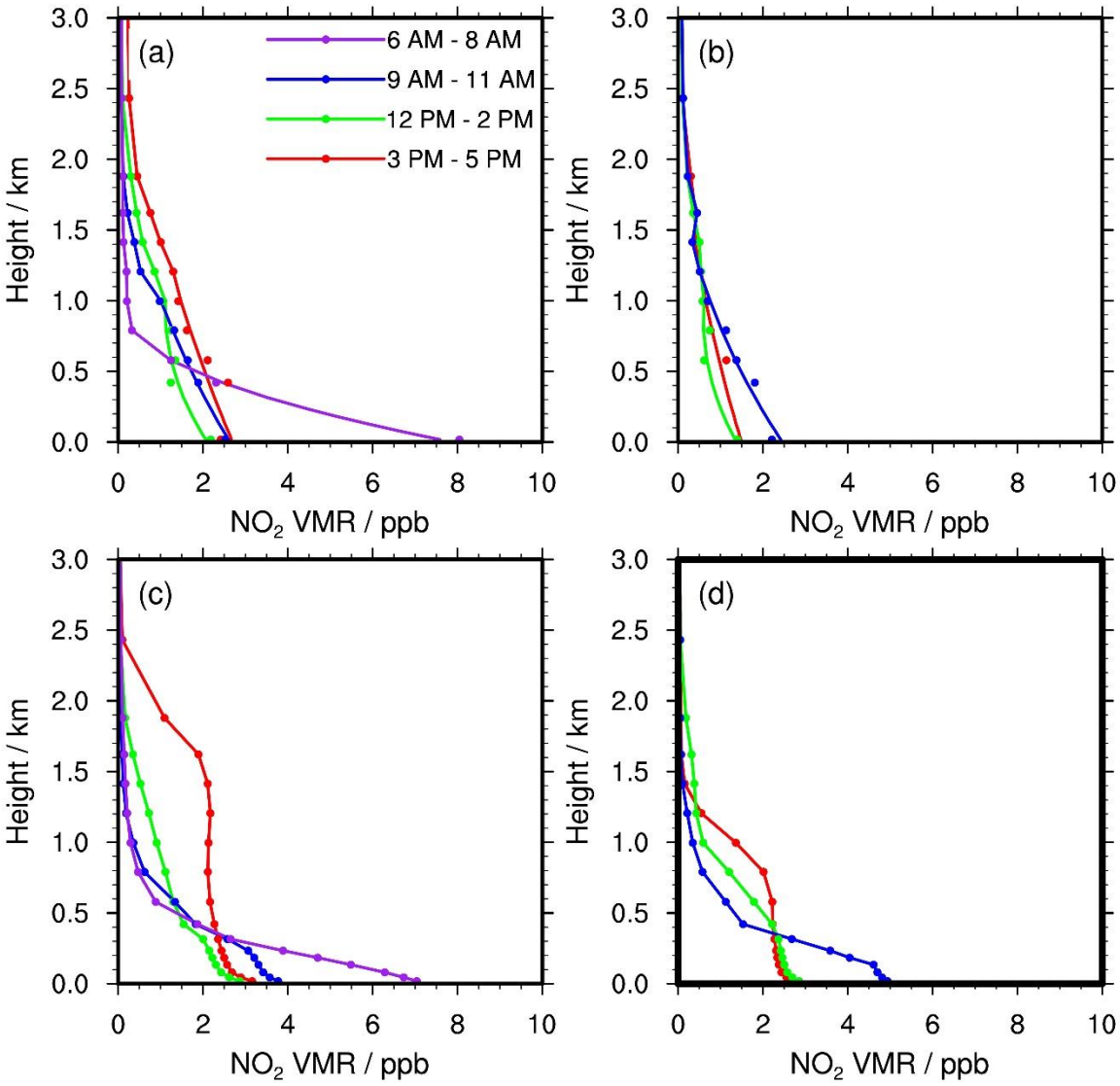

Figure 2. 14 Diurnal variations of NO_2 vertical profiles on weekdays (a, c) and weekends (b, d) from aircraft observations (a, b) and coincident 4-REAM simulated results (c, d).

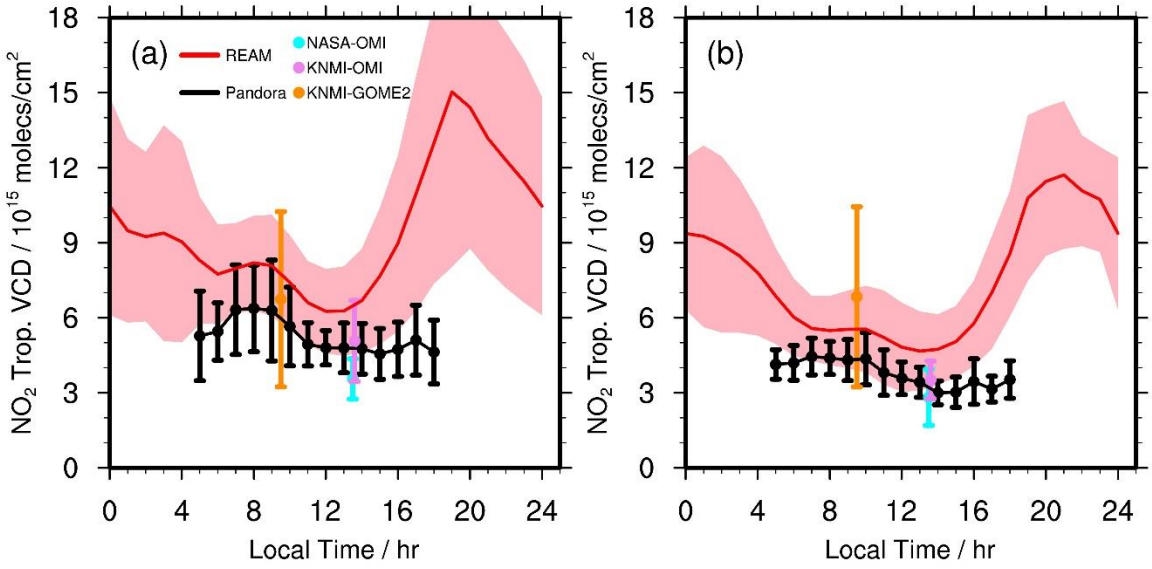

Figure 2. 15 Diurnal variations of NO_2 TVCD on weekdays (a) and weekends (b) at 4 km scale. Pandora refers to updated Pandora TVCD which includes the NO_2 VCD below Pandora instruments. "NASA-OMI" is the OMI NO_2 TVCD retrieved by NASA; "KNMI-OMI" is the OMI NO_2 TVCD from KNMI; "KNMI-GOME2" is the GOME2 TVCD from KNMI.

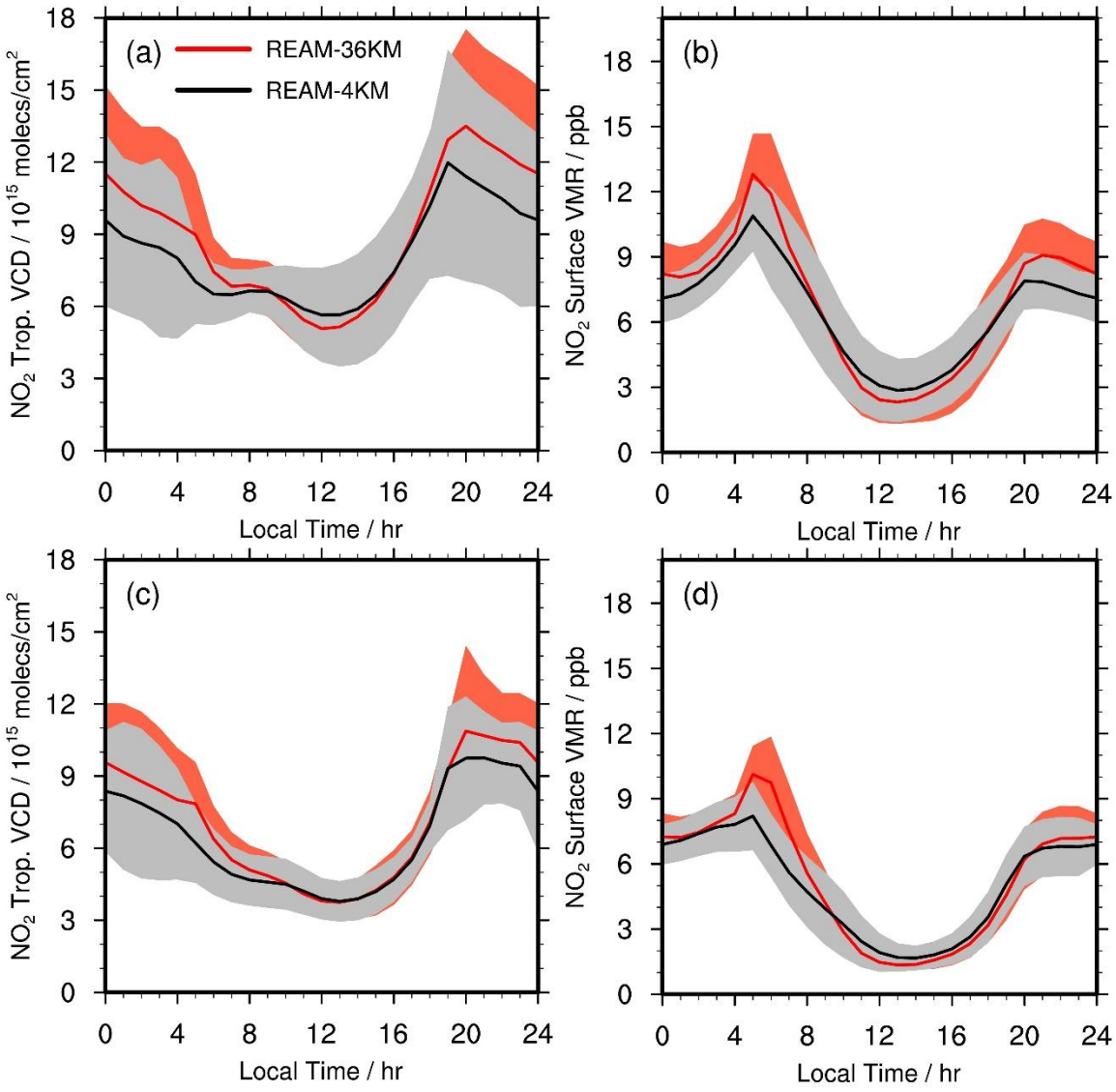

Figure 2. 16 Comparison between NO_2 re-gridded from the 4-km REAM results and NO_2 from the 36-km REAM on weekdays (a, b) and weekends (c, d). (b) and (d) are for surface NO_2 concentrations, while (a) and (c) are for NO_2 TVCD.

CHAPTER 3. Dependence of summertime surface ozone on NO_x and VOC emissions over the United States: Peak time and value

3.1 Introduction

Surface ozone (O_3), one of the six criteria air pollutants regulated by the U.S. Environmental Protection Agency (EPA), is also a greenhouse gas [*Myhre et al.*, 2013] and can adversely affect human health and vegetation [*Glowacz et al.*, 2015; *Jerrett et al.*, 2009; *S. Li et al.*, 2017; *Turner et al.*, 2016]. O_3 is a secondary pollutant, which is produced by complicated photochemistry reactions with the presence of NO_x (NO_x = NO + NO_2) and volatile organic compounds (VOCs) (Figure 3.4) [*Liu et al.*, 2012a; *Seinfeld and Pandis*, 2016]. NO_x and VOCs are emitted by both anthropogenic activities (vehicles, power plants, industry, etc.) and natural sources (soil NO_x, lightning NO_x, and biogenic VOCs (BVOCs)). Globally, isoprene emitted by vegetation is the most abundant non-methane VOC (535 Tg yr^{-1} for the year 2000) [*Guenther et al.*, 2012], while anthropogenic NO_x contribute about 75% of the total NO_x emissions [*Seinfeld and Pandis*, 2016].

The relationship between O_3 production and VOC and NO_x emissions is essential to understand tropospheric chemistry and has been widely studied in recent decades [*Cheng et al.*, 2017; *Cheng et al.*, 2018; *Liu et al.*, 2012a; *Xie et al.*, 2011]. For example, *Pierce et al.* [1998] examined the sensitivities of O_3 concentrations to isoprene and NO_x emissions in the Regional Acid Deposition Model (RADM) simulations with different emission scenarios in the eastern United States, and found that increased isoprene emissions

produce a shift in elevated O_3 concentrations from VOC sensitivity to NO_x sensitivity over many areas of eastern North America. *Gao* [2007] analyzed surface O_3 and NO_x diurnal cycles and VOC and NO_x emissions from heavy-duty trucks (HDT) and low-duty vehicles (LDV) in California, and demonstrated that an O_3 weekend effect with higher O_3 concentrations on weekends compared to weekdays in urban regions is induced by a weekend increase in the ratio of transportation VOC to NO_x emissions which results from decreased HDT activity relative to LDV. *Mazzuca et al. [2016]* investigated the diurnal variation in the sensitivities of ozone production rate to NO_x and VOCs in September 2013 by using the observations from the NASA Deriving Information on Surface Conditions from COlumn and VERtically Resolved Observations Relavant to Air Quality (DISCOVER-AQ) Houston campaign and the model simulations from a box model and the Community Multiscale Air Quality (CMAQ) model. They found that O_3 production shifts from generally being more VOC-sensitive in the morning to mainly NO_x-sensitive in the afternoon during the campaign. *R. Zhang et al.* [2017a] evaluated the contributions of BVOC emissions to O_3 through Ozone Source Apportionment Technology and brute force zero-out sensitivity tests over the United States and found that BVOCs typically contribute 10 - 19% to regional O_3 concentrations at the nonattainment sites during selected O_3 episodes. In general, the O_3-VOC-NO_x relationship can be categorized into two regimes: NO_x-limited regime, where O_3 is more sensitive to NO_x than to VOCs and reducing NO_x emissions is more effective in lowering O_3, and VOC-limited regime, where O_3 is more sensitive to VOCs.

In this study, we investigate a new constraint on the O_3-NO_x-VOC relationship using the sensitivity of O_3 peak time (the time when O_3 reach its maximum in one day) to NO_x

and VOC emissions, in addition to previously used O_3 concentrations. This new relationship provides another diagnostic of O_3 sensitivity on NO_x and VOC emissions. The observations and modeling of July 2011 over the contiguous United States (CONUS) are analyzed to demonstrate the new O_3-NO_x-VOC relationship and its applications. The Regional chEmical and trAnsport Model (REAM), O_3 surface observations, and other data sets are described in Section 3.2. In Section 3.3, we analyze the dependences of O_3 peak time and the peak value (the maximum hourly concentration of O_3 in one day) on NO_x and VOC emissions through sensitivity tests with different emission scenarios. Making use of the dependences, we analyze the discrepancies of O_3 peak time and peak values between REAM simulations and the observations in order to evaluate the emission inventories in the model. Conclusions are given in section 3.4.

3.2 Observation Data and Model Description

3.2.1 Surface ozone observations

We obtained O_3 surface concentration measurements in July 2011 from the EPA Air Quality System (AQS) Data Mart (https://www3.epa.gov/airdata/) and converted them into O_3 peak values and peak time in local time. Data at 1024 observation sites are available and used in this study. The CONUS was divided into 9 regions following the definition of the National Oceanic and Atmospheric Administration (NOAA) (http://www.ncdc.noaa.gov/monitoring-references/maps/us-climate-regions.php) [*Karl and Koss*, 1984]. Figure 3.1 shows the regions and the distribution of the O_3 observations sites. There were 185, 63, 196, 146, 148, 30, 134, 77, and 45 sites in Central, East North

Central, Northeast, South, Southeast, Northwest, Southwest, West and West North Central, respectively.

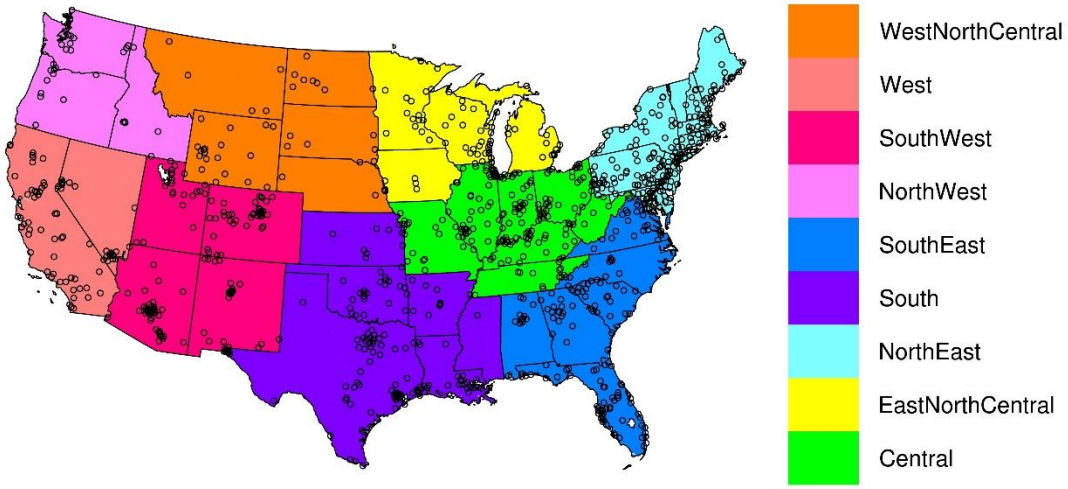

Figure 3. 1 Region definitions and locations of EPA AQS O_3 monitoring sites. Site locations are shown with open circles.

3.2.2 OMI HCHO tropospheric vertical columns

The Ozone Monitoring Instrument (OMI) is an ultraviolet/visible nadir solar backscatter spectrometer onboard NASA EOS-Aura sun-synchronous polar satellite, which was launched in July 2004. It crosses the equator around 13:30 local time. OMI provides tropospheric HCHO column observations with nearly daily global coverage and a nadir spatial resolution of 13 km × 24 km [*Levelt et al.*, 2006b]. Here, we use the newest OMI HCHO version 14 (OMI-v14) level-3 product with a resolution of 0.25° × 0.25° (http://h2co.aeronomie.be/). In the retrieval of OMI-v14, a priori profile shapes

extracted from the Intermediate Model of Global Evolution of Species version 2 (IMAGESv2) are used to calculate air mass factors [*De Smedt et al.*, 2015]. The IMAGESv2 model reproduces very well observed vertical profiles of HCHO measured during the Intercontinental Chemical Transport Experiment North America (INTEX-A) campaign (July – August 2004) over the US [*De Smedt et al.*, 2015; *Stavrakou et al.*, 2009]. Using the HCHO vertical shape from the Compact Atmospheric Multispecies Spectrometer (CAMS) measurements during the SEAC^{4}RS (Studies of Emissions, Atmospheric Composition, Clouds and Climate Coupling by Regional Surveys) aircraft campaign (August - September 2013) in the OMI-v14 retrieval algorithm, HCHO columns are increased by about 10% in the southeastern US [*Zhu et al.*, 2016]. *Zhu et al.* [2016] suggested that OMI-v14 offers the best estimation of tropospheric HCHO columns in the southeastern US compared to GOME2A-BIRA (V14), GOME2B-BIRA (V14), OMPS-SAO, OMPS-PCA and OMI-SAO (V003), although OMI-v14 still underestimates the columns by 20% compared to CAMS derived HCHO columns. On the other hand, *De Smedt et al.* [2016] demonstrates that the precision (random error) of OMI-v14 is below 7×10^{14} molecules cm^{-2} in July (which is about 5% for the southeastern US) when considering monthly average columns with a resolution of 20 km × 20 km and that the accuracy (systematic error) of OMI-v14 is about 20% over the Southeastern US.

HCHO is an intermediate product of isoprene oxidation, and HCHO columns provide a proxy for isoprene emissions [*Palmer et al.*, 2003; *Shim et al.*, 2005]. In this study, OMI-v14 HCHO columns are used to evaluate the isoprene emission inventory

from the Model of Emissions of Gases and Aerosols from Nature (MEGAN) [*Guenther et al.*, 2012].

3.2.3 Model description

3.2.3.1 REAM

REAM has been applied in many tropospheric chemistry and transport studies and emission estimations over East Asia, North America and polar regions [*Alkuwari et al.*, 2013; *Cheng et al.*, 2017; *Cheng et al.*, 2018; *Y. Choi et al.*, 2008a; *Y. Choi et al.*, 2008b; *Gu et al.*, 2014; *Gu et al.*, 2013; *Koo et al.*, 2012; *Liu et al.*, 2014; *Liu et al.*, 2012b; *Yuhang Wang et al.*, 2007; *Q. Yang et al.*, 2011; *R. Zhang et al.*, 2017b; *R. Zhang et al.*, 2018; *Y. Zhang and Wang*, 2016; *C. Zhao and Wang*, 2009; *C. Zhao et al.*, 2009a; *C. Zhao et al.*, 2010]. The model has a horizontal resolution of 36 km × 36 km with 30 vertical layers in the troposphere. Transport is driven by the Weather Research and Forecasting (WRF, version 3.6) model-assimilated meteorological fields constrained by the NCEP coupled forecast system model version 2 (CFSv2) products (http://rda.ucar.edu/datasets/ds094.0/) [*Saha et al.*, 2011]. The chemistry mechanism is from the GEOS-Chem model (v11.01) with updated aerosol uptake of isoprene nitrate based on *Fisher et al.* [2016]. Chemistry boundary conditions and initiations are from a GEOS-Chem simulation with a resolution of 2° × 2.5°. Anthropogenic NO_x, CO and VOC emissions are from the National Emission Inventory 2011 (NEI2011) provided by the Pacific Northwest National Laboratory (PNNL). We assume that the weekend emissions are two-thirds of the weekday emissions [*Y. Choi et al.*, 2012; *Kaynak et al.*, 2009]. This study focuses on weekday analysis and the weekend emission uncertainty is

out of the scope of this study and has little impacts on weekday O_3 peak values and peak time because of the short lifetimes of O_3 and its precursors, VOCs and NO_x. Biogenic VOC emissions are from MEGAN v2.1 [*Guenther et al.*, 2012]. Soil emitted NO_x is calculated by using the Yienger and Levy (YL) scheme [*Yienger and Levy*, 1995].

3.2.3.2 MEGAN v2.1

MEGAN [*Guenther et al.*, 2012; *Guenther et al.*, 2006] is currently widely used to estimate global and regional BVOC emissions [*Fisher et al.*, 2016; *Mao et al.*, 2013; *Stavrakou et al.*, 2014; *Yu et al.*, 2016]. In this study, we use a recommended high-resolution plant functional type database for the U.S. for the year 2008 (http://lar.wsu.edu/megan/guides.html). Land coverage data is from the GLASS Leaf Area Index (LAI) product with a raw resolution of 0.05° (download from ftp://ftp.glcf.umd.edu/glcf/GLASS/LAI/MODIS/0.05D/), and the GLASS LAI product is derived from MODIS land surface reflectance (MOD09A1) [*Liang and Xiao*, 2012; *Xiao et al.*, 2014]. Meteorological parameters, such as temperature, soil moisture, and radiation flux, are from a WRF simulation.

3.3 Results and Discussions

3.3.1 Dependence of O_3 peak values and time on NO_x and VOCs

To evaluate the dependence of O_3 peak time and values on NO_x and VOC emissions, we made 17 sensitivity simulations with different emission scenarios by using REAM, including STD-REAM where standard anthropogenic and natural NO_x and VOC emissions were used, natural scenarios with varying BVOC or soil NO_x emissions,

anthropogenic scenarios with different anthropogenic NO_x or VOC emissions, and combination scenarios where more than two types of emissions were changed. The responses of weekday monthly mean O_3 peak time and peak values to NO_x and VOC emission variations, as well as complete descriptions of the emission scenarios, are illustrated in Figures 3.2 and 3.5. Figure 3.2 shows that the sensitivities of regional O_3 peak time to NO_x and VOC emissions differ significantly from those of O_3 peak values. For example, in Central CONUS, O_3 peak time responds to VOC emission changes while O_3 peak value responds to NO_x emission changes. Therefore, the observations of O_3 peak time provides another set of constraints on model simulations in addition to O_3 peak values (next section). We first discuss the dependence of O_3 peak value on NO_x and VOC emissions.

Generally, anthropogenic NO_x emissions showed positive correlations with regional ozone peak values (Figure 3.2). The effects of anthropogenic NO_x emissions on peak values were more significant in East North Central, Central, Northeast, South, and Southeast than in the other regions. Soil NO_x emissions affect regional O_3 peak values in a manner similar to anthropogenic NO_x emissions. Therefore, the relative importance of the two NO_x sources depends on their relative emission strengths. Soil NO_x dominates in most areas of the western CONUS while anthropogenic NO_x is predominant in the eastern regions (Figure 3.6). As a result, increasing soil NO_x emissions by 400% has fewer impacts on O_3 peak values in Southeast and Northeast than increasing anthropogenic NO_x emissions by 50%, while the two effects are comparable in Central and South CONUS. The former has a larger effect in East North Central, Northwest, Southwest, West, and West North Central CONUS.

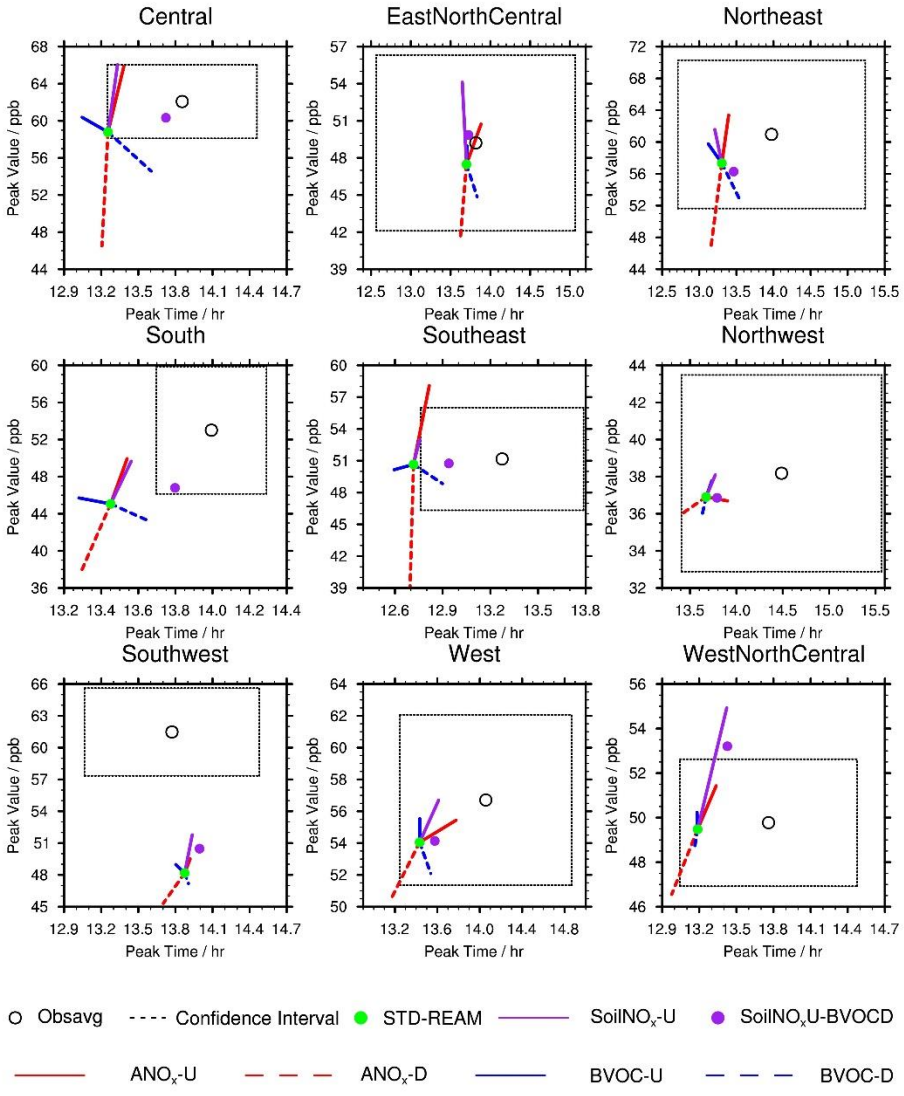

Figure 3. 2 Comparison of weekday monthly mean O_3 peak values and peak time between EPA observations and REAM simulations with different emission scenarios in July 2011 over different regions (Figure 3.1). "Obsavg" denotes EPA observations. The "Confidence Interval" box is calculated based on the 99.9% confidence intervals. STD-REAM denotes the standard simulation result without any emission changes. "SoilNO$_x$-U" is the sensitivity simulation result after increasing soil NO$_x$ emissions to five times. "ANO$_x$-U" and "ANO$_x$-D" are for increasing and decreasing anthropogenic NO$_x$ by 50%, respectively. "BVOC-U" and "BVOC-D" are for increasing and decreasing MEGAN isoprene emissions by 50%, respectively. "SoilNO$_x$U-BVOCD" denotes a sensitivity simulation with MEGAN isoprene emissions decreased by 50% and soil NO$_x$ emissions increased to five times. Additional sensitivity simulation results are shown in Figure 3.5.

The effects of BVOCs are more apparent than anthropogenic VOCs (Figures 3.2 and 3.5). For BVOCs, the correlations between O_3 peak value and emissions are positive in all regions except for in Southeast, where a slight decrease is simulated when BVOC emissions are changed by 50%, reflecting the nonlinear O_3 photochemistry in this region of abundant isoprene emissions. Since both VOCs and NO_x show positive correlations with O_3 peak values, concurrent increase (decrease) of NO_x and VOC emissions could elevate (lower) O_3 peak values more as shown by combination sensitivity scenarios in Figure 3.5. However, it should be noted that O_3 peak values were much more sensitive to NO_x than VOC emissions in East North Central, Central, Northeast, South, and Southeast. That is to say, these regions are in NO_x-limited regime, which is consistent with the relatively high BVOC emissions in these areas (Figure 3.7). In West, West North Central, Southwest, and Northwest, the effects of NO_x and VOC emission changes on O_3 peak values are comparable, but both are significantly weaker than those in the former five regions, due in part to relatively lower NO_x and VOC emissions in these regions and transport factors controlling surface O_3 levels such as stratospheric O_3 intrusion [*Langford et al.*, 2009; *Musselman and Korfmacher*, 2014].

Figure 3.2 shows that O_3 peak time is positively correlated with anthropogenic NO_x emissions. As in anthropogenic NO_x, the effects of soil NO_x emissions are generally more significant on O_3 peak values than peak time. VOC emission changes, in general, affect O_3 peak time more than NO_x emissions, but the relationships are somewhat complicated. Generally, O_3 peak time is negatively correlated with BVOC emissions (Figures 3.2 and 3.5) in most regions, and it is most significant in Central, Northeast, South, and Southeast, where BVOC emissions are much higher than the other regions (Figure 3.7).

In the other regions, BVOC effects are relatively small. Figure 3.5 shows that the effects of anthropogenic VOC emissions are also small.

In Central, Northeast, South, and Southeast, O_3 peak value is more sensitive to NO_x emissions but O_3 peak time is more sensitive to VOC (mostly BVOC) emissions (Figure 3.2). In these regions, O_3 peak time is negatively correlated with VOC emissions. With sufficient BVOC emissions, it is not surprising that O_3 peak values in the regions are more sensitive to NO_x than VOC emissions. Different sensitivities in O_3 peak time from peak values reflect the O_3 photochemical process (Figure 3.4). As shown in Figure 3.8, BVOC and NO_x emissions have opposite impacts on diurnal cycles of NO, RO_2, and HO_2 concentrations: decreasing BVOC emissions decreases HO_2 and RO_2 concentrations and increases NO concentrations while decreasing NO_x increases HO_2 and RO_2 concentrations and reduces NO concentrations in the morning. Since RO_2 and HO_2 concentrations are changed more significantly than NO concentrations in the early morning, BVOC and NO_x emissions have opposite effects on the daytime O_3 production ($P(O_3) = k_1[RO_2][NO] + k_2[HO_2][NO]$): decreasing BVOC and increasing NO_x emissions shifts the accumulated $P(O_3)$ profile later in time while increasing BVOC and decreasing NO_x emissions shifts the accumulated $P(O_3)$ profile earlier in time.

Figure 3.8 also shows that the change of BVOC emissions affects accumulated $P(O_3)$ profile more significantly than that of NO_x emissions, especially for decreasing BVOC emissions. The main reason is their different effects on NO concentrations from 5:00 – 8:00 when NO concentrations are changed much more significantly for the NO_x emission sensitivity simulations than for the BVOC emission sensitivity simulations,

which partially offsets the changes of RO_2 and HO_2. It reflects the direct impact of NO_x emissions on NO concentrations when photochemistry is weak in the early morning. There is no significant pattern difference for RO_2 and NO_2 concentrations from 5:00 – 13:00 between BVOC and NO_x sensitivity simulations except that: 1) decreasing BVOC emissions reduces RO_2 and HO_2 concentrations much more (about 50%) than increasing NO_x emissions, which means decreasing BVOC emissions shifts accumulated $P(O_3)$ profile much more significantly than increasing NO_x emissions; 2) decreasing NO_x emissions increases RO_2 and HO_2 concentrations some more (about 20%) than increasing BVOC emissions. However, its effect on accumulated $P(O_3)$ profile is canceled out by the effect of NO concentration change difference in the early morning. Therefore, decreasing BVOC emissions and increasing NO_x emissions shift the accumulated $P(O_3)$ profile later in time and delay O_3 peak time and the sensitivity of O_3 peak time to BVOC emission change is higher than NO_x (Figures 3.8 and 3.9).

The sensitivities of O_3 peak time to NO_x and BVOC emissions were also found previously by *Lei et al.* [2007] and *Lei et al.* [2008]. They investigated the sensitivities of O_3 production to NO_x and VOC emissions in April 2003 in the Mexico City Metropolitan Area (MCMA). Even though MCMA is a VOC-limited region, their sensitivity simulations also showed that O_3 peak shifted to earlier hours with reduced NO_x emissions and later hours with reduced VOC emissions. Therefore, the utilities of the sensitivities of O_3 peak time to NO_x and BVOC emissions discussed in this study are likely extendable to other seasons and regions.

3.3.2 Application of the O_3-NO_x-VOC relationships to evaluate model VOC and NO_x emissions

As discussed in the previous section, the sensitivities of O_3 peak values and time to NO_x and VOC emissions are often quite different, therefore providing independent constraints on model simulations. Figure 3.2 shows that the standard model simulates well on the observed O_3 peak values in most regions but underestimates them in South and Southwest. The model generally reproduces O_3 peak time within the 99.9% confidence intervals in most regions except for Central, South, and Southeast where the simulated O_3 peak time is significantly earlier than the observations.

The large set of sensitivity simulations (Figures 3.2 and 3.5) point to possible problems in the model NO_x and BVOC emissions, although the model underestimates of O_3 peak values in the Southwest region cannot be easily corrected without increasing soil NO_x emissions by a factor of 10-50, implying that transport of O_3 from the upper troposphere may be underestimated. For the Central and Southeast regions, observed O_3 peak values are simulated well by the standard model. The relatively high sensitivity of O_3 peak values to NO_x emissions in these regions implies that emissions of NO_x are reasonable. The O_3 peak time simulated by the model, on the other hand, is earlier than the observations. Model sensitivity simulations suggest that O_3 peak time is sensitive to BVOC emissions since anthropogenic VOC emissions are much lower than BVOCs in these regions and reducing BVOC emissions reduces the simulation bias in O_3 peak time.

For the South region, the simulated O_3 peak value is lower and peak time is earlier than the observations, suggesting an increase of NO_x emissions and a decrease of BVOC

emissions (Figure 3.2). It is noteworthy that the underestimation of O_3 peak values mainly occur in the upper South (Figure 3.10), where soil NO_x emissions are close or even much higher than anthropogenic NO_x emissions (Figure 3.6). Several studies demonstrated that the YL scheme underestimated soil NO_x emissions by a factor of 2 - 4 [*Hudman et al.*, 2012; *Jaeglé et al.*, 2005; *Rasool et al.*, 2016; *Wolfe et al.*, 2015] over the United States. Increasing YL soil NO_x emissions by a factor of 5 brings the simulated regional O_3 peak value closer to the observations, in agreement with the previous studies.

The increase of soil NO_x emissions delays the O_3 peak time. However, the model simulated O_3 peak time in the South region is still earlier than the observations. Model sensitivity results in Figure 3.2 suggest that a decrease of BVOC emissions by 50% is necessary. Previous studies showed that MEGAN might overestimate BVOC emissions in some regions of the United States. For example, [*Wolfe et al.*, 2015] demonstrated that MEGAN v2.1 overestimated isoprene surface fluxes by up to 40% based on the measurements during the NASA SEAC^{4}RS mission over the Ozarks. *Carlton and Baker* [2011] indicated that MEGAN v2.04 led to much higher isoprene concentrations than the surface and aloft measurements in July 1998 in the Ozarks region. Top-down constraints from satellite HCHO measurements, such as OMI, provide an independent means to evaluate the bottom-up isoprene emissions from MEGAN, although the HCHO yield from isoprene oxidation could lead to some uncertainties [*Marais et al.*, 2012]. In the next section, we examine the simulated isoprene emissions based on OMI HCHO column measurements.

Our evaluation of the NEI2011 NO_x emissions is consistent with the results by *Salmon et al.* [2018], who examined the NO_x/CO_2, CO/CO_2, and CO/NO_x ratios in February-March 2015 over the northeastern United States and found that NO_x emissions from NEI2011 and NEI2014 were in agreement with the aircraft observation-derived emissions. *Cheng et al.* [2017] also found good agreement between model simulations and aircraft observations of O_3, NO_x and VOCs in July 2011 around the Washington-Baltimore area. However, *Canty et al.* [2015], *Travis et al.* [2016], and *Anderson et al.* [2014] suggested that on-road mobile sources in the NEI NO_x emissions inventories were overestimated by around 50% - 70% in 2007 and 2011, while *Dallmann and Harley* [2010] suggested that on-road mobile NO_x emissions from NEI2005 were 15% lower than fuel-derived on-road NO_x emissions. The different evaluations of NEI NO_x emissions might be caused by the limitations of the datasets used to assess the NEI emissions, such as the temporal-spatial coverage of measurements, which would bias the evaluations due to significant inhomogeneity of NO_x emissions *Marr et al.* [2013], measurement uncertainties, and differences in evaluation methods.

3.3.3 Constraints of OMI-v14 tropospheric HCHO column measurements on isoprene emissions

Figure 3.3.a shows the monthly average of STD-REAM tropospheric HCHO columns at 12:30 – 14:30 LT in July 2011. The corresponding re-gridded OMI-v14 HCHO columns based on the model resolution are shown in Figure 3.3.b. The relative difference (REAM/OMI – 1) is shown in Figure 3.3.c. STD-REAM captured the spatial distribution of HCHO columns ($R^2 = 0.62$) with high column concentrations in Central, South, and Southeast where there are dense forests. However, STD-REAM simulates

much higher columns than OMI-v14 in these regions. Over the model grid cells where surface O_3 observation sites are available in Central, South, and Southeast, the STD-REAM tropospheric HCHO columns are about 36.9% higher than the corresponding OMI-v14 columns on average, and 29.7%, 37.8%, and 46.0% for Central, South, and Southeast, respectively.

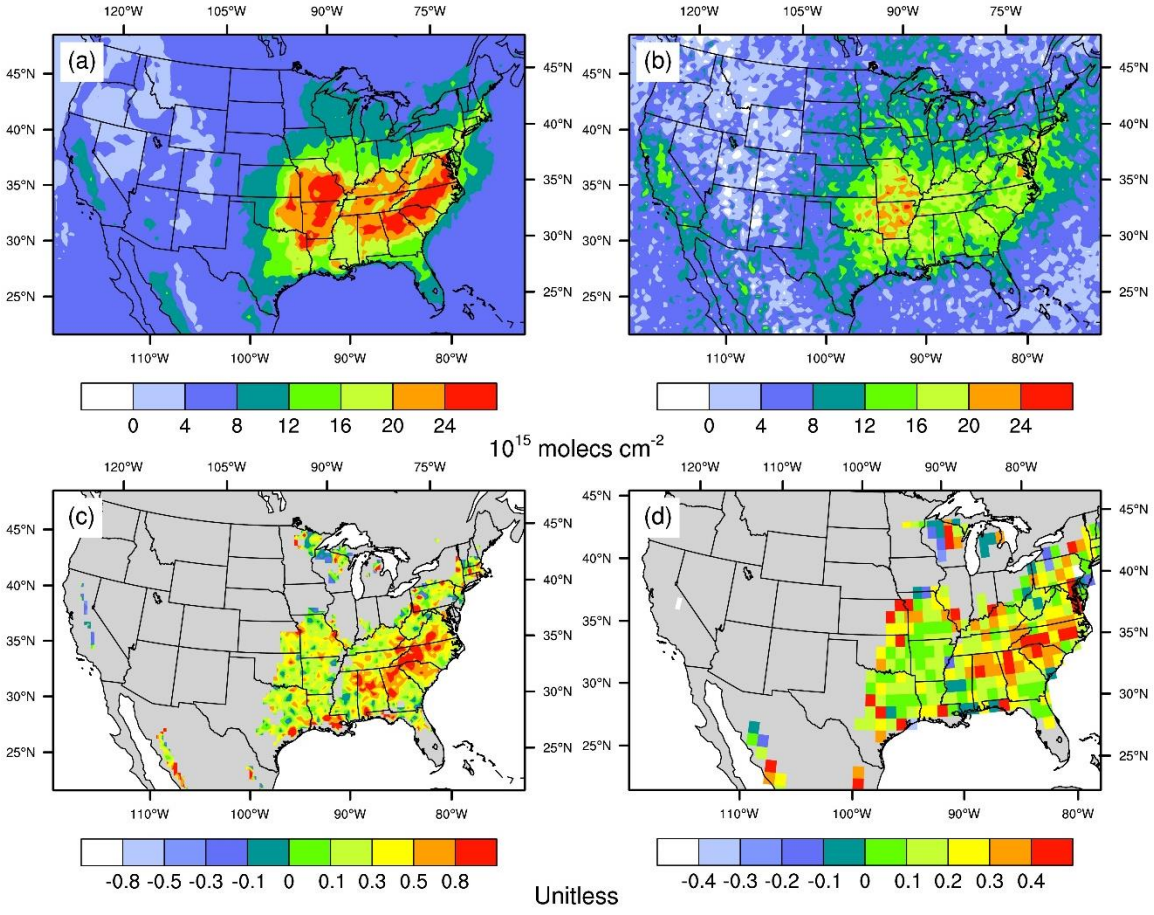

Figure 3. 3 Spatial distribution of (a) tropospheric HCHO vertical columns of STD-REAM between 12:30 – 14:30 LT, (b) tropospheric HCHO vertical columns of OMI-v14 retrievals, (c) relative difference between STD-REAM and OMI-v14 (REAM/OMI - 1); (d) the relative difference of the MEGAN isoprene emissions from those derived from OMI-v14 HCHO column data for regions with MEGAN isoprene emissions > 3×10^{12} atoms C cm^{-2} s^{-1}. All data shown are monthly averages for July 2011.

HCHO is mainly produced during the oxidation of biogenic isoprene, and HCHO column observations from space are highly specific to biogenic isoprene in Central, South, and Southeast [*Millet et al.*, 2008; *Shim et al.*, 2005]. A quantified relationship between biogenic isoprene emissions and HCHO tropospheric columns at 12:00 – 15:00 LT was derived by *Millet et al.* [2008]:

$$\Omega_{HCHO} = 2.40\, E_{ISOPRENE} + 0.51 \qquad (3.1)$$

where Ω_{HCHO} denotes tropospheric HCHO columns in 10^{16} molecules cm^{-2}, and $E_{ISOPRENE}$ denotes biogenic isoprene emissions in 10^{13} atoms C cm^{-2} s^{-1}. Therefore, the top-down constraint on an a priori emission inventory can be calculated by,

$$\Delta\Omega_{HCHO} = 2.40\, \Delta E_{ISOPRENE} \qquad (3.2)$$

In order to reduce the smearing effect [*Millet et al.*, 2008], we re-gridded 36 km × 36 km data to a resolution of 1° × 1°. If we only included those grids containing the observations sites in Central, South, and Southeast, STD-REAM tropospheric HCHO column was 31.5% or 0.41×10^{16} molecules cm^{-2} higher than OMI-v14 on average, corresponding to a biogenic isoprene emission bias of 1.71×10^{12} atoms C cm^{-2} s^{-1}. As a result, the MEGAN isoprene emissions are overestimated by 27.2% on average in these regions, and 30.4%, 21.3%, and 28.9% for Central, South, and Southeast, respectively. Figure 3.3.d shows the distribution of the factional overestimation of isoprene emissions. These results are consistent with *Millet et al.* [2008], who suggested that isoprene emissions derived from OMI HCHO columns were 23% lower than MEGAN from June to August, and the absolute differences were the largest in the Ozark Plateau, the Upper South and Southeast where MEGAN overestimation could reach up to about 50%. Accounting for the uncertainty of OMI HCHO columns of ~25%, we estimate that the overestimation of

MEGAN isoprene emissions in July 2011 is in the range of 5.6% - 48.6% in Central, South, and Southeast, which provides additional support to the previous results on the basis of model-simulated peak O_3 time and values in comparison to the observations for these regions.

3.4 Conclusions

We evaluated the dependence of O_3 peak values and time on NO_x and VOC emissions through model simulations with different emission scenarios in July 2011 over the CONUS. In addition to the previously known dependence of O_3 peak values on NO_x and VOC emissions, we find that O_3 peak time is affected by NO_x and VOC emissions in a different manner. As such, the observations of O_3 peak values and time provide useful constraints on model emissions of NO_x and VOCs. Over regions with extensive biogenic isoprene emissions, such as the Central, South, Southeast, and Northeast regions, the O_3 peak values are sensitive to the emissions of NO_x but not VOCs. However, O_3 peak time in these regions is sensitive to isoprene emissions, where an increase of isoprene emissions leads to earlier peak time of surface O_3.

We applied these O_3 dependences to analyze REAM performance on reproducing the observations of surface O_3 peak values and time in July 2011 over the CONUS. REAM reproduced well O_3 peak values and peak time in most regions except in the South and Southwest, where peak values were significantly underestimated, and in the Central, South, and Southeast, where peak time was earlier than observed. The underestimation of soil NO_x emissions from the Yienger and Levy (YL) scheme could be the reason for the O_3 peak value underestimation in the South. However, it is insufficient

to explain the low bias of O_3 peak value in the Southwest, suggesting an underestimation of O_3 transport from the upper troposphere. The earlier than observed O_3 peak time in the Central, South, and Southeast was attributed to an overestimation of biogenic isoprene emissions by MEGAN, which was consistent with the estimate of a 27.1% ± 21.5% overestimation of isoprene emissions in these regions in July 2011 on the basis of OMI HCHO column observations. As our study is limited in July 2011 over the CONUS, evaluations of O_3 peak time and value sensitivities to NO_x and VOC emissions are needed for other seasons and regions. Given the sensitivities found in this study for the summertime, we recommend that the dependence of O_3 peak time on NO_x and VOC emissions be applied to evaluate model emissions in conjunction with the often-used evaluation of O_3 concentrations.

3.5 Supporting materials

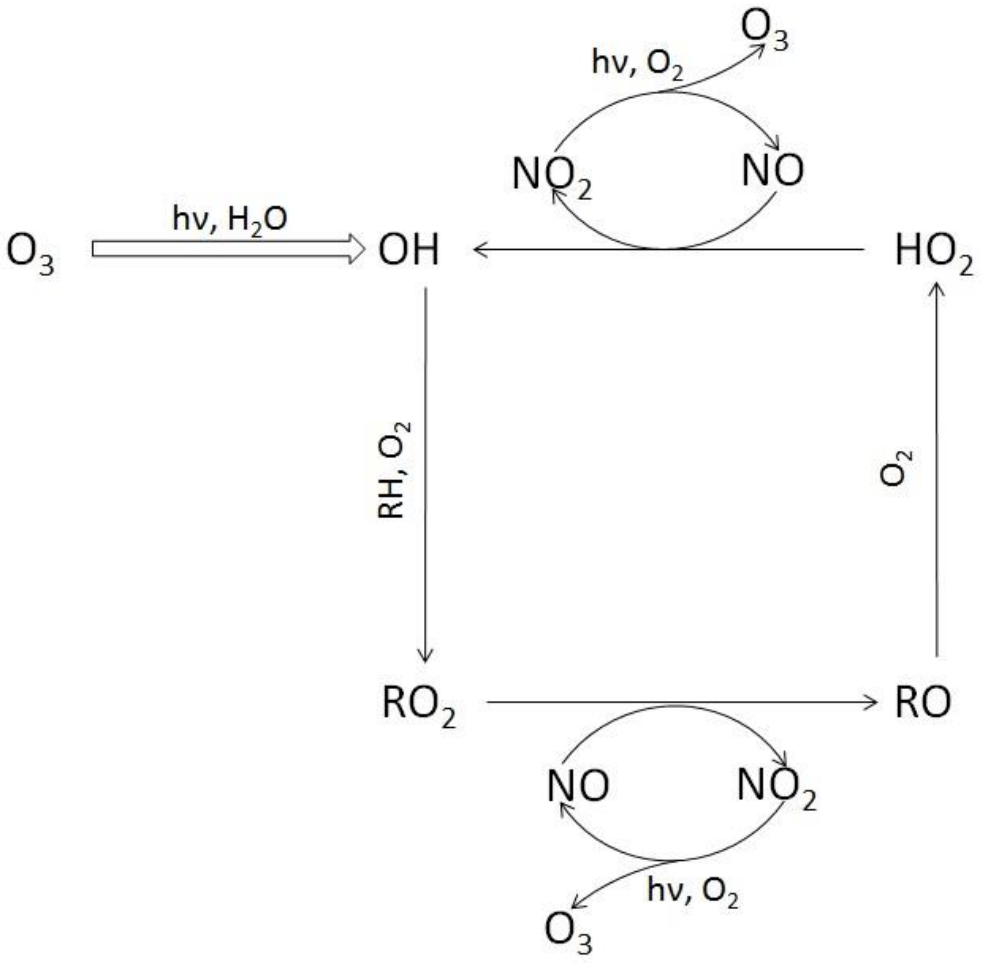

Figure 3. 4 A schematic illustration of simplified tropospheric O_3-VOC-NO_x chemistry.

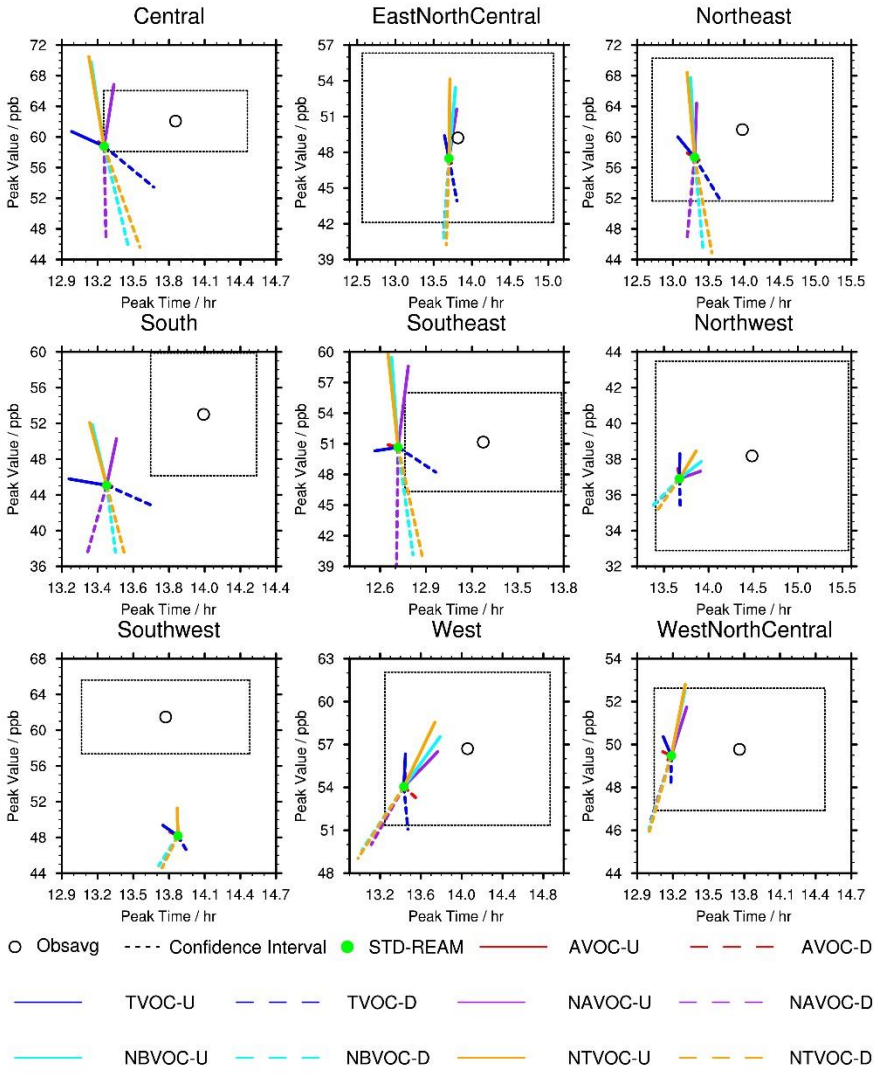

Figure 3. 5 Same as Figure 3.2. The suffix, "U", denotes increasing the specified emissions by 50%, while "D" denotes decreasing emissions by 50%. AVOC denotes anthropogenic VOC emissions. TVOC denotes the sum of biogenic isoprene emissions and anthropogenic VOC emissions. NAVOC denotes both anthropogenic NO_x and VOC emissions. NBVOC denotes both anthropogenic NO_x emissions and BVOC emissions. NTVOC denotes both anthropogenic NO_x emissions and total VOC emissions (including biogenic VOC emissions).

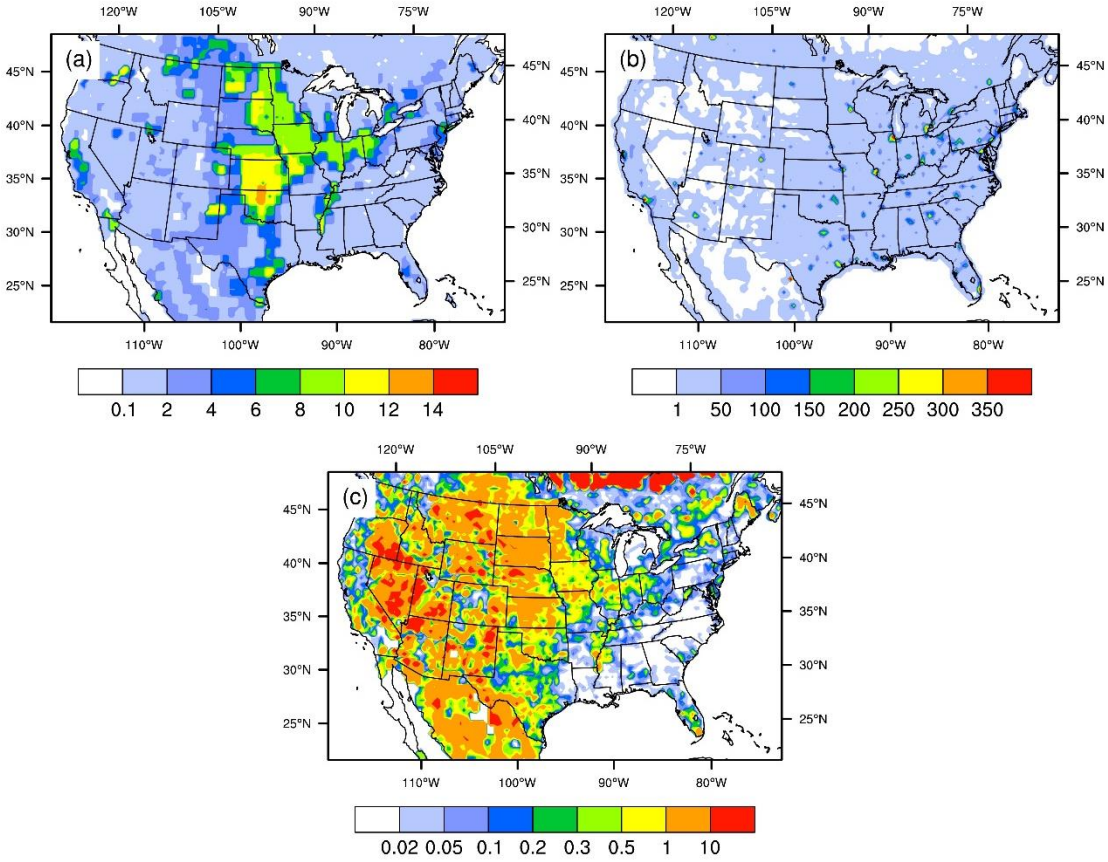

Figure 3. 6 Comparison between soil NO_x and anthropogenic NO_x emissions (unit: $ng \cdot m^{-2} \cdot s^{-1}$) for July 2011: (a) soil NO_x; (b) anthropogenic NO_x; (c) the ratio of soil NO_x to anthropogenic NO_x emissions.

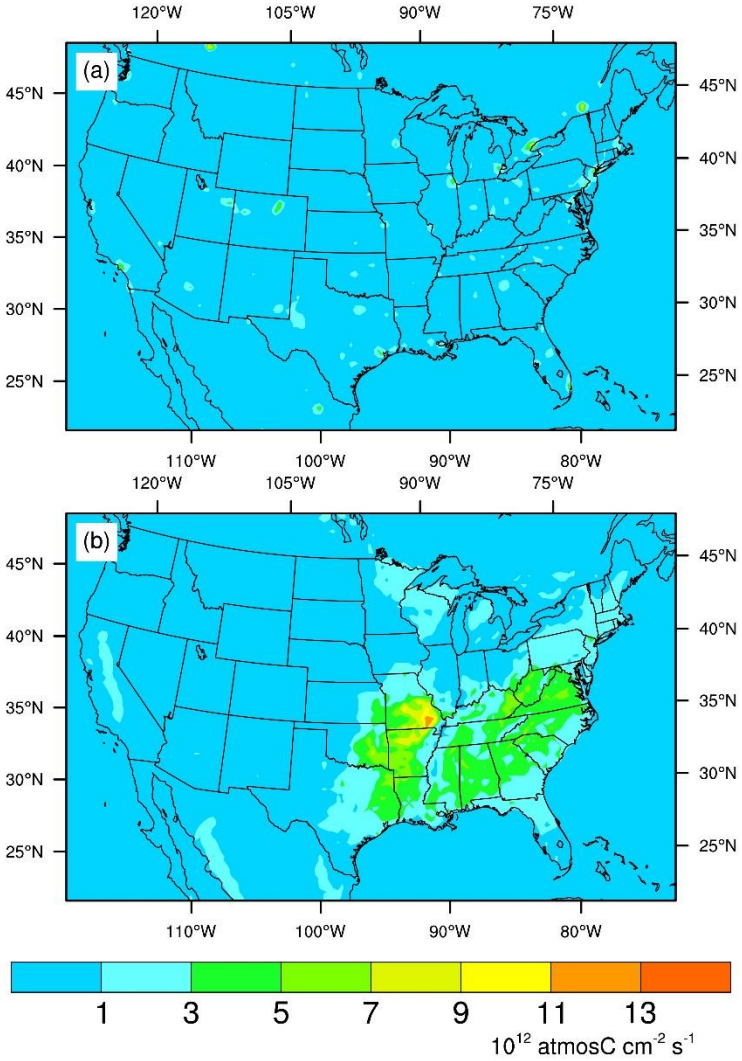

Figure 3. 7 Monthly averaged VOC emission distributions for July 2011: (a) anthropogenic VOC; (b) biogenic isoprene.

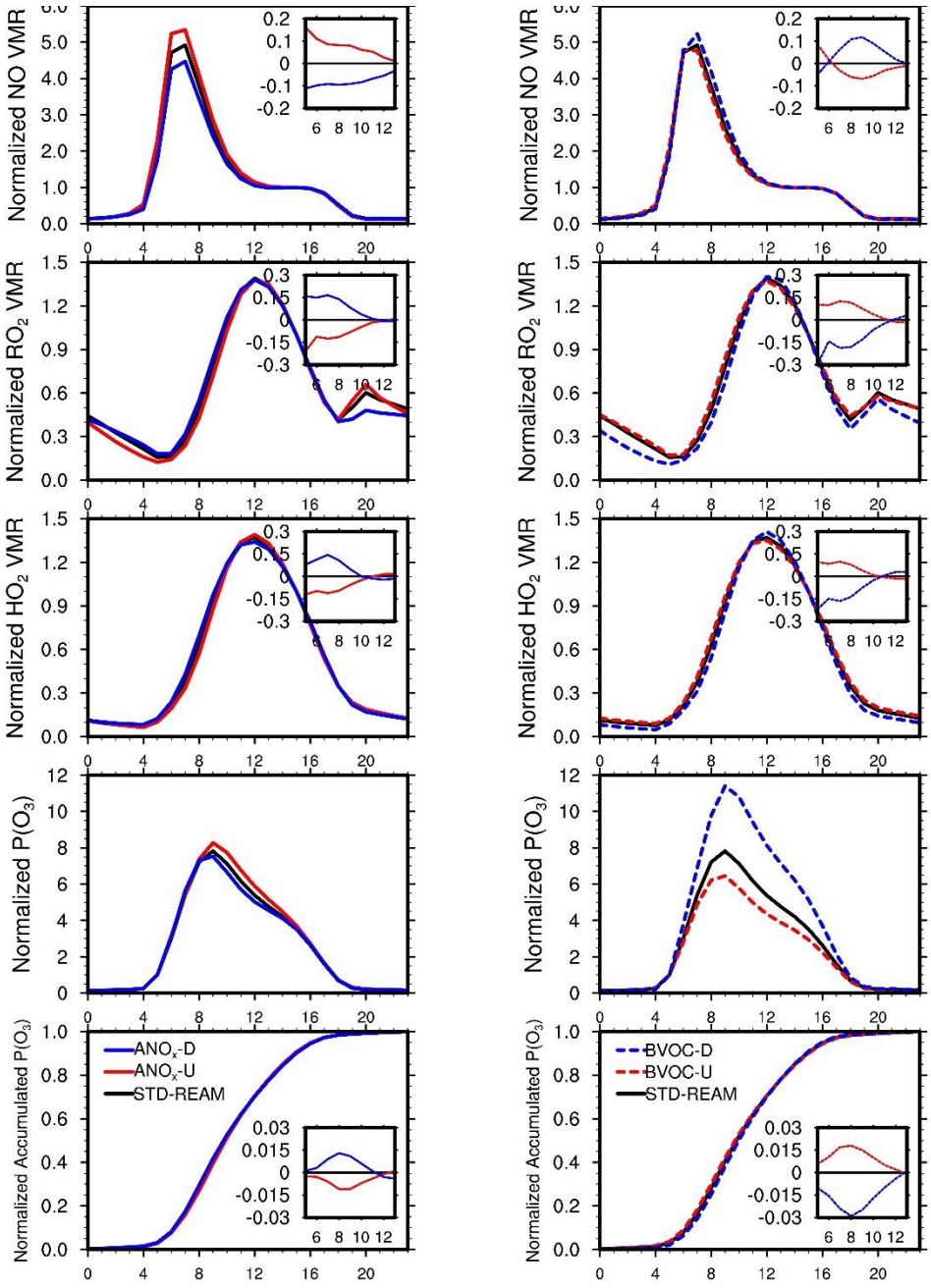

Figure 3. 8 The impacts of NO_x and BVOC emissions on diurnal cycles of NO, RO_2, and HO_2 concentrations and O_3 productions ($P(O_3)$), and on accumulated $P(O_3)$ in the Southeast for July 2011. The left panels are for NO_x emissions, and the right panels are for BVOC emissions. "STD-REAM", "ANO_x-D", "ANO_x-U", "BVOC-D", and "BVOC-U" are the same as Figure 3.2. RO_2 and HO_2 are scaled based on their reaction rates with NO. "Normalized NO VMR", "Normalized RO_2 VMR", and "Normalized HO_2 VMR" mean scaling concentrations of each hour to the corresponding 15:00 concentrations. "Normalized $P(O_3)$" denotes $P(O_3)$ scaled by the corresponding values at 5:00. The nested panels from "Normalized NO VMR", "Normalized RO_2 VMR", and "Normalized HO_2 VMR" are their relative differences between STD-REAM and the corresponding

sensitivity simulations. The nested panels from "Normalized Accumulated P(O_3)" are absolute differences between STD-REAM and the corresponding sensitivity simulations.

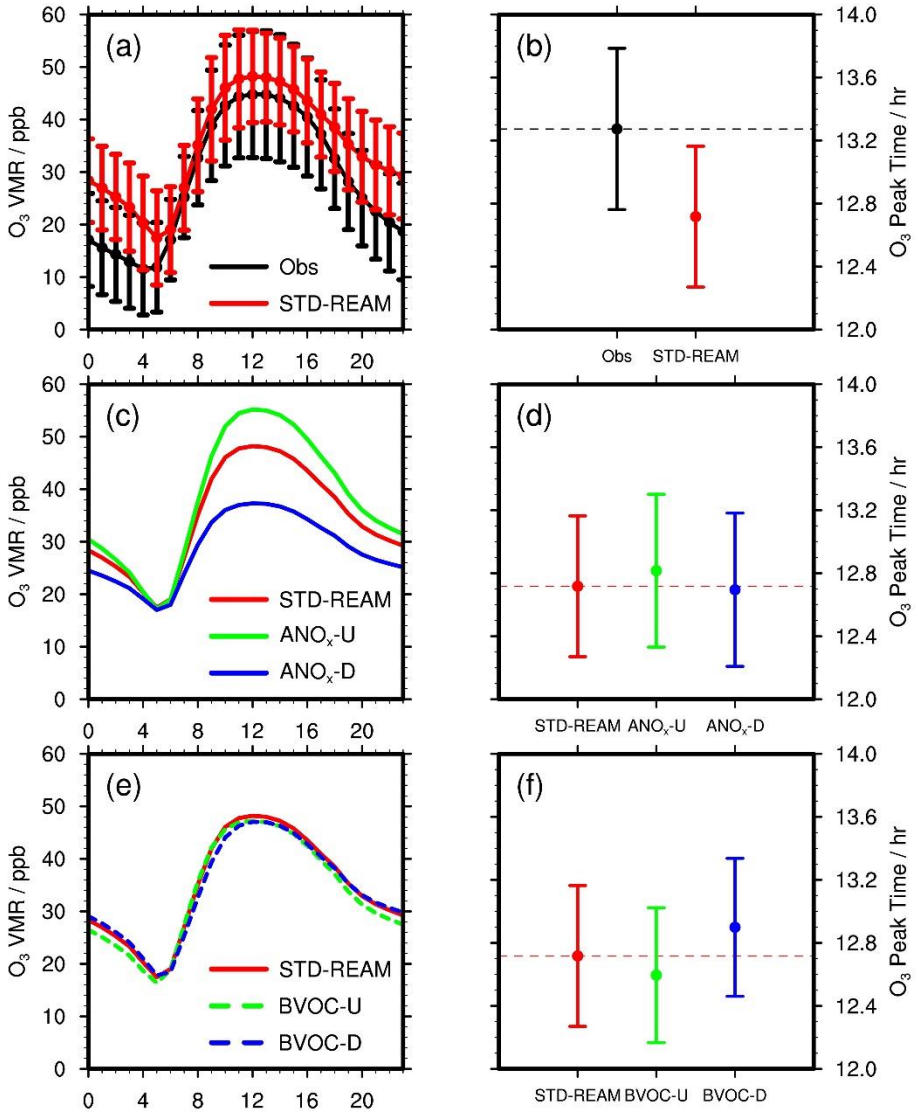

Figure 3. 9 Left panels: diurnal cycles of O_3 monthly mean concentrations in July 2011 for the observations and simulations with different emission scenarios in the Southeast. Right panels: the corresponding O_3 peak time, which is the same as Figures 3.2 and 3.5. "Obs" denotes EPA AQS surface observations, and "STD-REAM", "ANO_x-D", "ANO_x-U", "BVOC-D", and "BVOC-U" are the same as Figure 3.2. The standard deviations of observed and modeled O_3 concentrations are displayed as uncertainties in (a).

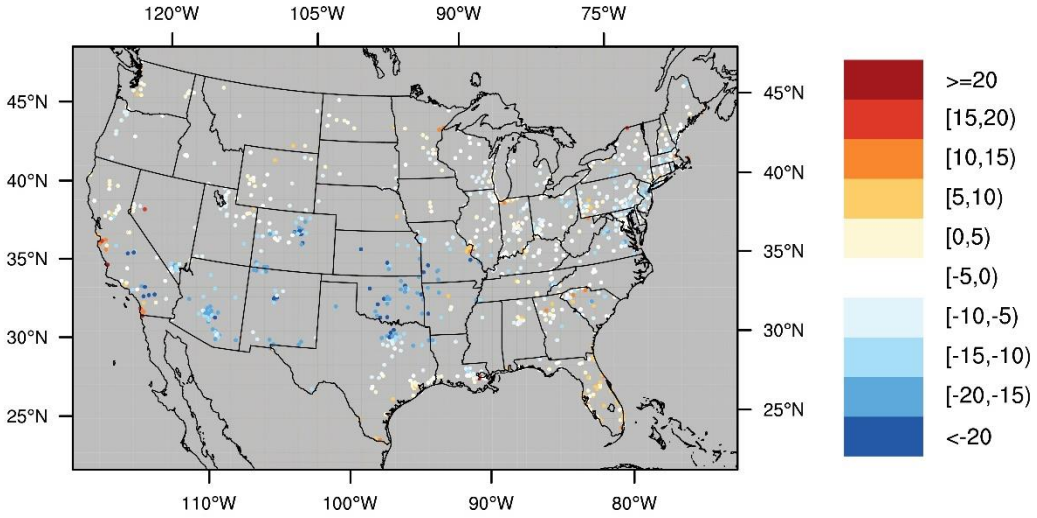

Figure 3. 10 Distribution of ozone peak value difference (ppbv) of the standard model result from the observations in July 2011.

CHAPTER 4. Inferring the anthropogenic NO_x emission trend over the United States after the Great Recession from satellite observations

4.1 Introduction

Anthropogenic emissions of nitrogen oxides ($NO_x = NO_2 + NO$) adversely affect the environment, not only because of their direct detrimental impacts on human health [*Greenberg et al.*, 2016; *Greenberg et al.*, 2017; *Heinrich et al.*, 2013; *Weinmayr et al.*, 2009], but also their fundamental roles in the formation of ozone, acid rain, and fine particles which are unfavorable to human health, ecosystem stabilities, and climate change [*Crouse et al.*, 2015; *Kampa and Castanas*, 2008; *Myhre et al.*, 2013; *Pandey et al.*, 2005; *Singh and Agrawal*, 2007]. About 48.8 Tg N yr-1 of NO_x are emitted globally from both anthropogenic (77%) and natural (23%) sources, such as fossil fuel combustion, biomass and biofuel burning, soil bacteria, and lightning [*Seinfeld and Pandis*, 2016]. 3.85 Tg N and 0.24 Tg N of anthropogenic and natural NO_x, respectively, were emitted from the U.S. in 2014 on the basis of the 2014 National Emission Inventory (NEI2014); vehicle sources and fuel combustions which accounted for 93% of the total anthropogenic NO_x emissions [*EPA*, 2017].

The U.S. NO_x emissions during the 2010s declined compared dramatically to the mid-2000s [*EPA*, 2018; *Xing et al.*, 2013] due to stricter air quality regulations and emission control technology improvements, such as the phase-in of Tire II vehicles during 2004 – 2009 and the switch of power plants from coal to natural gas [*De Gouw et al.*, 2014; *McDonald et al.*, 2018]. The overall reduction (about 30% - 50%) of NO_x

emissions from the mid-2000s to the 2010s was corroborated by observed decreasing of vehicle NO_x emission factors, NO_2 surface concentrations, nitrate wet deposition flux, and NO_2 tropospheric vertical column densities (TVCDs) [*Bishop and Stedman*, 2015; *J. Li et al.*, 2018; *McDonald et al.*, 2018; *Miyazaki et al.*, 2017; *Russell et al.*, 2012; *Tong et al.*, 2015]. However, the detailed NO_x emission changes after the Great Recession (from December 2007 to June 2009) are highly uncertain. On the one hand, the U.S. Environmental Protection Agency (EPA) estimated that the Great Recession had a slight impact on the NO_x emission trend, and the NO_x emissions decreased steadily from 2002 to 2017 (Figure 4.4), although the emission decrease rate slowed down by about 20% after 2010 (-5.8% yr-1 for 2002 – 2010, and -4.7% yr-1 for 2010 – 2017, Table 4.1) [*EPA*, 2018]. Fuel-based emission estimates in Los Angeles also showed a steady decrease of NO_x emissions after 2000 and a small impact of the Great Recession on NO_x emission decrease trend [*Hassler et al.*, 2016]. The continuous decrease of anthropogenic NO_x emissions was consistent with the ongoing reduction of vehicle emissions [*McDonald et al.*, 2018]. On the other hand, *Miyazaki et al.* [2017] and *Jiang et al.* [2018] found that the U.S. NO_x emissions derived from satellite NO_2 TVCDs, including OMI (the Ozone Monitoring Instrument), SCIAMACHY (SCanning Imaging Absorption SpectroMeter for Atmospheric CHartography), and GOME-2A (Global Ozone Monitoring Experiment – 2 onboard METOP-A), were almost flat from 2010 - 2015 and suggested that the decrease of NO_x emissions was only significant before 2010, which was completely different from the bottom-up and fuel-based emission estimates.

A complicating factor in inferring anthropogenic NO_x emission trends from the observations of NO_2 surface concentrations and satellite NO_2 TVCDs is the nonlinearity

in NO_x chemistry [*Gu et al.*, 2013; *Gu et al.*, 2016]. Although the decrease rates of both NO_2 surface concentrations and coincident OMI NO_2 TVCDs slowed down after the Great Recession over the United States, *Tong et al.* [2015], *Lamsal et al.* [2015] and *Jiang et al.* [2018] found that the decrease rates derived from NO_2 surface concentrations slowed down by 12% - 79% less compared to those from NO_2 TVCD (Table 4.1). Secondly, the decrease rates of NO_2 surface concentrations and OMI TVCD over cities and power plants [*Russell et al.*, 2012; *Tong et al.*, 2015] slowed down significantly less than those over the whole contiguous United States (CONUS) [*Jiang et al.*, 2018; *Lamsal et al.*, 2015]. Moreover, *R. Zhang et al.* [2018] found that filtering out lightning-affected measurements could significantly improve the comparison of NO_2 surface concentration and OMI NO_2 TVCD trends over the CONUS.

In this study, we carefully investigate the relationships among NO_x emissions, NO_2 surface concentrations, and NO_2 TVCDs over the CONUS and evaluate the impact of the relationships on inferring anthropogenic NO_x emission changes and trends from surface and satellite observations. Section 4.2 describes the model and datasets used in this study, including the Regional chEmistry and trAnsport Model (REAM), the EPA Air Quality System (AQS) NO_2 surface observations, and NO_2 TVCD products from OMI, GOME-2A, GOME-2B (GOME2 onboard METOP-B), and SCIAMACHY. In Section 4.3, we examine the nonlinear relationships among NO_x emissions, NO_2 surface concentrations, and NO_2 TVCDs using model simulations. Accounting for the effects of chemical nonlinearity, we then investigate the anthropogenic NO_x emission trends and changes from 2003 – 2017 over the CONUS. Finally, section 4.4 gives a summary of the study.

4.2 Model and Data Description

4.2.1 REAM

The REAM model has been applied and evaluated in many research applications including ozone simulation and forecast, emission inversion and evaluations, and mechanical studies of chemical and physical processes [*Alkuwari et al.*, 2013; *Cheng et al.*, 2017; *Cheng et al.*, 2018; *Y. Choi et al.*, 2008a; *Y. Choi et al.*, 2008b; *Gu et al.*, 2014; *Gu et al.*, 2013; *Koo et al.*, 2012; *Liu et al.*, 2014; *Liu et al.*, 2012b; *Yuhang Wang et al.*, 2007; *Q. Yang et al.*, 2011; *R. Zhang et al.*, 2017b; *R. Zhang et al.*, 2018; *Y. Zhang and Wang*, 2016; *C. Zhao and Wang*, 2009; *C. Zhao et al.*, 2009a; *C. Zhao et al.*, 2010]. REAM used in this work has 30 vertical layers in the troposphere, and the horizontal resolution is 36×36 km^2. The model is driven by meteorology fields from a Weather and Research Forecasting (WRF, version 3.6) model simulation initialized and constrained by the NCEP coupled forecast system model version 2 (CFSv2) products [*Saha et al.*, 2011]. The chemistry mechanism is based on GEOS-Chem v11.01 with updated reaction rates and aerosol uptake of isoprene nitrates [*Fisher et al.*, 2016]. Chemistry boundary conditions and initializations are from a GEOS-Chem ($2° \times 2.5°$) simulation. Hourly anthropogenic emissions on weekdays are based on the 2011 National Emission Inventory (NEI2011), while weekend anthropogenic emissions are set to be two-thirds of the weekday emissions [*Beirle et al.*, 2003; *Y. Choi et al.*, 2012]. Biogenic VOC emissions are estimated using the Model of Emissions of Gases and Aerosols from Nature (MEGAN) v2.10 [*Guenther et al.*, 2012]. NO_x emissions from soils are based on the Yienger and Levy (YL) scheme [*Yienger and Levy*, 1995].

4.2.2 Satellite NO_2 TVCDs

The satellite NO_2 TVCD products used in this study include GOME-2B (TM4NO2A v2.3), SCIAMACHY (QA4ECV v1.1), GOME-2A (QA4ECV v1.1), OMI (QA4ECV v1.1, hereafter referred to as OMI-KNMI), OMNO2 (SPv3, hereafter referred to as OMI-NASA), and the Berkeley High-Resolution NO_2 products (v3.0B, hereafter referred to as OMI-BEHR). We describe more detailed information and our pixel-size data selection criteria for these satellite products in the supplement and Tables 4.2, 4.3, and 4.4. After the selection, we re-grid the pixel-size data into the REAM 36 × 36 km^2 grid cells and calculate the seasonal means of each grid cell with corresponding daily values on weekdays (winter: January, February, and December; spring: March, April, and May; summer: June, July, and Autumn; autumn: September, October, and November). We excluded weekend data in this study to minimize the impacts of weekend NO_x emission reduction, leading to different NO_2 TVCDs between weekdays and weekends (Figure 4.5).

Satellite TVCD measurements can show large variations and apparent discontinuities due in part to the effects of cloud, lightning NO_x, the shift of satellite pixel coverage, and retrieval uncertainties (Figure 4.5; e.g., [*Boersma et al.*, 2018; *R. Zhang et al.*, 2018]). However, continuous and consistent measurements are required for reliable trend analyses. In addition to the criteria of data selection in Table 4.4, we compute the seasonal relative 90^{th} percentile confidence interval, defined as RCI = (X(95^{th} percentile) - X(5^{th} percentile)) / mean(X), where X is the daily NO_2 TVCD for a given season. To compute the seasonal trend, we require that RCI is < 50% for the selected season every year in the analysis period (Table 4.4). About 45% of data are removed as a result.

4.2.3 Surface NO_2 measurements

Hourly surface NO_2 measurements from 2003 - 2017 are from the EPA AQS monitoring network (archived on https://www.epa.gov/outdoor-air-quality-data). We discuss the uncertainties of different NO_2 measurement methods used in the AQS sites and our processing methods in the supplement. Since NO_2 surface concentrations have significant diurnal variations (Figure 4.7), we choose the data at 9:00-10:00 LT for comparison with GOME-2A/2B data, 10:00-11:00 LT for comparison with SCIAMACHY data, and 13:00-14:00 LT for OMI data. The resaonal *RCI* < 50% requirement is also used here to be consistent with the analysis of satelllite TVCD data. We also require that the measurement site must have valid measurements in the aforementioned 3 hours for at least one season from 2003 – 2017. The locations of the 179 selected sites using the site selection criteria are shown in Figure 4.8. The region definitions follow the U.S. Census Bureau (https://www2.census.gov/geo/pdfs/maps-data/maps/reference/us_regdiv.pdf).

4.3 Results and Discussions

4.3.1 Nonlinear relationships among NO_x emissions, NO_2 surface concentrations, and NO_2 TVCDs

NO_2 surface concentrations and NO_2 TVCD are not linearly correlated with NO_x emissions due in part to chemical nonlinearity [*Gu et al.*, 2013; *Lamsal et al.*, 2011]. Therefore, it is necessary to first investigate the nonlinearities among NO_x emissions, NO_2 surface concentrations, and TVCDs over the CONUS before we compare the trends between NO_2 surface concentrations and TVCDs. The nonlinearity between NO_x

emission and NO_2 TVCD is analyzed by examining the local sensitivity of NO_2 TVCD to NO_x emissions [*Gu et al.*, 2013; *Lamsal et al.*, 2011; *Tong et al.*, 2015], which is defined as β in Equation (4.1). We further define γ as the sensitivity of NO_2 surface concentration to NO_x emission:

$$\frac{\Delta E}{E} = \beta \frac{\Delta \Omega}{\Omega} \tag{4.1}$$

$$\frac{\Delta E}{E} = \gamma \frac{\Delta c}{c} \tag{4.2}$$

where E denotes NO_x emission and ΔE denotes the change of NO_x emission; Ω denotes NO_2 TVCD, c denotes surface NO_2 concentration, and $\Delta\Omega$ and Δc denote the corresponding changes.

We compute β and γ values for July 2011 using REAM; the method is described in the supplement. Figure 4.1 shows the distributions of our β and γ ratios as a function of NO_x emissions for July 2011 over the CONUS. While the model simulation is for one summer month, several key points on the surface and column concentration sensitivies to NO_x emissions have implications for comparing the trends of AQS and satellite TVCD data. (1) Both β and γ values are negatively correlated with NO_x emissions due to chemical nonlinearity and background NO_x contributions [*Gu et al.*, 2016; *Lamsal et al.*, 2011]. It is consistent with the distribution of β as a funciton of NO_x emissions in China [*Gu et al.*, 2013], although the β ratios for the US are generally larger than for China due primarily to different emission distributions of NO_x and VOCs and regional circulation patterns [*C. Zhao et al.*, 2009b]. (2) The uncertainties of β and γ values increase significantly as NO_x emissions decrease, which means regions with less NO_x emissions are more sensitive to environmental conditions, such as NO_x transport from nearby

regions. (3) The value of γ is generally less than β, especially for low-NO_x emission regions, which reflects the significant contribution of free tropospheric NO_2 to NO_2 TVCD but not to NO_2 surface concentrations. (4) The variations of β and γ values in NO_x emission bins tend to be larger at 10:00 – 11:00 than at 13:00 – 14:00 LT, reflecting a stronger effect due to weaker chemical loss at 10:00 – 11:00. (5) Both β and γ values are significantly less than 1 at 13:00 – 14:00 LT (β = 0.74 and γ = 0.84) when NO_x emissions are > 4×10^{12} molecules cm^{-2} s^{-1}, but they are close to 1 at 10:00 – 11:00 LT (β = 0.96 and γ = 1.02), which reflect stronger chemistry nonlinearity at 13:00 – 14:00 than in the morning.

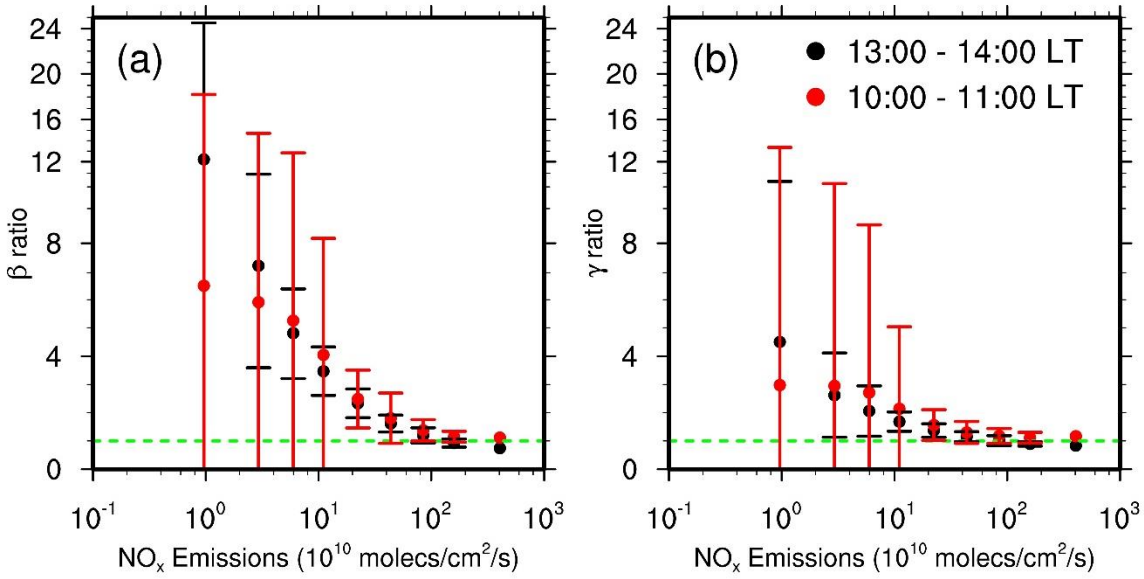

Figure 4. 1 Distributions of β (panel a) and γ (panel b) ratios as a function of NO_x emissions on weekdays for July 2011 over the CONUS. "13:00 – 14:00 LT" is for OMI, and "10:00 – 11:00" LT is for SCIAMACHY and GOME-2A/2B. The data are binned into nine groups based on NO_x emissions: $E \in (0, 2^1)$, $[2^1, 2^2)$, $[2^2, 2^3)$, $[2^3, 2^4)$, $[2^4, 2^5)$, $[2^5, 2^6)$, $[2^6, 2^7)$, $[2^7, 2^8)$, $[2^8, 2^9) \times 10^{10}$ molecules cm^{-2} s^{-1}. The green dashed line denotes a value of 1.

The largely varying β and γ values for NO_x emissions < 10^{11} molecules cm^{-2} s^{-1} imply that the trends derived from satellite TVCD data do not directly represent NO_x emissions. Therefore, the variations of TVCD data may not be comparable to the corresponding surface NO_2 concentrations. We define a region "urban", if anthropogenic NO_x emissions are > 10^{11} molecules cm^{-2} s^{-1}. All the other regions are defined as "rural". Figure 4.9 shows the distributions of anthropogenic NO_x emissions, and urban and rural regions defined in this study. Such defined urban regions account for 69.8% of the total anthropogenic NO_x emissions over the CONUS, the trend of which is therefore representative of anthropogenic emission changes (Table 4.5). A caveat is that some "urban" regions would become "rural" if anthropogenic NO_x emissions decreased after 2011 as the EPA NO_x emission trend suggested (Figure 4.4). In a sensitivity study, we define urban region using a stricter criterion of NO_x emissions > 2×10^{11} molecules cm^{-2} s^{-1} and the analysis results are similar to those shown in the next section.

4.3.2 Trend comparisons between NO_2 AQS surface concentrations and coincident satellite NO_2 tropospheric VCD over urban and rural regions

Using anthropogenic NO_x emissions of 10^{11} molecules cm^{-2} s^{-1} as the threshold value, 157 AQS sites are urban and the rest 22 sites are rural. Their properties are summarized in Table 4.5. Figure 4.2 shows the relative annual variations of AQS NO_2 surface measurements at 13:00 – 14:00 and coincident OMI-KNMI NO_2 TVCD data from 2005 – 2017 in each season for urban and rural regions. The contrast between the two regions is apparent in all seasons. For comparison purposes, we scale the time series of TVCD and AQS surface NO_2 to their corresponding 2005 values and the resulting data are therefore unitless. Over urban regions, NO_2 surface concentrations are highly

correlated with NO_2 TVCDs (TVCD = 1.03 × AQS + 0.11, R^2 = 0.98), reflecting the comparable and stable β and γ values (Table 4.5). However, over rural regions, the scaled TVCD data significantly deviate from AQS NO_2 data (TVCD = 1.15 × AQS + 0.09, R^2 = 0.87). It is noteworthy that the discrepancies between urban and rural data are smaller in winter than in spring, summer, and autumn due to a more dominant role of transport than chemistry and lower natural NO_x emissions in winter.

We also examine the correlations of AQS NO_2 surface concentrations with coincident OMI-NASA, OMI-BEHR, SCIAMACHY, GOME-2A, and GOME-2B TVCD measurements. The results of OMI-NASA and OMI-BEHR are similar to those of OMI-KNMI (Figure 4.2). SCIAMACHY and GOME-2B TVCD observations at 9:00-11:00 LT also show large contrast between urban (SCIAMACHY: TVCD = 0.92 × AQS - 0.005, R^2 = 0.94; GOME-2B: TVCD = 0.54 × AQS + 0.56, R^2 = 0.96) and rural regions (SCIAMACHY: TVCD = 0.77 × AQS +0.83, R^2 = 0.63; GOME-2B: TVCD = 0.46 × AQS + 0.73, R^2 = 0.59). The correlation of coincident GOME-2A NO_2 TVCD data with AQS surface concentrations is poor for rural (TVCD = 0.65 × AQS + 0.56, R^2 = 0.44) and urban (TVCD = 0.31 × AQS + 0.56, R^2 = 0.21) regions (Figure 4.10), which likely reflects the degradation of the GOME-2A instrument causing significant increase of NO_2 SCD uncertainties [*Boersma et al.*, 2018]. Therefore, we excluded GOME-2A in the analysis hereafter.

We further investigate the sensitivities of OMI-KNMI NO_2 TVCD relative annual variations from 2005 - 2017 to "urbanization levels" in Figure 4.11 over the CONUS. We find clear flattening of NO_2 TVCD variations as NO_x emissions decrease, which is

consistent with the above analyses. And like Figure 4.2, Figure 4.11 also show a less significant flattening effect in winter than the other three seasons due to the same reasons. Other satellite products also have similar flattening features, even for GOME-2A, but again, SCIAMACHY and GOME-2B show weaker impacts than OMI archives, consistent with above analyses. In summary, "urban" regions are much better than "rural" regions for satellite NO_2 TVCD interpreting anthropogenic NO_x emission variations.

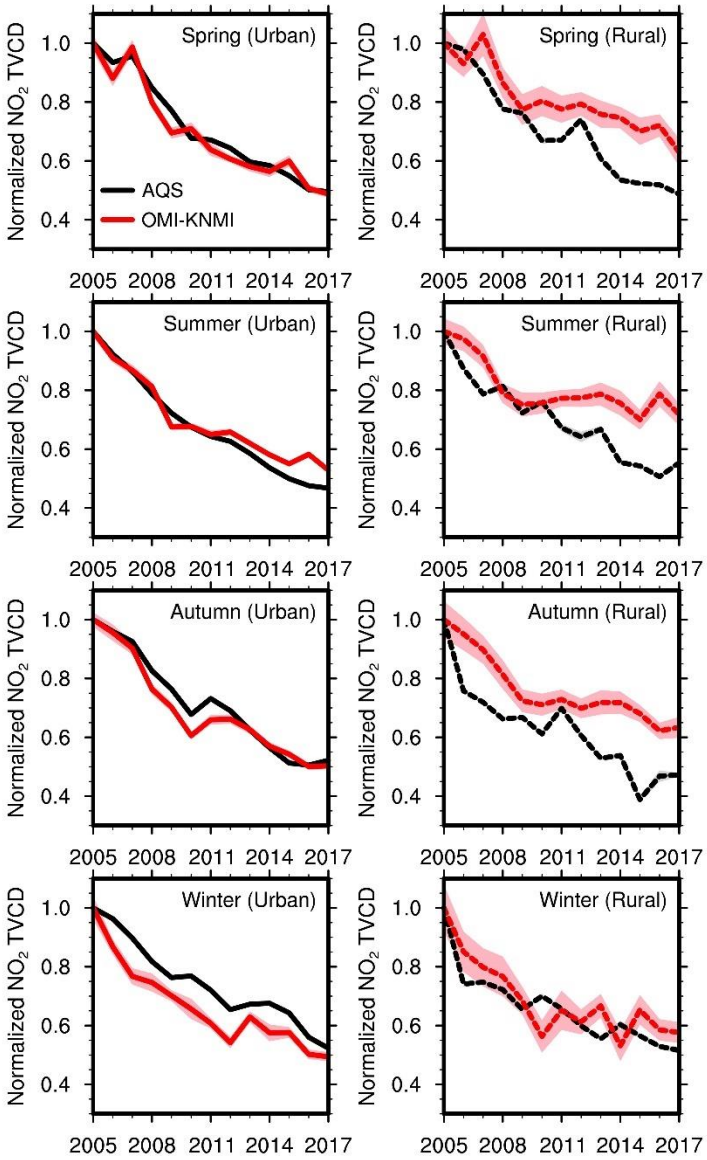

Figure 4. 2 Relative annual variations of AQS NO_2 surface concentrations and coincident OMI-KNMI NO_2 TVCD in each season from 2005 – 2017 for urban (left panel) and rural

(right panel) regions. The observation data are scaled by the corresponding 2005 values. Black and red lines denote AQS surface observations and OMI-KNMI NO_2 TVCDs, respectively. Shading in a lighter color is added to show the standard deviation of the results; when uncertainty is small due in part to the large number of data points, shading area may not show up.

4.3.3 Trend analysis of AQS NO_2 surface concentrations, satellite TVCDs, and updated EPA NO_x emissions

We first updated the CEMS measurement data used in the EPA NO_x emission trend datasets with the newest datasets obtained from https://ampd.epa.gov/ampd/. As shown in Figure 4.4, the updated CEMS data lead to a reduction of NO_x emissions during the Great Recession (2008 – 2009) and a recovery period in 2010 – 2011. The sharp drop during the Great Recession and the flattening trend right after the Great Recession are captured by OMI NO_2 and SCIAMACHY TVCD products (Figures 4.2, 4.3, and 4.12) and AQS NO_2 surface measurements (Figures 4.2, 4.3, and 4.7) and are also noted by *Russell et al.* [2012] and *Tong et al.* [2015] (Table 4.1).

In Figure 4.3, we show the comparisons among the relative variations of the updated EPA NO_x emissions, AQS NO_2 surface measurements at 10:00-11:00 and 13:00-14:00, and coincident satellite NO_2 TVCDs for urban regions in 4 seasons from 2003 to 2017. Figure 4.3 also shows the comparisons among the updated EPA NO_x emissions and satellite NO_2 TVCDs. There are many more data points for the latter comparison because the data selection is no longer limited to those coincident with the AQS surface data and therefore the uncertainty spread is much lower. The comparisons in general show consistent results that the updated EPA NO_x emissions, AQS surface measurements, and

satellite TVCD data are in agreement. The agreement of decreasing trends among the datasets are just as good for post-2011 period as pre-2011 period. This result differs from *Miyazaki et al.* [2017] and *Jiang et al.* [2018], who suggested no significant decreasing trend for OMI TVCD data after 2010. The disagreement can be explained by the results of Figure 4.11. Including the low NO_x emission regions leads to underestimates of NO_x decreases. Since the area of low NO_x emission regions is larger than high NO_x emission regions (Table 4.5), the arithmetic averaging will lead to a large weighting of rural observations, which do not reflect anthropogenic NO_x emission changes. *Miyazaki et al.* [2017] and *Jiang et al.* [2018] included all regions in their analyses, but we exclude rural regions. Figure 4.12 shows the seasonal variations if the TVCDs over rural regions are included; the result shows a much lower decreasing rate of TVCDs over the CONUS.

We summarize the decreasing rates of NO_2 after the Great Recession in Table 4.6. To minimize the effect of the sharp decrease and the following recovery, we chose to analyze the post-2011 period. Table 4.6 summarizes the results for each season, while Table 4.1 gives the averaged annual decreasing trends. Generally, Tables 4.1 and 4.6 confirm the continuous decreases of AQS surface observations, satellite NO_2 TVCD, and updated EPA NO_x emissions after 2011 as in Figure 4.3, but decreasing rates are lower than the pre-2011 period. Over the AQS urban sites, the slowdown magnitudes are 9% for AQS surface observations and 20% - 40% for satellite NO_2 TVCD measurements, which may reflect in part smaller γ than β values (Table 4.5). Our estimated slowdown magnitudes are significantly lower than *Lamsal et al.* [2015] and *Jiang et al.* [2018] but comparable to the results by *Tong et al.* [2015] (Table 4.1). The agreement with Tong et

al. (2015) is because we select urban AQS sites based on NO_x emissions and they chose eight large cities, while *Lamsal et al.* [2015] and *Jiang et al.* [2018] used all AQS sites.

Over the CONUS urban regions, updated EPA NO_x emissions show a slowdown of 22% compared to 29% - 46% for three OMI NO_2 TVCD products. The difference is partially due to the β ratio of 2.3 ± 0.9 at 13:00 – 14:00 over the CONUS urban regions (Table 4.5). Satellite NO_2 TVCD measurement uncertainties also contribute to the difference. From 2013 – 2017, GOME-2B NO_2 TVCDs decrease more than OMI products, especially in spring, autumn and winter (Tables 4.1 and 4.6). Finally, trend analyses in different regions (Table 4.7) indicate that generally, the Midwest has the least slowdown of the decreasing rate for urban OMI NO_2 TVCD (-14%) after 2011 compared to the Northeast (-30%), South (-34%), and West (-28%).

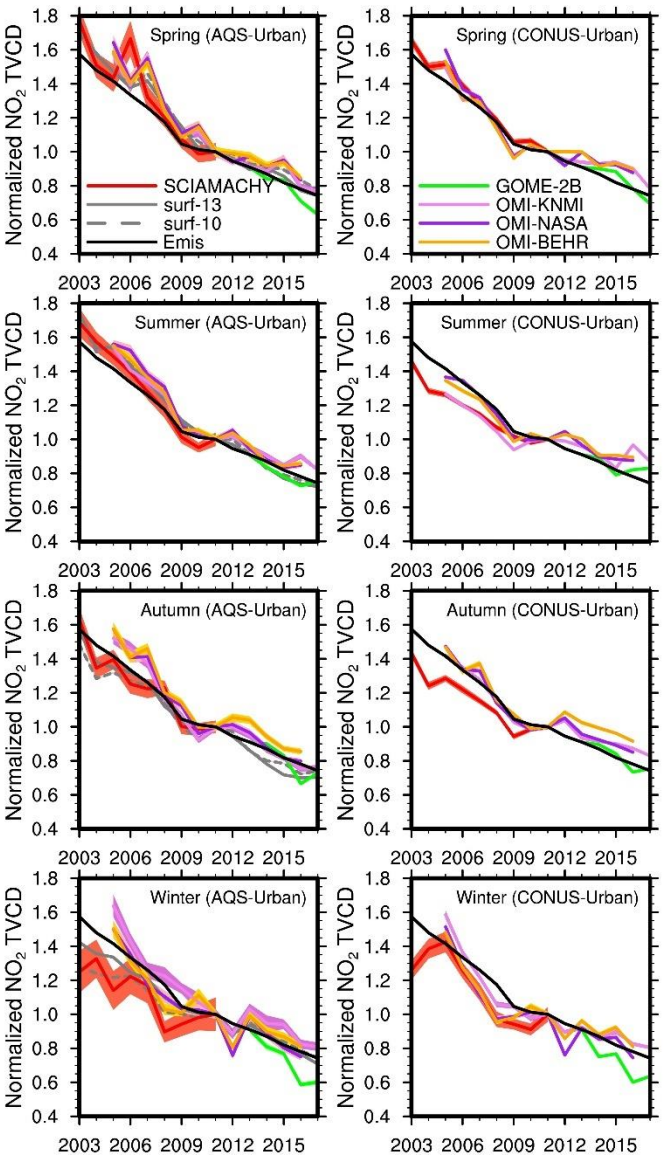

Figure 4. 3 Relative variations of AQS NO_2 surface measurements at 13:00-14:00 and 10:00-11:00 LT, updated EPA NO_x emissions, and satellite NO_2 TVCD data over the AQS urban sites (left column) and the CONUS urban regions (right column) for 4 seasons. AQS NO_2 surface measurements are not included in the right column. All datasets are scaled by their corresponding values in 2011 except for GOME-2B. For GOME-2B, we firstly normalized the values in each season to the corresponding 2013 values and plotted the relative changes from the 2013 EPA point of each season to make the GOME-2B relative variations comparable to the other datasets. Shading in a lighter color is added to show the standard deviation of the results; when uncertainty is small due in part to the large number of data points, shading area may not show up.

4.4 Conclusions

Using model simulations for July 2011, we demonstrate the nonlinear relationship of NO_2 surface concentration and TVCD with anthropogenic NO_x emissions. Over low NO_x emission regions, the ratios of NO_x emission changes to the changes of surface concentrations (γ) and TVCDs (β) have very large variations and $\beta > \gamma \gg 1$. Therefore, for the same emission changes, surface concentration and TVCD changes are much smaller and variable than urban regions, making it difficult to use the observations to directly infer anthropogenic NO_x emission trends. We find that defining urban regions where anthropogenic NO_x emissions are > 10^{11} molecules cm^{-2} s^{-1} and using surface and TVCD observations over these regions can infer the trends that can be compared with the EPA emission trend estimates.

We evaluate the anthropogenic NO_x emission variations from 2003 – 2017 over the CONUS by using satellite NO_2 TVCD products from GOME-2B, SCIAMACHY, OMI-KNMI, OMI-NASA, and OMI-BEHR, over the urban regions of CONUS. We find broad agreements among the decreases of AQS NO_2 surface observations, satellite NO_2 TVCD products, and the EPA NO_x emissions with the CEMS dataset updated. After 2011, they all show a slowdown of the decreasing rates. Over the AQS urban sites, NO_2 surface concentrations have a slowdown of 9% and OMI products show a slowdown of 20% - 40%. Over the CONUS urban regions, OMI TVCD products indicate a slowdown of 29% - 46%, and the updated EPA NO_x emissions have a slowdown of 22%. The different slowdown magnitudes between OMI TVCD products and the other two datasets may be caused by the nonlinear response of TVCD to anthropogenic emissions and the

uncertainties of satellite measurements (e.g., GOME-2B TVCD data show a larger decreasing trend than OMI products from 2013 – 2017).

We did not find observation evidence supporting the notion that anthropogenic NO_x emissions have not been decreasing after the Great Depression. In future studies, we recommend that the nonlinear relationships of NO_x emissions with NO_2 TVCD and surface concentration be carefully evaluated when applying satellite and surface measurements to infer the changes of anthropogenic NO_x emissions.

4.5 Supporting materials

4.5.1 Satellite NO_2 TVCD products and data selection criteria

In this study, we use NO_2 TVCD products from four satellite measurements in the past decade, including SCIAMACHY, GOME-2A, GOME-2B, and OMI, the spectrometers onboard sun-synchronous satellites to monitor atmospheric trace gases. The SCIAMACHY onboard the Environmental Satellite (ENVISAT) has an equator overpass time of 10:00 Local time (LT) and a nadir pixel resolution of 60 × 30 km^2. The GOME-2 instruments on Metop-A (named as GOME-2A) and Metop-B (GOME-2B) satellites cross the equator at 9:30 LT and have a nadir resolution of 80 × 40 km^2. After July 15, 2013, the nadir resolution of GOME-2A became 40 × 40 km^2 with a smaller scanning swath. The OMI onboard the EOS-Aura satellite has a nadir resolution of 24 × 13 km^2 and overpasses the equator around 13:45 LT. More detailed information about these instruments is summarized in Table 4.2. These instruments measure transmitted, backscattered, and reflected radiation from the atmosphere in ultraviolet and visible wavelength. The radiation measurements in wavelength of 402 - 465 nm are then used to

retrieve NO_2 VCDs. The retrieval process consists of three steps: 1) converting radiation observations to NO_2 slant column densities (SCDs) by using the Differential Optical Absorption Spectroscopy (DOAS) spectral fitting method; 2) separating tropospheric SCDs and stratospheric SCDs from the total NO_2 SCDs; 3) dividing the NO_2 tropospheric SCDs by the tropospheric air mass factors (AMF) to compute VCDs.

The product archives we use in this study include GOME-2B (TM4NO2A v2.3), SCIAMACHY (QA4ECV v1.1), GOME-2A (QA4ECV v1.1), OMI (QA4ECV v1.1, hereafter referred to as OMI-KNMI), OMNO2 (SPv3, hereafter referred to as OMI-NASA), and the Berkeley High-Resolution NO_2 products (v3.0B, hereafter referred to as OMI-BEHR). OMI-BEHR uses the tropospheric SCDs from OMI-NASA products but updates some inputs for the tropospheric AMF calculation [*Laughner et al.*, 2018]. These product archives have been previously validated [*Boersma et al.*, 2018; *Drosoglou et al.*, 2017; *Drosoglou et al.*, 2018; *Krotkov et al.*, 2017; *Laughner et al.*, 2018; *Yang Wang et al.*, 2017; *Zara et al.*, 2018]. Generally, the pixel-size uncertainties of these products are > 30% over polluted regions under clear-sky conditions. We summarize the basic information of these products in Table 4.3. To keep the high quality and sampling consistency of NO_2 TVCD datasets, we chose pixel-size NO_2 TVCD data using the criteria listed in Table 4.4.

4.5.2 AQS NO_2 measurement methods and uncertainties

Most AQS monitoring sites use the Federal Reference Method (FRM) — gas-phase chemiluminescence to measure NO_2. Few sites use the Federal Equivalent Method (FEM) – photolytic-chemiluminescence or the Cavity Attenuated Phase Shift Spectroscopy

(CAPS) method. FRM and FEM are indirect methods, in which NO_2 is first converted to NO and then NO is measured through chemiluminescence measurement of NO_2* produced by NO + O_3. The difference is that FRM uses heated reducers/catalysts for the conversion of NO_2 to NO and FEM uses photolysis of NO_2 to NO. The conversion to NO in the FRM instruments is not specific to NO_2, and non-NO_x active nitrogen compounds (NO_z) can also be reduced by the catalysts, which would cause high biases of NO_2 measurements, while the FEM method is sensible to the photolysis conversion efficiency of NO_2 to NO [*Beaver et al.*, 2013; *Beaver et al.*, 2012; *Lamsal et al.*, 2015]. The CAPS method directly determines NO_2 concentrations based on a NO_2-induced phase shift measured by a photodetector. The CAPS instrument operates at a wavelength of about 450 nm and may overestimate NO_2 concentrations due to absorption of other molecules at the same wavelength [*Beaver et al.*, 2013; *Beaver et al.*, 2012; *Kebabian et al.*, 2005].

Due to the different characteristics of the above three methods and demonstrated biases between the FRM and the FEM by *Lamsal et al.* [2015], we firstly investigate the measurement discrepancies among the above three methods. There are three sites having FRM and FEM measurements simultaneously during some periods from 2013 - 2014, two sites having both FRM and CAPS data during some periods from 2015 – 2016, and one site using all three measurement methods during some periods in 2015. Figure 4.6 shows the hourly averaged ratios of FEM and CAPS to FRM data, respectively, for 4 seasons during 2013 – 2016. The CAPS/FRM ratios are in the range of 0.94 – 1.06 and the FEM/FRM ratios of 0.86 – 1.11. Furthermore, *R. Zhang et al.* [2018] discussed that the relative trends are not affected by scaling the observation data. As in the work by *R.*

Zhang et al. [2018], we analyze the relative trends in the surface NO_2 data. We therefore did not scale the FRM data. At sites with FEM or CAPS measurements, we use these measurements in place of FRM data. If both FEM and CAPS data are available, we use the averages of the two datasets.

4.5.3 Model calculation of β and γ values

To compute local β and γ values over the CONUS, we added another independent group of chemistry species ("group 2") in REAM in order to compute the standard and sensitivity simulations concurrently. The original chemical species in the model ("group 1") were used in the standard simulation. For group 2 chemical species, anthropogenic NO_x emissions were reduced by 15%. In model simulation, we first compute the advection of group 1 tracers. The horizonal tracer fluxes were therefore available. All influxes into a grid cell for group 2 tracer simulation were from group 1 tracer simulation; only outfluxes were computed using group 2 tracers. The outflux was one way in that nitrogen species were transported out but the transport did not affect adjacent grid cells because the influxes were from group 1 tracer simulation. Using this procedure, the effects of NO_x emission reduction were localized. The β and γ values were computed by the ratio of TVCD and surface concentration changes to NO_x emission changes, respectively. The procedure used here is similar to *Gu et al.* [2013] and *Gu et al.* [2016]. Results essentially the same as Figure 4.1 were obtained when a perturbation of 10% was used for anthropogenic NO_x emissions.

4.5.4 Supporting Figures

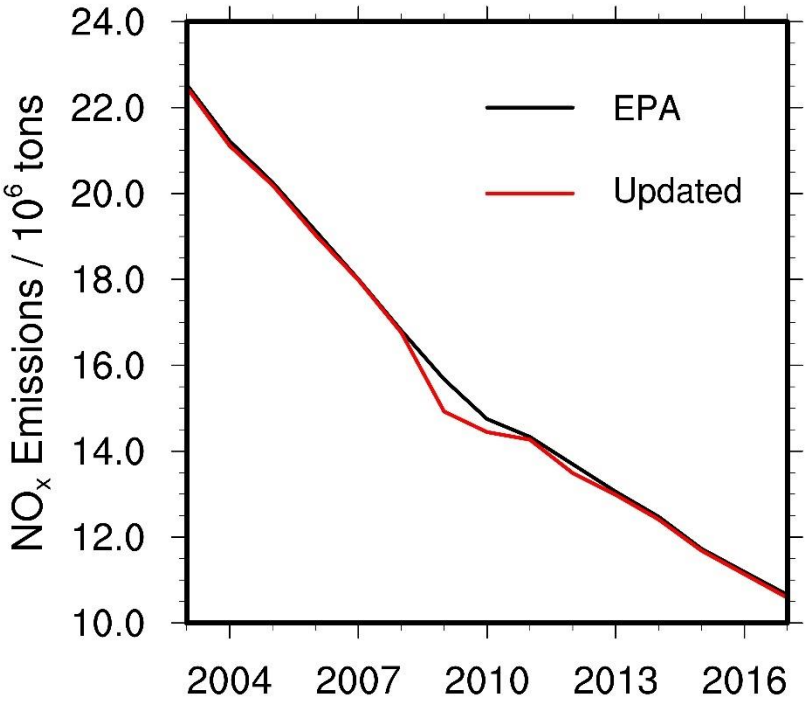

Figure 4. 4 Comparison between original EPA NO_x emissions and updated EPA NO_x emissions with the newest Continuous Emission Monitoring Systems (CEMS) measurements.

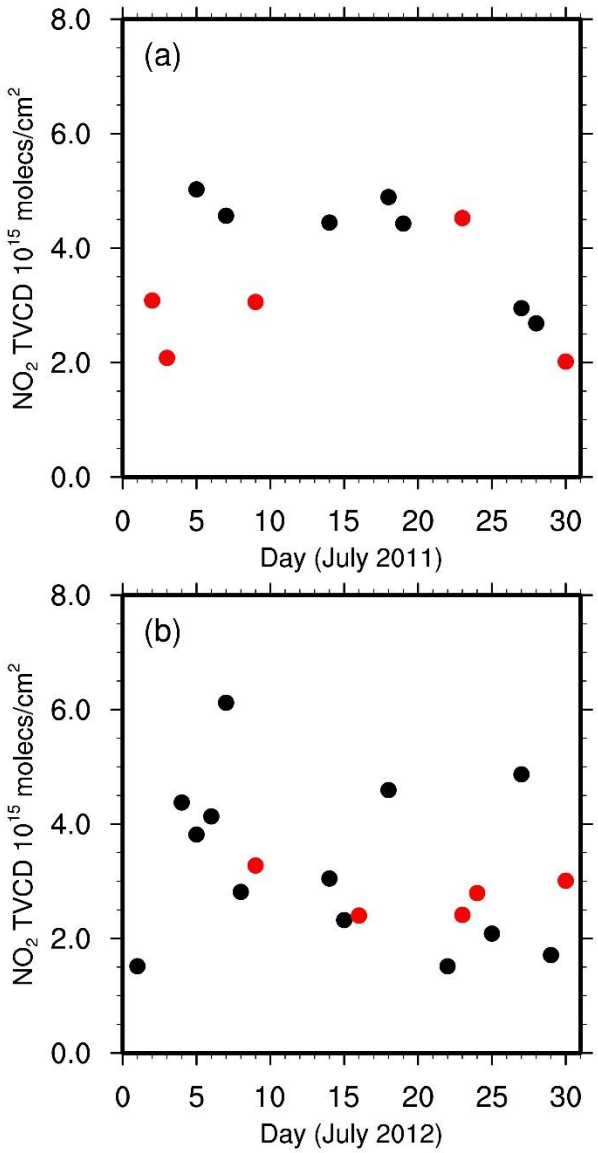

Figure 4. 5 Daily OMI NO_2 TVCDs for July 2011 (a) and 2012 (b) in Atlanta (33.755° N, 84.39° W). Black circles are weekday values, and red circles are weekend values. We find significant daily variations of NO_2 TVCD from (a) and (b). The number of available measurements in July 2011 are much less than July 2012. We find clear larger NO_2 TVCD values on weekdays than on weekends in July 2011, but the difference between weekday and weekday TVCDs in July 2012 are not so obvious.

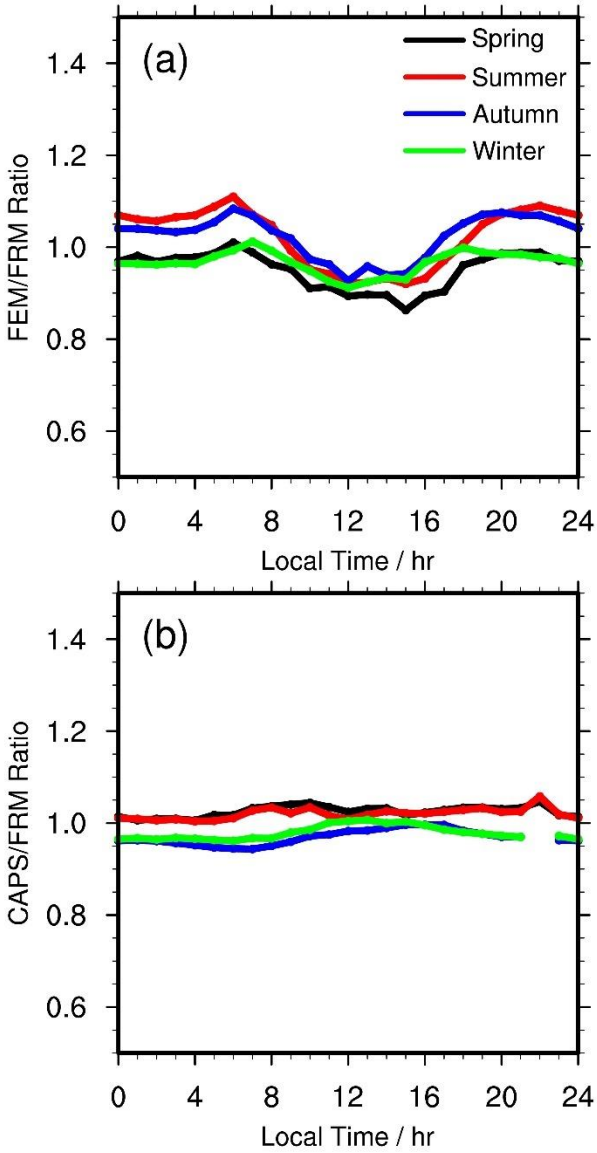

Figure 4. 6 Hourly averaged ratios of FEM (a) and CAPS (b) to FRM NO_2 measurements in each season, respectively. The FEM/FRM ratios are computed from coincident FRM and FEM measurements from 2013 – 2015 at 4 sites. The CAPS/FRM ratios are calculated based on coincident CAPS and FRM data from 2015 – 2016 at 3 sites.

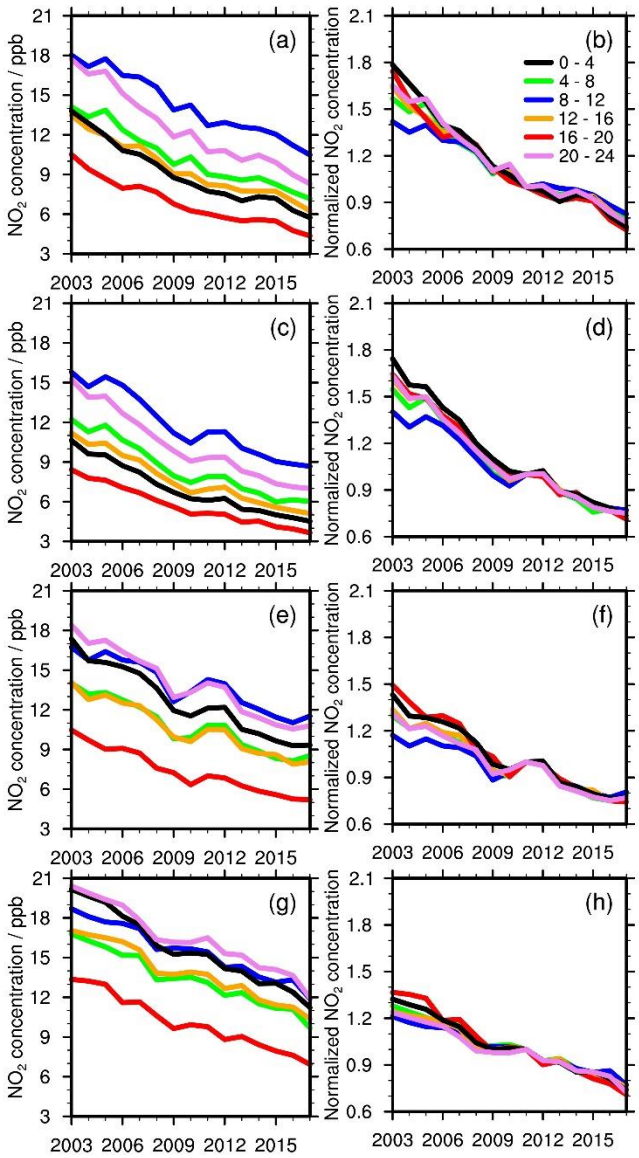

Figure 4. 7 Annual variations of AQS NO_2 surface concentrations at different hours on weekdays in spring (a, b), summer (c, d), autumn (e, f), and winter (g, h). Left panels show absolute NO_2 concentrations, and right panels are their relative variations normalized to 2011. To conduct reliable and consistent comparisons, we only used monitoring sites satisfying the seasonal *RCI* < 50% and continuity criteria on weekdays from 2003 – 2017.

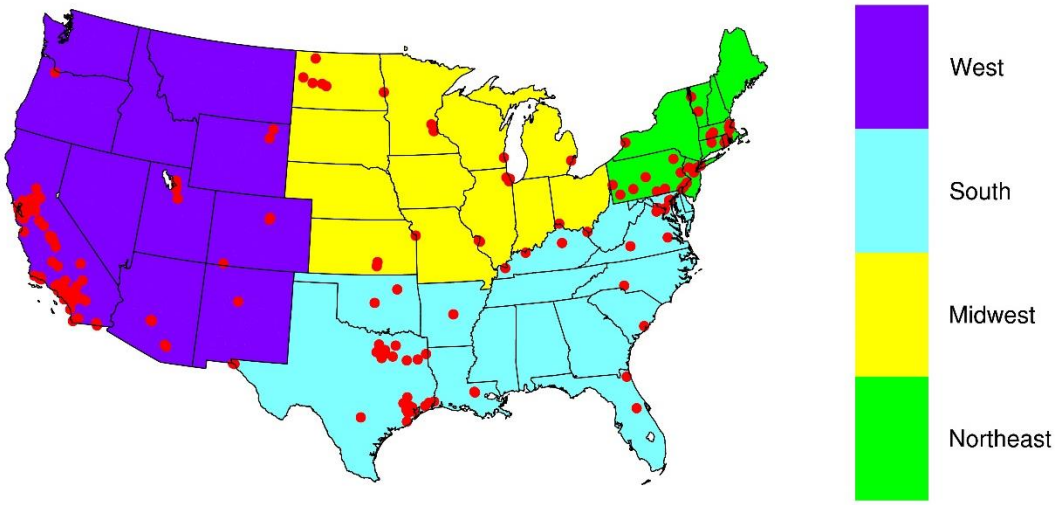

Figure 4. 8 Region definitions and locations of NO_2 surface observation sites used in this study.

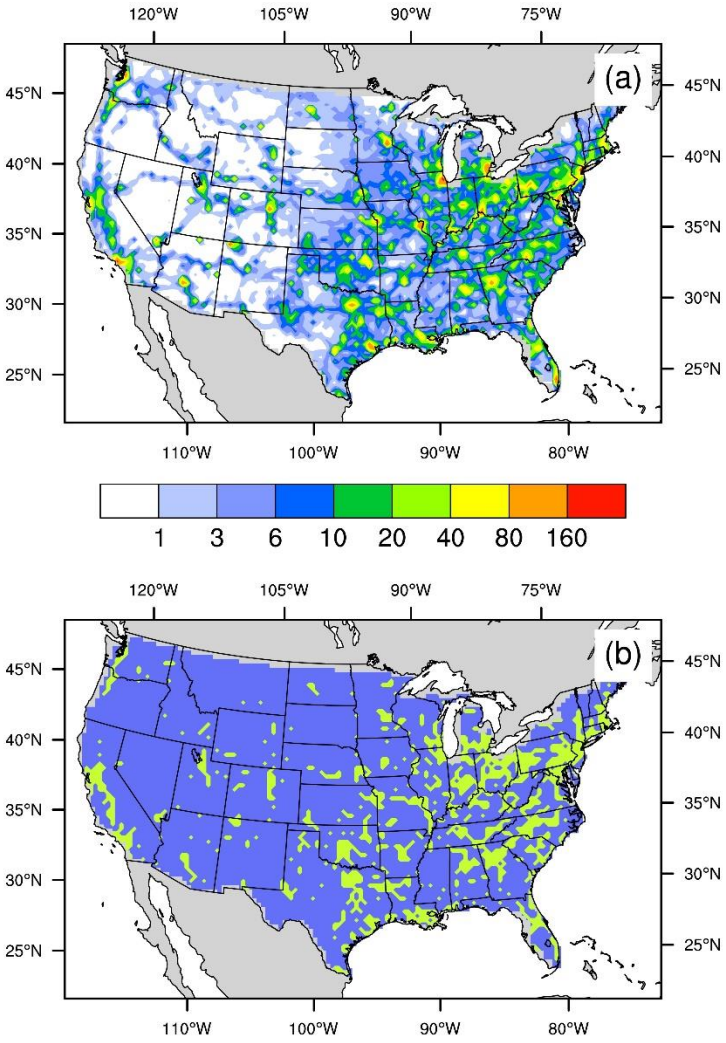

Figure 4. 9 Spatial distributions of (a) anthropogenic NO_x emissions (unit: 10^{10} molecules cm^{-2} s^{-1}) and (b) "urban" regions satisfying our selection criteria. In (b), Light green and blue denote the resulting urban and rural regions, respectively.

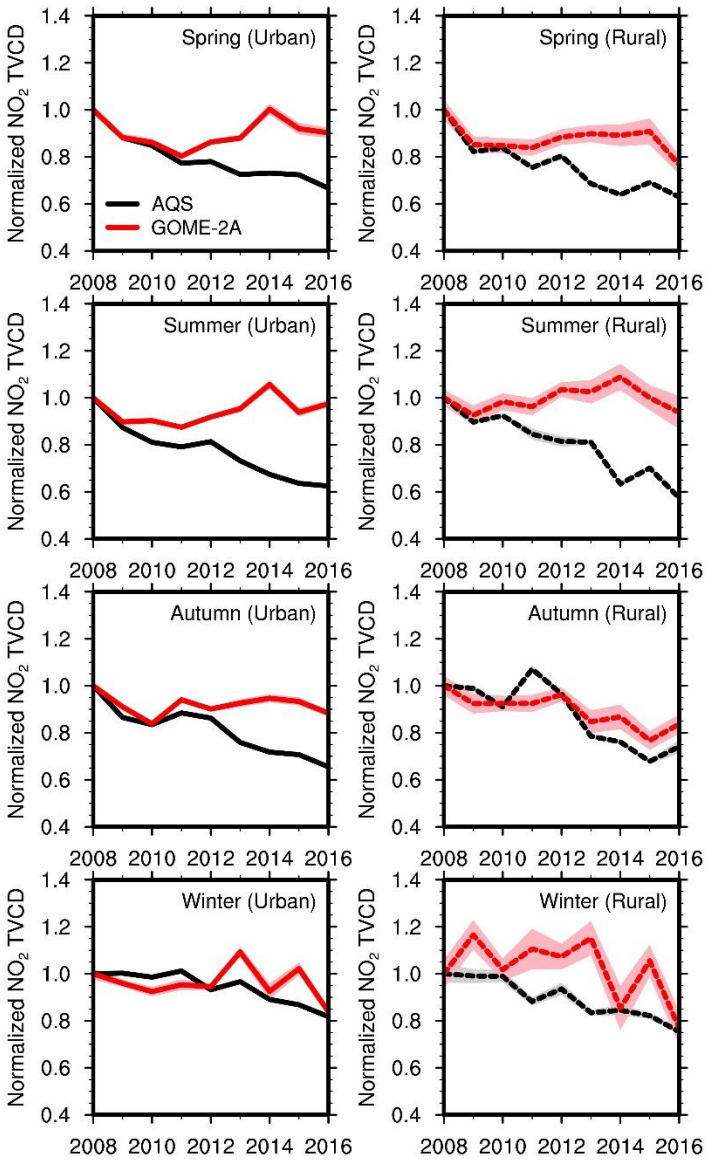

Figure 4. 10 Same as Figure 4.2, but for AQS NO_2 surface concentrations and coincident GOME-2A NO_2 TVCD data during 2008 – 2016.

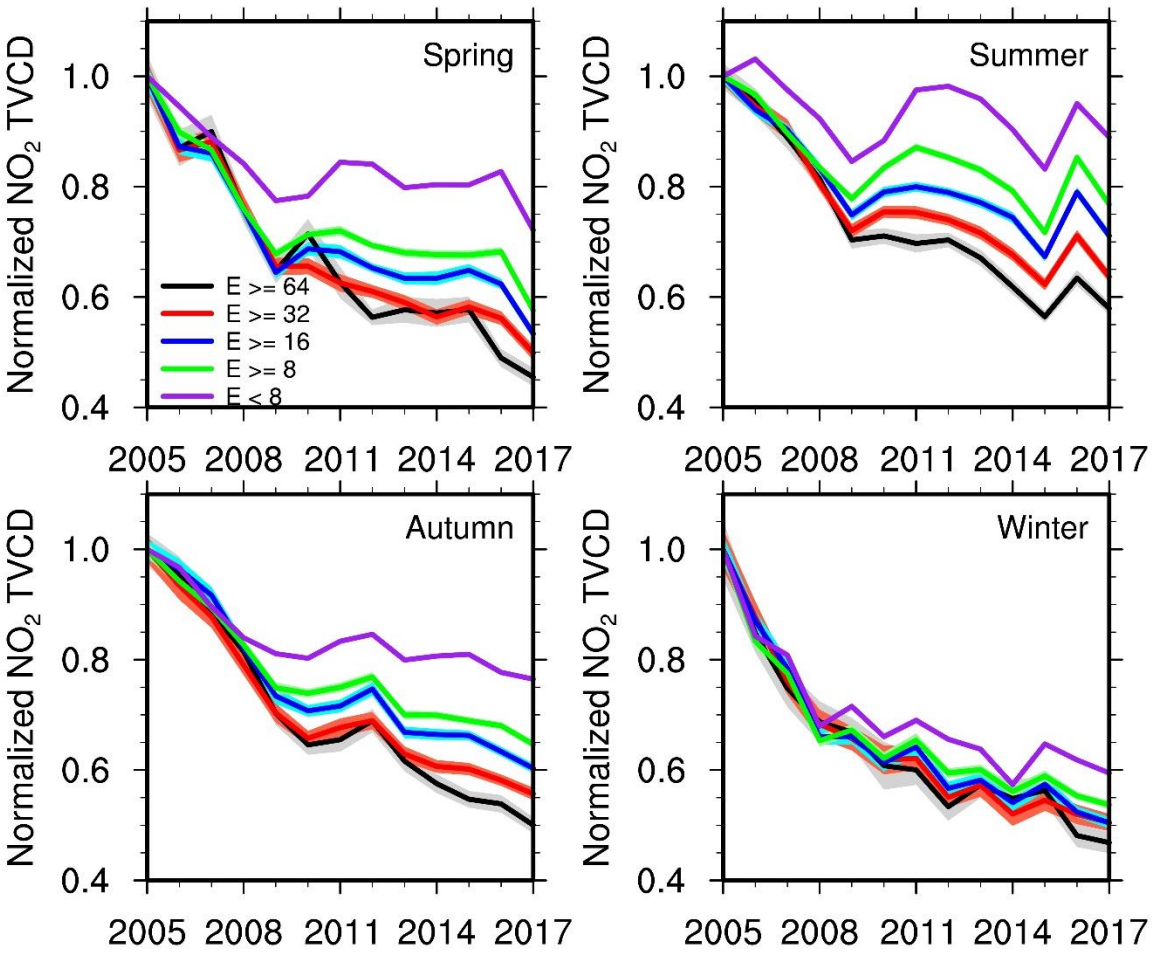

Figure 4. 11 Relative annual variations of OMI-KNMI NO_2 TVCD for different NO_x-emission groups in each season from 2005 - 2017. Group selection is based on anthropogenic NO_x emissions in July 2011. "E >= 64" indicates grids with NO_x emissions over 64×10^{10} molecules cm^{-2} s^{-1}. "E >= 32" denotes grids with NO_x emissions larger than 32×10^{10} molecules cm^{-2} s^{-1} but less than 64×10^{10} molecules cm^{-2} s^{-1}, etc. Shading in a lighter color is added to show the standard deviation of the results; when uncertainty is small due in part to the large number of data points, shading area may not show up.

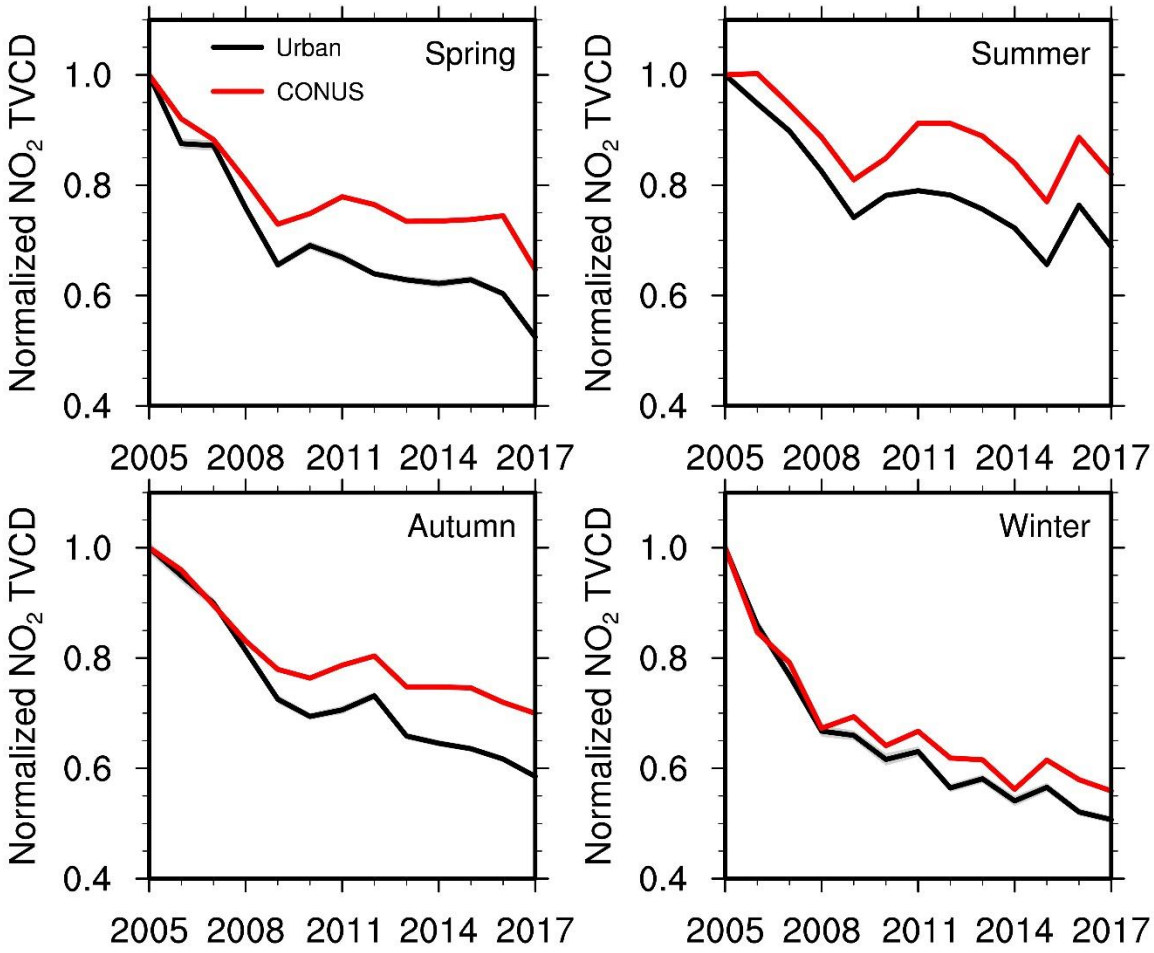

Figure 4. 12 Relative variations of OMI-KNMI NO_2 TVCD data for urban regions (black lines) and the whole CONUS (red lines) from 2005 – 2017 in 4 seasons.

4.5.5 Supporting tables

Table 4. 1 Summary of trends of satellite NO_2 TVCD products, NO_2 surface measurements, and EPA NO_x emissions during from different studies

Studies	Datasets	Period 1[1]		Period 2		Period 3		Slow down ratio[3]
		Time	Trend (yr^{-1})[2]	Time	Trend (yr^{-1})	Time	Trend (yr^{-1})	
This study for CONUS "urban" sites[4]	GOME-2B[5] (36 × 36 km^2)					2013 - 2017	**-8.2 ± 3.0%**	
	SCIAMACHY (36 × 36 km^2)	2003 – 2011	**-6.3 ± 1.1%**					
	OMI-NASA (36 × 36 km^2)	2005 – 2011	**-8.6 ± 1.2%**			2011 – 2016	**-6.1 ± 3.6%**	**-29%**[2]
	OMI-BEHR (36 × 36 km^2)	2005 – 2011	**-8.2 ± 1.3%**			2011 – 2016	**-4.4 ± 1.6%**	**-46%**
	OMI-KNMI (36 × 36 km^2)	2005 – 2011	**-7.7 ± 1.4%**			2011 - 2017	**-4.2 ± 0.5%**	**-46%**
	Updated EPA NO_x emissions[6]	2003 – 2011	**-6.5 ± 0.8%**			2011 - 2017	**-5.1 ± 0.3%**	**-22%**
This study for AQS "urban" sites	GOME-2B (36 × 36 km^2)					2013 - 2017	**-10.2 ± 2.9%**	
	SCIAMACHY (36 × 36 km^2)	2003 - 2011	**-7.6 ± 1.1%**					
	OMI-NASA (36 × 36 km^2)	2005 - 2011	**-9.0 ± 0.8%**			2011 – 2016	**-7.2 ± 3.8%**	**-20%**
	OMI-BEHR (36 × 36 km^2)	2005 - 2011	**-8.9 ± 0.3%**			2011 – 2016	**-6.2 ± 2.6%**	**-30%**
	OMI-KNMI (36 × 36 km^2)	2005 - 2011	**-9.0 ± 0.8%**			2011 - 2017	**-5.4 ± 0.9%**	**-40%**
	NO_2 surface VMR[7]	2003 - 2011	**-6.5 ± 1.2%**			2011 - 2017	**-5.9 ± 0.8%**	**-9%**
[*Russell et al.*, 2012][8]	BEHR v2.1 NO_2 TVCD (0.05°×0.05°)	2005 - 2007	-6 ± 5% **(-6.2%)**[9]	2007 - 2009	-8 ± 5% **(-8.4%)**	2009 - 2011	-3 ± 4% **(-3.0%)**	**-52%**

	Updated EPA NO_x emissions		**-6.0%**		**-10.0%**		**-2.4%**	**-60%**
[*Tong et al.*, 2015][10]	NASA v2.1 NO_2 TVCD (pixels < 50 × 24 km^2)	2005 - 2007	-7.3% **(-7.6%)**	2008 - 2009	-9.2% **(-11.4%)**	2010 - 2012	-2.8% **(-4.4%)**	**-42%**
	BEHR v2.1 NO_2 TVCD (pixels < 50 × 24 km^2)		-8.9% **(-9.3%)**		-9.1% **(-11.8%)**		-3.6% **(-6.0%)**	**-35%**
	NO_2 surface VMR		-6.0% **(-6.2%)**		-10.8% **(-13.2%)**		-3.4% **(-5.4%)**	**-13%**
	Updated EPA NO_x emissions		**-6.0%**		**-10.0%**		**-3.4%**	**-43%**
[*Lamsal et al.*, 2015][11]	NASA v2.1 NO_2 TVCD (0.1°×0.1°)	2005 - 2008	-4.8 ± 1.9% **(-5.1%)**			2010 - 2013	-1.2 ± 1.2% **(-1.2%)**	**-76%**
	NO_2 surface VMR		-3.7 ± 1.5% **(-3.8%)**				-2.1 ± 1.4% **(-2.1%)**	**-45%**
	Updated EPA NO_x emissions		**-6.4%**				**-4.0%**	**-38%**
[*Jiang et al.*, 2018][11]	NASA v3 NO_2 TVCD (0.5°×0.667°)	2005 - 2009	-10.2 ± 1.8% **(-9.8%)**			2011-2015	-3.2 ± 1.6% **(-3.2%)**	**-67%**
	KNMI v2 NO_2 TVCD (0.5°×0.667°)		-9.6 ± 1.7% **(-9.3%)**				-2.6 ± 1.8% **(-2.6%)**	**-72%**
	BEHR v2.1 NO_2 TVCD (0.5°×0.667°)		-8.5 ± 1.8% **(-8.2%)**				-2.1 ± 1.6% **(-2.1%)**	**-74%**
	NO_2 surface VMR		-6.6 ± 1.4% **(-6.4%)**				-2.6 ± 1.5% **(-2.6%)**	**-59%**
	Updated EPA NO_x emissions		**-7.8%**				**-5.0%**	**-36%**

[1] Since different studies used different time division methods, we list the time period of each study in the table.
[2] Trends are based on an exponential model ($E(y) = E_0 \times r^{y-y_0}$: "$y$" denotes year and "$y_0$" denotes the initial year; "$E(y)$" denotes the value at year "y" and "E_0" denotes the value at the initial year; r-1 is the relative trend).
[3] Slowdown ratios = Trend in "period 3" / Trend in "period 1" – 1.

[4] Trends in our study are calculated based on the national seasonal trends shown in Table 4.6.
[5] The information on satellite products used in this study is summarized in Table 4.3.
[6] We updated EPA NO_x emissions with the newest Continuous Emission Monitoring Systems (CEMS) datasets. Figure 4.4 shows the comparison between our updated and original EPA NO_x emissions [*EPA*, 2018].
[7] Denote the averaged trends of 13:00 and 10:00 LT based on the values in Table 4.6.
[8] The study used NO_2 TVCD from urban and power plant grid cells across the U.S.
[9] Since previous studies used linear models to calculate trends and the results are sensitive to their calculation methods and the selection of initial years, we recalculate the trends based on the above exponential model, which makes all the results consistent. Our results are those bold numbers inside the parentheses, while the numbers in normal fonts are from the original publications.
[10] The study uses NO_2 TVCD and surface concentrations from Los Angeles, Dallas, Houston, Atlanta, Philadelphia, Washington, D.C., New York, and Boston.
[11] The two studies used EPA Air Quality System (AQS) NO_2 surface measurements and coincident satellite NO_2 TVCD data over the U.S.

Table 4. 2 Summary of major satellite instruments for remote sensing of atmospheric NO_2 VCD in the past decade

Instrument	Satellite	Launch date	End date	Operator	Equator crossing time (local time)	UV/Vis Spectral range (nm)	Spectral resolution (nm)	Swath length (km)	Nadir pixel resolution (km × km)	Global coverage (days)
SCIAMACHY	ENVISAT[1]	03/01/2002[2]	04/08/2012[2]	ESA[3]	10:00[1]	240 – 805[4]	0.24 – 0.48[4]	960[5]	60 × 30[5]	6[5]
GOME-2A	MetOp-A[6]	10/19/2006[6]	in operation	EUMETSAT[7]	9:30[8]	240 – 790[8]	0.26 – 0.51[8]	1920 before Jul. 15th, 2013; 960 after Jul. 15th, 2013[8]	80 × 40 before Jul. 15th, 2013; 40 × 40 after Jul. 15th, 2013[8]	1.5[9]
GOME-2B	MetOp-B[6]	09/17/2012[6]	In operation	EUMETSAT	9:30[8]	240 – 790[8]	0.26 – 0.51[8]	1920[8]	80 × 40[8]	1.5[9]
OMI	EOS-Aura[10]	07/152004[10]	In operation	NASA	13:45[10]	270 – 500[11]	0.45 – 1.0[11]	2600[11]	24 × 13[11]	1[11]

[1] Refer to https://earth.esa.int/web/guest/missions/esa-operational-eo-missions/envisat
[2] Refer to https://en.wikipedia.org/wiki/Envisat
[3] The European Space Agency
[4] Refer to http://www.iup.uni-bremen.de/sciamachy/instrument/performance/index.html
[5] Refer to *Boersma et al.* [2008], *Boersma et al.* [2009], and [*Lee et al.*, 2009]
[6] Refer to https://www.eumetsat.int/website/home/Satellites/CurrentSatellites/Metop/index.html
[7] The European Organization for the Exploitation of Meteorological Satellites
[8] Refer to *EUMETSAT* [2015]
[9] Refer to *Lee et al.* [2009] and *Yang Wang et al.* [2017]
[10] Refer to https://aura.gsfc.nasa.gov/
[11] Refer to https://aura.gsfc.nasa.gov/omi.html

Table 4. 3 Summary of satellite NO_2 TVCD products and their retrieval information

NO_2 TVCD products	Version	Available period	DOAS fitting method	Stratosphere–troposphere separation	Fitting window (nm)	Albedo / reflectance	A priori profiles	Radiative transfer model	Cloud
GOME-2B	TM4NO2A (2.3)	12/20/2012 – current	Intensity fit[1]	Assimilation of satellite total slant columns in the TM4 model[2, 3]	405 – 465[1]	Climatology albedo from 3 years of OMI data[4]	TM4 (2° × 3°)[2]	DAK[2]	FRESCO+ (Oxygen A-band around 760 nm)[5]
SCIAMACHY	QA4ECV (v1.1)	08/02/2002 – 04/08/2012	Optical Density[1, 6]	Assimilation of OMI total slant columns in the TM5 - MP model[6, 7]	425 – 465[6]	Climatology albedo based on SCIAMACHY[8]	TM5-MP (1° × 1°)[6]	DAK	FRESCO+
GOME-2A	QA4ECV (v1.1)	02/01/2007 – 12/31/2016			405 – 465[1, 6]	Climatology albedo based on GOME-2A[8]			FRESCO+
OMI-KNMI	QA4ECV (v1.1)	10/012004 – Current			405 – 465[1, 6]	Climatology albedo from 5 years of OMI data[6]			Improved O_2-O_2 (477 nm)[9]
OMI-NASA	SPv3	01/01/2005 – 07/31/2017	Stepwise intensity fit with monthly averaged solar irradiance spectrum[1, 10]	Based on OMI total slant columns over regions with low estimated TVCD contributions (TVCD contributions less than 0.3×10^{15} molecules/cm^2)[10]	402 – 465[1, 10]	OMI climatology albedo[10]	GMI (1° × 1.25°)[10]	TMORAD[10]	O_2-O_2 (477 nm)[10, 11]
OMI-BEHR[13]	v3.0B	01/01/2005 – 07/31/2017				Based on MCD43D BRDF product (for land) and model parameterization (for ocean)	WRF-Chem (12 km)		

[1] Refer to *Zara et al.* [2018]
[2] Refer to *Boersma et al.* [2011]. "TM4" is the Tracer Model, version 4. "DAK" is the Doubling-Adding KNMI (DAK) radiative transfer model.
[3] Refer to *Williams et al.* [2009]
[4] Refer to *Kleipool et al.* [2008]
[5] Refer to *Yang Wang et al.* [2017] and *P. Wang et al.* [2008]
[6] Refer to *Boersma et al.* [2018]
[7] Refer to *Williams et al.* [2017]

[8] Refer to *Tilstra et al.* [2017]
[9] Refer to *Veefkind et al.* [2016]
[10] Refer to *Bucsela et al.* [2013], *Bucsela et al.* [2016], *Krotkov et al.* [2017], and *Marchenko et al.* [2015]. "TMORAD" is the TMOS radiative transfer model.
[11] Refer to *Acarreta et al.* [2004]
[12] Refer to *Lamsal et al.* [2014], *Oetjen et al.* [2013], and *Tong et al.* [2015]
[13] Refer to *Laughner et al.* [2018]. OMI-BEHR uses the SCD from OMI-NASA SPv3 but updates inputs for the AMF calculation, such as a prior NO_2 vertical profiles and surface reflectance. Besides, OMI-BEHR only provides NO_2 TVCD over the contiguous United States (CONUS). As in this study, we used the OMI-NASA datasets archived in the OMI-BEHR product, we only obtained OMI-NASA datasets extended to July 31, 2017.
[14] Average uncertainty over the CONUS is calculated based on the file from http://behr.cchem.berkeley.edu/behr/BEHR-us-uncertainty.hdf

Table 4. 4 Selection criteria for satellite NO2 TVCD pixel data

NO_2 TVCD products	Period	Solar zenith angle	albedo	Cloud radiance fraction	Snow or ice covered	AMFtrop/AMFgeo	Flag for retrieval success	Retrieval quality flag	Rows in swath
GOME-2B	01/01/2013 – 12/31/2017	< 80°	<= 0.3	<= 50%	No	> 0.2	Yes		All
SCIAMACHY	01/01/2003 – 12/31/2011	< 80°	<= 0.3	<= 50%	No	> 0.2	Yes		All
GOME-2A	01/01/2008 – 12/31/2016	< 80°	<= 0.3	<= 50%	No	> 0.2	Yes		All
OMI-KNMI[1]	01/01/2005 – 12/31/2017	< 80°	<= 0.3	<= 50%	No	> 0.2	Yes		6 - 21
OMI-NASA[1]	01/01/2005 – 12/31/2016	< 80°	<= 0.3	<= 50%			Yes	Yes	6 – 21
OMI-BEHR[1]	01/01/2005 – 12/31/2016	< 80°	<= 0.3	<= 50%			Yes	Yes	6 - 21

[1] Rows 6-21 are selected to remove the anomalies developed in the OMI sensor [*Boersma et al.*, 2018; *R. Zhang et al.*, 2018].

Table 4. 5 Properties of urban and rural regions in July 2011

type	Surface area fraction[1]	Anthropogenic NO_x emission fraction	Anthropogenic NO_x emissions ($\times 10^{10}$ molecules cm^{-2} s^{-1})	β at 13:00 – 14:00 LT	γ at 13:00 – 14:00 LT	β at 10:00 – 11:00 LT	γ at 10:00 – 11:00 LT
Urban/CONUS[2]	17.3%	69.8%	29.9	2.3 ± 0.9	1.4 ± 0.3	2.4 ± 1.8	1.5 ± 1.0
Rural/CONUS	82.7%	30.2%	2.7	8.1 ± 8.7	3.1 ± 3.9	5.9 ± 8.0	2.8 ± 5.8
Urban/AQS	87.7%		71.0	1.5 ± 0.7	1.2 ± 0.4	1.7 ± 1.0	1.3 ± 0.5
Rural/AQS	12.3%		5.7	5.0 ± 2.0	2.5 ± 1.3	4.3 ± 3.2	2.7 ± 2.6

[1] "Fraction" denotes the percentages of "urban" or "rural" data points for the whole CONUS or all AQS sites.
[2] "Urban-CONUS" denote CONUS "urban" grid cells; "Urban-AQS" denote AQS "urban" site grid cells.

Table 4. 6 Summary of national trends of updated EPA NO_x emissions, AQS NO_2 surface concentrations at 13:00 – 14:00 and 10:00 – 11:00 LT, and satellite NO_2 TVCD products for 4 seasons during different periods[1]

		Spring		Summer		Autumn		Winter	
		AQS site	CONUS	AQS site	CONUS	AQS site	CONUS	AQS site	CONUS
AQS NO_2 VMR at 13:00 -14:00	2003 – 2011	-7.3 ± 1.4%		-7.4 ± 0.9%		-6.7 ± 1.8%		-5.2 ± 0.8%	
	2011 – 2017	-5.3 ± 1.6%		-6.4 ± 1.2%		-7.3 ± 2.5%		-6.0 ± 2.8%	
AQS NO_2 VMR at 10:00 – 11:00	2003 – 2011	-7.1 ± 1.6%		-7.6 ± 1.5%		-6.2 ± 2.2%		-4.4 ± 1.6%	
	2011 – 2017	-4.4 ± 1.4%		-6.1 ± 1.8%		-6.3 ± 2.5%		-5.2 ± 2.4%	
SCIAMACHY	2003 – 2011	-8.8 ± 3.4%	-6.9 ± 1.1%	-8.2 ± 1.6%	-5.2 ± 1.2%	-6.8 ± 2.4%	-5.6 ± 2.1%	-6.4 ± 7.4%	-7.5 ± 5.5%
	2011 – 2017								
GOME2B	2003 – 2011								
	2013 – 2017	-10.2 ± 7.8%	-8.3 ± 16.9%	-6.4 ± 14.0%	-5.3 ± 4.0%	-10.5 ± 41.6%	-6.9 ± 13.2%	-13.6 ± 15.1%	-12.3 ± 78.9%
OMI-KNMI	2005 – 2011	-9.3 ± 5.6%	-8.3 ± 4.6%	-8.3 ± 2.4%	-5.9 ± 5.2%	-10.0 ± 4.2%	-7.4 ± 2.4%	-8.3 ± 2.1%	-9.3 ± 5.2%
	2011 – 2017	-5.3 ± 6.0%	-4.3 ± 6.5%	-4.2 ± 3.0%	-4.9 ± 9.2%	-6.0 ± 1.8%	-3.8 ± 1.8%	-6.1 ± 25.6%	-3.8 ± 3.5%
OMI-NASA	2005 – 2011	-9.4 ± 5.0%	-9.6 ± 5.3%	-9.4 ± 2.8%	-7.1 ± 2.9%	-9.4 ± 3.2%	-8.1 ± 2.8%	-7.8 ± 3.6%	-9.5 ± 16.6%
	2011 – 2016	-4.4 ± 18.9%	-3.8 ± 7.5%	-5.7 ± 6.7%	-4.5 ± 5.3%	-6.0 ± 3.1%	-4.6 ± 3.9%	-12.8 ± 7.8%	-11.4 ± 6.6%
OMI-BEHR	2005 – 2011	-9.1 ± 5.3%	-8.9 ± 5.8%	-8.7 ± 2.4%	-6.4 ± 3.2%	-9.2 ± 3.2%	-8.0 ± 3.1%	-8.5 ± 10.6%	-9.4 ± 23.0%
	2011 – 2016	-3.8 ± 4.4%	-3.0 ± 4.0%	-5.4 ± 7.0%	-3.9 ± 6.6%	-5.6 ± 13.2%	-4.1 ± 14.0%	-9.9 ± 5.2%	-6.7 ± 5.9%
EPA	2003 – 2011	-6.5 ± 0.8%							
	2011 – 2017	-5.1 ± 0.3%							

[1] We calculate trends by using the exponential model described in Table 4.1.

Table 4. 7 Summary of annual trends of AQS NO_2 surface concentrations and satellite NO_2 TVCD products in each region during different periods[1]

		Northeast AQS site	CONUS	Midwest AQS site	CONUS	South AQS site	CONUS	West AQS site	CONUS
AQS NO_2 VMR at 13:00 -14:00	2003 – 2011	-6.8 ± 0.7%		-6.1 ± 1.2%		-6.6 ± 0.7%		-7.6 ± 1.2%	
	2011 – 2017	-8.0 ± 1.2%		-6.4 ± 0.8%		-5.8 ± 0.6%		-7.2 ± 1.6%	
AQS NO_2 VMR at 10:00 – 11:00	2003 – 2011	-6.6 ± 0.5%		-5.8 ± 1.5%		-6.5 ± 1.3%		-7.1 ± 1.6%	
	2011 – 2017	-7.6 ± 1.0%		-6.8 ± 0.5%		-5.7 ± 0.1%		-6.1 ± 1.1%	
SCIAMACHY	2003 – 2011 2011 – 2017	-17.1 ± 2.7%	-11.0 ± 3.3%	-12.9 ± 6.8%	-6.5 ± 0.8%	-9.1 ± 1.0%	-6.2 ± 1.5%	-9.1 ± 1.8%	-7.0 ± 1.4%
GOME2B	2003 – 2011 2013 – 2017	-11.4 ± 3.7%	-10.8 ± 3.9%	-9.9 ± 13.1%	-4.4 ± 27.2%	-8.9 ± 3.0%	-7.5 ± 3.6%	-11.8 ± 3.0%	-10.6 ± 2.3%
OMI-KNMI	2005 – 2011	-14.2 ± 6.3%	-10.6 ± 3.8%	-9.2 ± 4.2%	-8.4 ± 2.8%	-9.2 ± 2.7%	-8.2 ± 1.5%	-10.5 ± 1.6%	-8.7 ± 0.9%
	2011 – 2017	-18.0 ± 16.2%	-7.6 ± 4.2%	-7.6 ± 3.3%	-7.0 ± 1.7%	-4.8 ± 1.4%	-4.6 ± 1.0%	-6.4 ± 1.4%	-4.8 ± 1.2%
OMI-NASA	2005 – 2011	-11.8 ± 1.3%	-11.0 ± 1.8%	-10.9 ± 4.8%	-10.0 ± 4.1%	-10.0 ± 3.5%	-9.5 ± 1.9%	-10.2 ± 1.8%	-8.5 ± 0.9%
	2011 – 2016	-10.0 ± 4.9%	-8.5 ± 3.8%	-13.2 ± 3.2%	-9.2 ± 2.7%	0.3 ± 19.2%	-8.0 ± 5.5%	-9.0 ± 5.7%	-6.6 ± 3.9%
OMI-BEHR	2005 – 2011	-11.8 ± 1.8%	-10.9 ± 1.9%	-12.2 ± 7.3%	-9.8 ± 4.4%	-9.5 ± 3.1%	-8.8 ± 2.0%	-9.9 ± 1.1%	-8.2 ± 0.4%
	2011 – 2016	-8.2 ± 3.4%	-6.6 ± 1.7%	-27.4 ± 24.3%	-8.1 ± 3.0%	-7.2 ± 2.3%	-5.0 ± 1.3%	-13.2 ± 14.5%	-7.0 ± 4.8%

Annual trends are the averages of regional seasonal trends.

CHAPTER 5. The underestimated impact of thunderstorms on surface ozone over the United States

5.1 Introduction

Thunderstorms (deep convection) play a crucial role in tropospheric chemistry and climate due to their direct emissions of lightning nitrogen oxides ($NO_x = NO + NO_2$), their key impact on pollutant re-distributions in the atmosphere, and the effect of cumulus clouds on solar radiance balance. Lightning NO_x, with annual global emissions of 2 – 8 Tg N [*Huntrieser et al.*, 2002; *Miyazaki et al.*, 2014; *Schumann and Huntrieser*, 2007; *Seinfeld and Pandis*, 2016], is the primary source of upper tropospheric NO_x [*S. Choi et al.*, 2014], which contributed to 60% - 75% of summertime 300 hPa NO_x over the eastern United States during 2004 – 2006 [*Allen et al.*, 2010; *C. Zhao et al.*, 2009a] and about 40% of total reactive odd nitrogen (NO_y) in the northern midlatitude (30°N) upper troposphere (500 hPa – 200 hPa) from 1990 – 1999 [*Grewe*, 2007]. As a precursor of ozone production, lightning NO_x contributed to about 25% of O_3 in the northern midlatitude upper troposphere [*Grewe*, 2007] and 19% - 31% (15 – 24 ppbv) of upper tropospheric O_3 over the eastern United States in the summers of 2004 – 2006 [*Allen et al.*, 2010; *Allen et al.*, 2012; *L. Wang et al.*, 2013; *C. Zhao et al.*, 2009a]. Due to the longer lifetime of upper tropospheric NO_x up to 10 days compared to a few hours in the boundary layer [*Jaegle et al.*, 1998], lightning NO_x can affect regions downwind far away from the lightning source region. For example, lightning in northern Kentucky and southern Ohio on July 27, 2011, even significantly evaluated the upper tropospheric NO_x and O_3 concentrations at downwind Huntsville,

Alabama (about 300 km from the lightning sources) after 16 hours of the lightning occurrence [*L. Wang et al.*, 2015].

Updrafts and downdrafts from thunderstorms are important factors redistributing air pollutants in the troposphere. On the one hand, pollutants and ozone precursors in the boundary layer, such as NO_x, VOC and CO, can be transported to upper troposphere by convective updrafts [*Dickerson et al.*, 1987; *Huntrieser et al.*, 2002], which further improves O_3 production in the upper troposphere with elevated formation of peroxy radicals [*Barth et al.*, 2016; *Barth et al.*, 2012]. On the other hand, convective downdrafts transport air with lightning NO_x and high-O_3 concentrations in the upper troposphere to the lower troposphere [*Luo et al.*, 2017; *Ott et al.*, 2010], which may affect surface NO_x and O_3 concentrations [*Allen et al.*, 2012; *Bharali et al.*, 2015; *Kar and Liou*, 2014]. However, due to the significant contributions of surface sources to surface NO_x and O_3 concentrations and the impact of thunderstorms on cloud optical depth and precipitations which affect the soil NO_x emissions and photochemistry activity in the boundary layer, the effect of thunderstorms on surface NO_x and O_3 is smaller compared to the upper troposphere. Therefore, it is hard to investigate the impact of thunderstorms on surface NO_x and O_3 accurately. The general approach is to examine the effect of lightning NO_x on surface O_3 concentrations through comparisons of two sensitivity simulations with/without lightning NO_x, which generally induces the enhancement of surface O_3 concentrations due to lightning NO_x [*Allen et al.*, 2012; *Koshak et al.*, 2014]. However, this method ignores the impact of downdrafts on surface O_3 concentrations, which was suggested by *Bharali et al.* [2015] through comparisons of nighttime surface O_3 concentrations during non-thunderstorm days and those during thunderstorm days.

In this study, we investigate the impacts of thunderstorm downdrafts on surface O_3 concentrations in the summer (June, July, August) of 2011 over the contiguous United States (CONUS). We describe the datasets and models used in this study in section 5.2, including lightning observations from U.S. National Lightning Detection Network (NLDN), surface NO_2, NO, and O_3 measurements from EPA Air Quality System (AQS), the Regional chEmistry and trAnsport Model (REAM), and the Weather and Research Forecasting (WRF) model. In section 5.3, we first improve the convective downdraft parameterization in REAM by examining the influences of thunderstorms on daytime and nighttime surface O_3 concentrations and analyses of idealized supercell simulations from WRF. By the updated downdraft parameterization, we then explore the impact of thunderstorm downdrafts and lightning NO_x on surface O_3 concentrations through comparisons between sensitivity simulations. Finally, section 5.4 gives a summary of the study.

5.2 Observation data and model description

5.2.1 WRF

We used WRF (v 3.9) in this study to include the feedbacks of sub-grid convective clouds to radiation balance [*Alapaty et al.*, 2012; *Herwehe et al.*, 2014], which is essential to correctly derive the impacts of thunderstorms on surface O_3 concentrations in the daytime due to the significant reduction of solar radiation reaching surface during thunderstorm events. We chose the Kain-Fritsch (KF) scheme for convection parameterization [*Kain,* 2004] and the Yonsei University (YSU) scheme for boundary layer parameterization [*Hong et al.,* 2006]. A WRF simulation from May 20 – September 2, 2011,

with a horizontal resolution of 36 km × 36 km and initialization and boundary conditions constrained by the NCEP coupled forecast system model version 2 (CFSv2) products (http://rda.ucar.edu/datasets/ds094.0/) [*Saha et al.*, 2011] provided the meteorology fields for this study. Figure 5.1 compares the simulated precipitation during June – August with gridded precipitation estimates from *Newman et al.* [2015] based on observations. Generally, the WRF simulation captured the precipitation distribution features (R^2 = 0.61) but underestimated precipitation by 21% (WRF: 1.49 mm day^{-1}; gridded: 1.89 mm day^{-1}) in June – August 2011 over the CONUS.

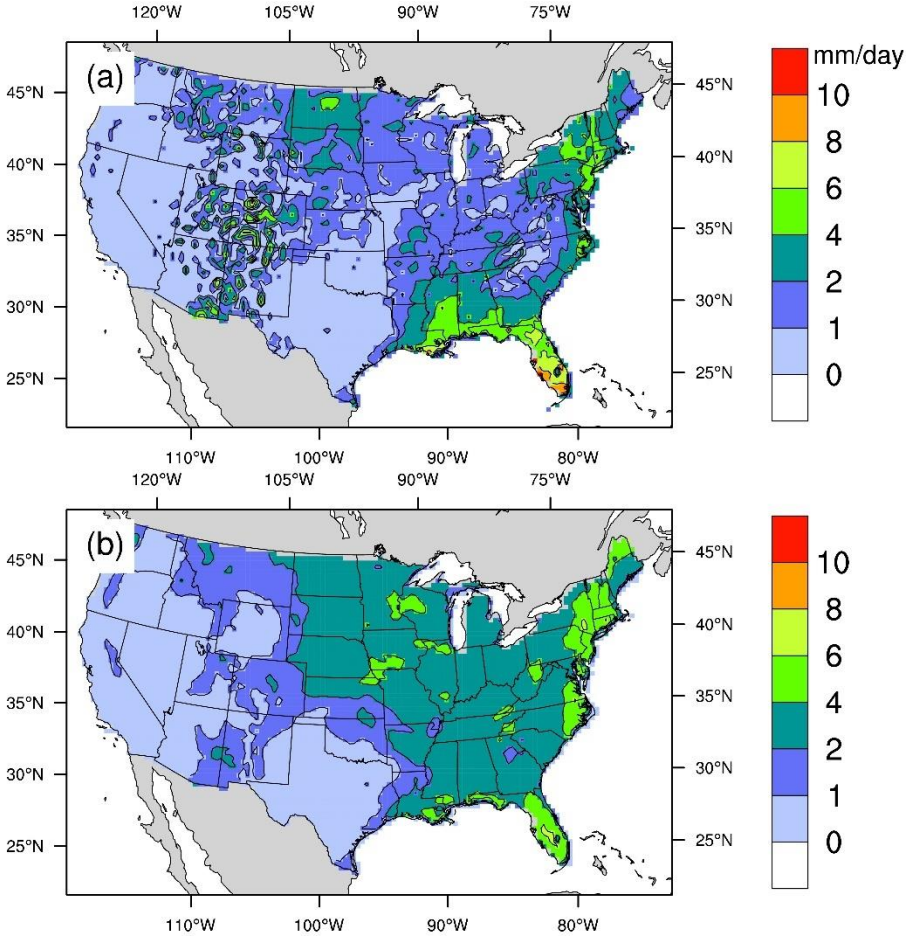

Figure 5. 1 Comparison of the precipitation distributions from our WRF simulation (a) and gridded estimates (b) from *Newman et al.* [2015] during June – August 2011 over the CONUS.

Based on the above WRF simulation, we extracted surface pressures, surface potential temperatures, surface vapor mixing ratios, and horizontal wind velocities (U and V), vapor mixing ratios, potential temperatures, and heights for each model level for deep convection events over the CONUS. The 3-month averages of these variables provided the soundings for WRF idealized supercell simulations (horizontal resolution: 500×500 m^2), which were used to investigate the updraft and downdraft features of deep convections. Figure 5.2 shows the vertical distributions of U, V, potential temperatures, and vapor mixing ratios.

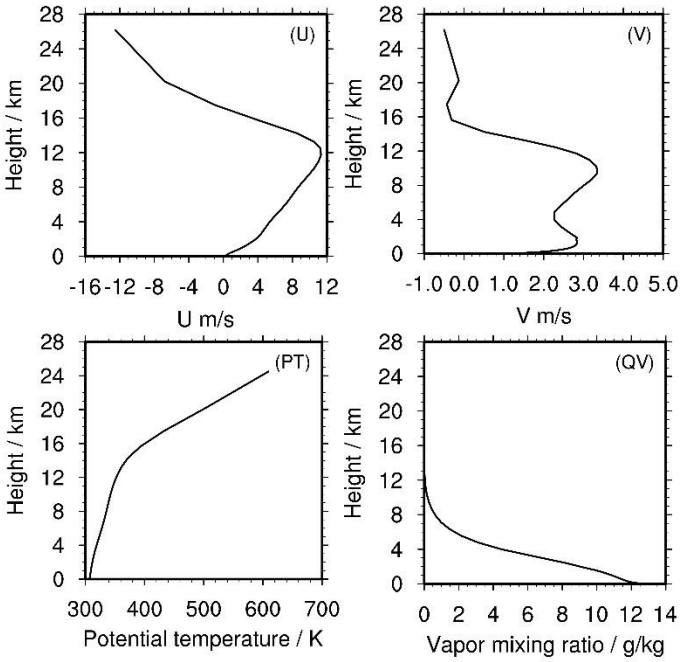

Figure 5. 2 WRF simulated vertical distributions of U, V, potential temperatures, and vapor mixing ratios from deep convection events over the CONUS during June – August 2011.

5.2.2 REAM

REAM has been applied in many types of research involving tropospheric chemistry and transport and emission estimations over East Asia, North America and polar regions [*Alkuwari et al.*, 2013; *Cheng et al.*, 2017; *Cheng et al.*, 2018; *Y. Choi et al.*, 2008a; *Y. Choi et al.*, 2008b; *Gu et al.*, 2014; *Gu et al.*, 2013; *Koo et al.*, 2012; *Liu et al.*, 2014; *Liu et al.*, 2012b; *Yuhang Wang et al.*, 2007; *Q. Yang et al.*, 2011; *R. Zhang et al.*, 2017b; *R. Zhang et al.*, 2018; *Y. Zhang and Wang*, 2016; *C. Zhao and Wang*, 2009; *C. Zhao et al.*, 2009a; *C. Zhao et al.*, 2010]. The model has a horizontal resolution of 36 km × 36 km with 30 vertical layers in the troposphere. Transport is driven by meteorology fields from the above WRF v3.9 simulation. The chemistry mechanism is from the GEOS-Chem model (v11.01) with updated aerosol uptake of isoprene nitrate based on *Fisher et al.* [2016]. Chemistry boundary conditions and initiations are from a GEOS-Chem simulation with a resolution of 2° × 2.5°. Anthropogenic NO_x, CO and VOC emissions are from the National Emission Inventory 2011 (NEI2011) provided by the Pacific Northwest National Laboratory (PNNL). We assume that the weekend emissions are two-thirds of the weekday emissions [*Y. Choi et al.*, 2012; *Kaynak et al.*, 2009]. This study focuses on weekday analysis to minimize the uncertainties of weekend emissions. Biogenic VOC emissions are from MEGAN v2.1 [*Guenther et al.*, 2012] constrained by meteorology fields from the above WRF simulation. Soil NO_x emissions are calculated with the scheme introduced by *Hudman et al.* [2012] with meteorology fields from our WRF simulation. We improve eddy diffusivity coefficients (k_{zz}) from 18:00 – 5:00 following the method described in Chapter 2. We estimate lightning flashes for deep convection events following the method of *Luo et al.* [2017] but with our updated cloud-ground (CG, flashes $minute^{-1}$) fitting results

(Equation 5.1) based on convective available potential energy (CAPE, J kg^{-1}) and updraft mass flux (UMF, kg m^{-2} min^{-1}) at about 500 hPa from our WRF simulation results. Figure 5.3 shows the comparison (R^2 = 0.63) of the CG flash distributions between our estimates and NLDN observations (described below) during June – August 2011 over the CONUS. Lightning NO_x production rate is from *Koshak et al.* [2014] with 384 moles NO per CG flash and 35 moles NO per intra-cloud (IC) flash. Pre-convection lighting NO_x profiles for IC and CG are from *Luo et al.* [2017]. We update the convection of lightning NO_x through the incorporation of 80% pre-convection lightning NO_x in convective downdrafts and updrafts as *Parsons* [2000] demonstrated that 68% - 79% of lightning happened within five nautical miles (9.26 km) of the lightning cluster center which is the typical size of thunderstorms. Therefore, part of lightning NO_x is in the updrafts/downdrafts but not mixed with the nearby environment before convection. The previous approach mixes all lightning NO_x with environmental air before convection, which significantly underestimates the impact of downdrafts/updrafts on lightning NO_x vertical transport unless post-convection lightning NO_x profiles are used.

$$CG = 0.754 \times CAPE^{0.0498} + 6.05 \times 10^{-5} \times CAPE \times UMF + 0.120 \times UMF^{0.907} \quad (5.1)$$

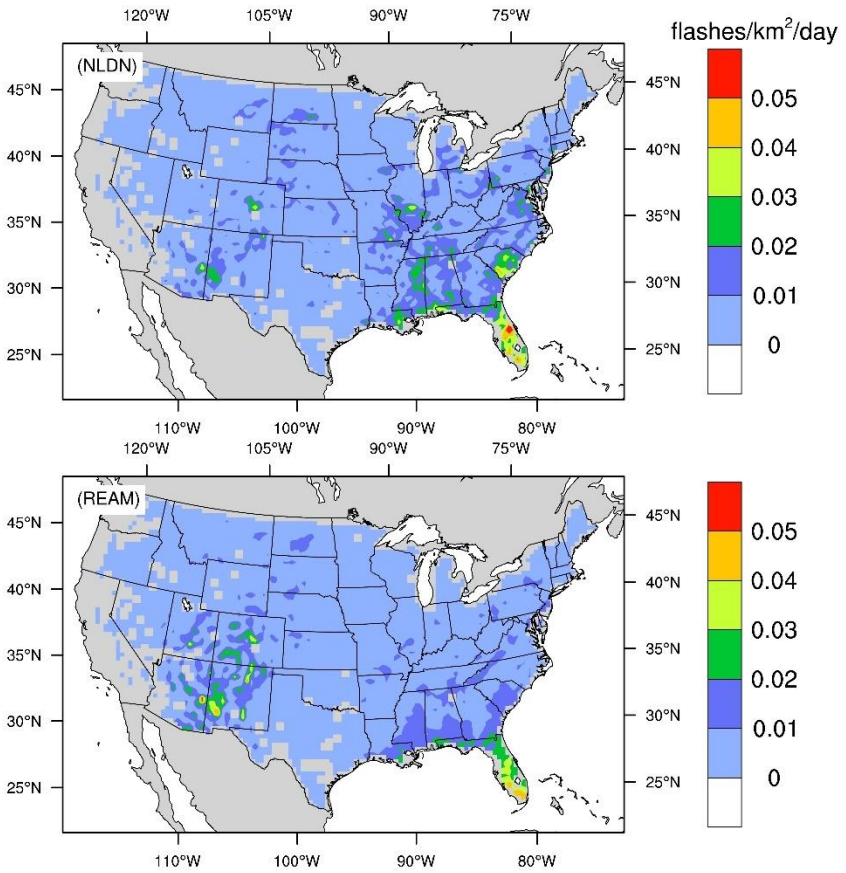

Figure 5. 3 CG flash distributions during June – August 2011 over the CONUS from our estimates and NLDN observations.

5.2.3 NLDN lightning observations

We obtained lightning observations during June – August 2011 from the NLDN datasets. NLDN sensors use magnetic direction signals and time-of-arrival measurements to determine the location and occurrence time of each lightning event across the CONUS. NLDN datasets have been validated with ground-truth video and rocket-triggered lightning [*Biagi et al.*, 2007; *Jerauld et al.*, 2005; *Nag et al.*, 2011]. The CG flash detection efficiency is greater than 95% over the CONUS and the IC flash detection efficiency is 40% - 60% [*Buck et al.*, 2014; *VAISALA*, 2015]. Lighting type classification (IC versus CG) accuracy

is about 90% [*VAISALA*, 2015]. Median location accuracy is 150 – 250 m over the CONUS [*Buck et al.*, 2014; *VAISALA*, 2015]. Lightning event timing precision is 0.5 microsecond [*VAISALA*, 2015]. In this study, we archived NLDN datasets into 5-minute bins and on our model grids.

5.2.4 AQS surface measurements

We downloaded O_3, NO_2 and NO surface concentration measurements from June to August in 2011 from the EPA Air Quality System (AQS) Data Mart (https://www3.epa.gov/airdata/). We scaled NO_2 measurements from the Federal Reference Method (FRM) instruments by using the "C42" hourly ratios in Figure 2.2 in Chapter 2. Then, we add NO_2 and coincident NO concentrations together to get hourly NO_x concentrations. We projected NO_x and O_3 sites on our model grids and excluded those sites with no NLDN lightning events during June – August in their corresponding grids. Finally, we obtained 1149 O_3 and 283 NO_x sites, and Figure 5.4 shows their locations.

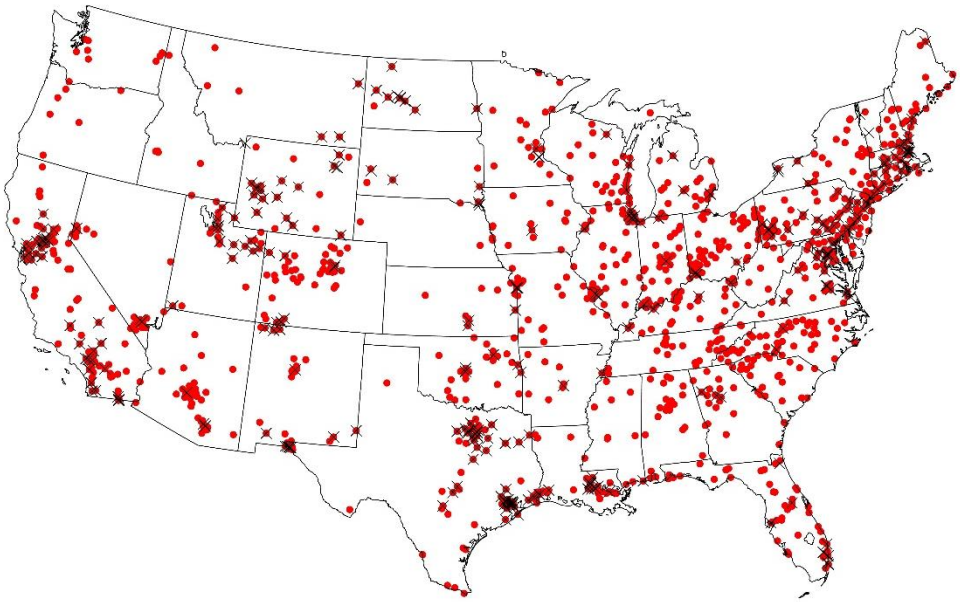

Figure 5. 4 Distributions of AQS O_3 and NO_x measurement sites used in this study. Red dots denote O_3 sites, and black crosses denote NO_x sites.

5.3 Results and discussion

5.3.1 Improvement of convective downdraft parameterization

To minimize the impact of other environmental conditions on surface O_3 and NO_x concentrations, we calculated ΔO_3 (Equation 5.2) and ΔNO_x to investigate the influence of thunderstorms on surface O_3 and NO_x.

$$\Delta(t) = c(t) - c(t-1) \quad (5.2)$$

where *t* denotes time (hour); *c(t)* denotes the O_3 (NO_x) concentration at hour *t*; therefore Δ denotes the change of O_3 (NO_x) from hour *t-1* to hour *t*. To further reduce the impact of previous thunderstorms on ΔO_3 (ΔNO_x) at hour *t*, we excluded ΔO_3 (ΔNO_x) when there were lightning events in the past five hours. Finally, ΔO_3 (ΔNO_x) was marked as a

lightning scenario if there are lightning events from *t*-1 to *t* and a non-lightning scenario if no lightning events during the period.

Through comparisons of ΔO_3 and ΔNO_x between lightning scenarios and non-lightning scenarios, we found no significant differences of observed ΔNO_x between lightning and non-lightning scenarios (Figure 5.5.b) but significant decreases of observed ΔO_3 in the daytime and increases of ΔO_3 during the daytime (Figure 5.5.a). REAM could capture the declines of ΔO_3 for lightning scenarios in the daytime but was unable to reproduce the increases of ΔO_3 for lightning scenarios during the nighttime. The impact of thunderstorms on atmospheric chemistry in the daytime is somewhat complicated, such as decreasing boundary layer height (PBLH) and biogenic isoprene emissions due to cloud blocking solar radiation and decreasing thermal instability (Figures 5.8.a and 5.8.c) and increasing soil NO_x emissions (Figure 5.8.b) due to increases in soil moisture induced by convective precipitation. However, most CONUS regions are NO_x-limited as mentioned in Chapter 3, and boundary layer mixing is strong enough from 12:00 – 16:00, the dominant effect of thunderstorms on surface O_3 in the daytime is the reduction of solar radiation reaching surface caused by cumulus cloud, which slows down O_3 production rate below the cloud, as shown in Figure 5.5.

Nighttime O_3 chemistry is relatively more straightforward: O_3 is mainly consumed by NO_x ($O_3 + NO \rightarrow NO_2 + O_3$; $O_3 + NO_2 \rightarrow NO_3 + NO_2$), and there is no significant chemistry production of ozone during the nighttime. The large-scale horizontal wind fields are small for lightning scenarios (Figure 5.2). Therefore, the only potential source of elevated ΔO_3 is from upper layers with higher O_3 concentrations than the surface.

During lightning events, there are two ways to transport upper layers to the surface: downdraft and boundary layer mixing, which may be underestimated by the 36-km WRF simulation.

We ran idealized supercell simulations by using soundings from the 36-km WRF simulation (Figure 5.2). Both the surface initialized (Figure 5.6, which stands for a typical daytime thunderstorm event) and elevated initialized (Figure 5.7, which stands for a typical nighttime thunderstorm event) simulations shown that downdraft mass fluxes (DMFs) are comparable to UMFs and DMF heights are close to UMF heights. It is entirely different from the DMFs produced by the KF scheme in the 36-km WRF simulation (Figures 5.6.c and 5.6.d). The KF scheme produces a significantly lower and weaker downdraft compared to updraft (Figure 5.6.d). The vertical-integrated DMF is only about 16% of the total UMF, but the idealized simulations show values of about 80% (Figures 5.6 and 5.7). More idealized sensitivity simulations with different initialization conditions produce similar results: equal heights of UMF and DMF, and DMF is generally over 50% of UMF. Our idealized simulation results with comparable DMFs and UMFs are consistent with radar reflectivity observations, Doppler velocity measurements, cloud-resolving model simulations [*Didlake Jr and Houze Jr*, 2009; *Giangrande et al.*, 2016; *Kumar et al.*, 2016; *Mrowiec et al.*, 2012; *J. Yang et al.*, 2016]. It seems the KF scheme only considers the precipitation-induced downdraft but ignore the downdrafts surrounding updrafts in the upper layers. Therefore, we adjusted downdrafts from the KF scheme: 1), made downdrafts the same high as corresponding updrafts; 2), scaled the vertical-integrated downdrafts half of the corresponding updrafts; 3), adjusted downdrafts, downdraft entrainments, downdraft detrainment at each level

based on the downdraft algorithm from *Kain* [2004]. The adjusted DMF vertical profile is shown in Figure 5.6.d, which is significantly improved compared to the original DMF profile.

Unlike daytime, thermal instability is not dominant in the nighttime boundary layer. Therefore, the impact of thunderstorms on thermal instability during the nighttime is ignorable compared to daytime (Figure 5.8.a). While, *Eberle* [2016] found that thunderstorms after sunset improved turbulent kinetic energy (TKE) and momentum flux which contributed to turbulent mixing, but the improvement of TKE and momentum flux disappeared soon as thunderstorm dissipated [*Eberle*, 2016]. So, we increased k_{zz} by 100% for those lightning scenarios during the nighttime (18:00 – 5:00). After these two adjustments, REAM reproduced well the nighttime increases of ΔO_3 for lightning scenarios (Figure 5.5.e).

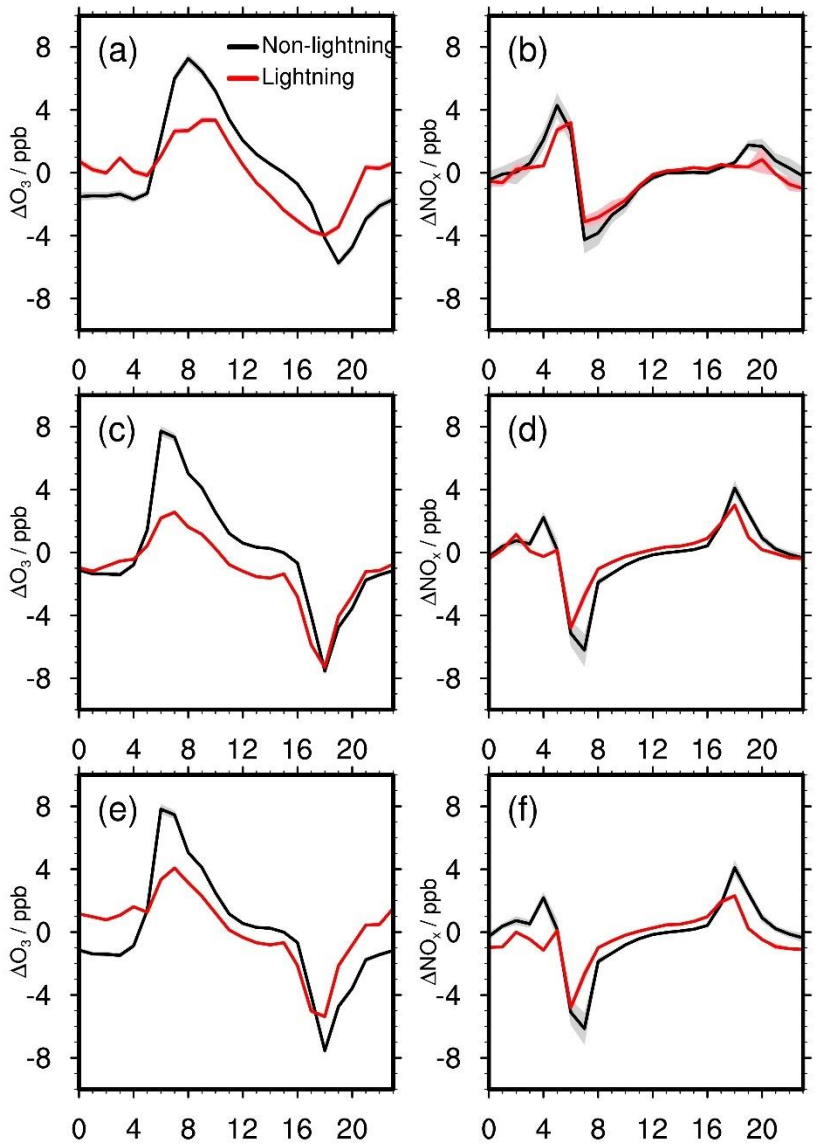

Figure 5. 5 Diurnal cycles of ΔO_3 (left panels) and ΔNO_x (right panels) for AQS observations (a, b), the original REAM simulation (c, d), and the REAM simulation with updated downdraft parametrization and improvement of k_{zz} at nighttime thunderstorm hours (e, f). Light shading areas denote uncertainties, which may not show up when uncertainties are small.

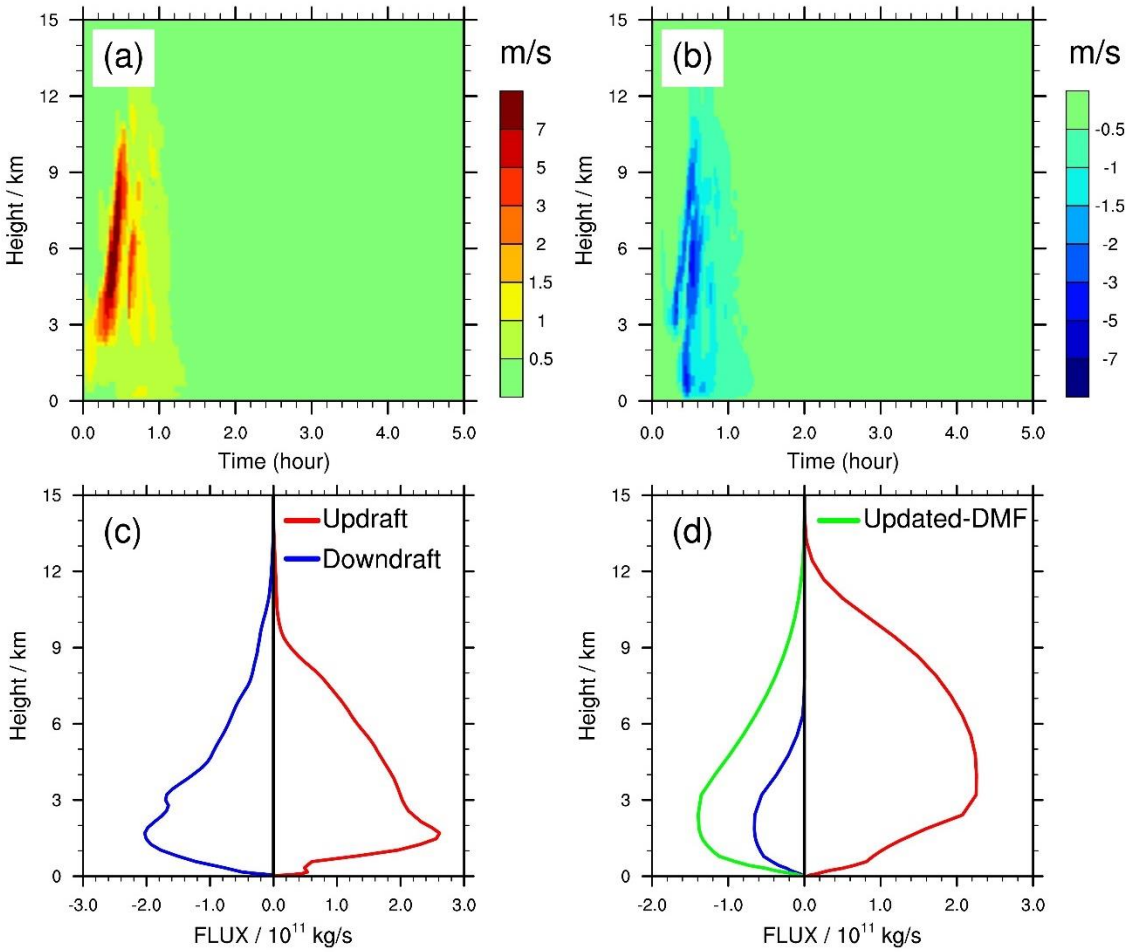

Figure 5. 6 Simulated evolution of positive (a) and negative (b) vertical velocities since the initialization of the thunderstorm by using the idealized WRF supercell model. Only vertical velocities with absolute values great than 0.5 m s^{-1} are regarded as updraft/downdraft. (c) Vertical distributions of UMF and downdraft mass flux (DMF) during the thunderstorm event from the supercell simulation. (d) Vertical distributions of UMF and DMF from the 36-km WRF simulation during June – August 2011 over the CONUS and distributions of our updated DMF.

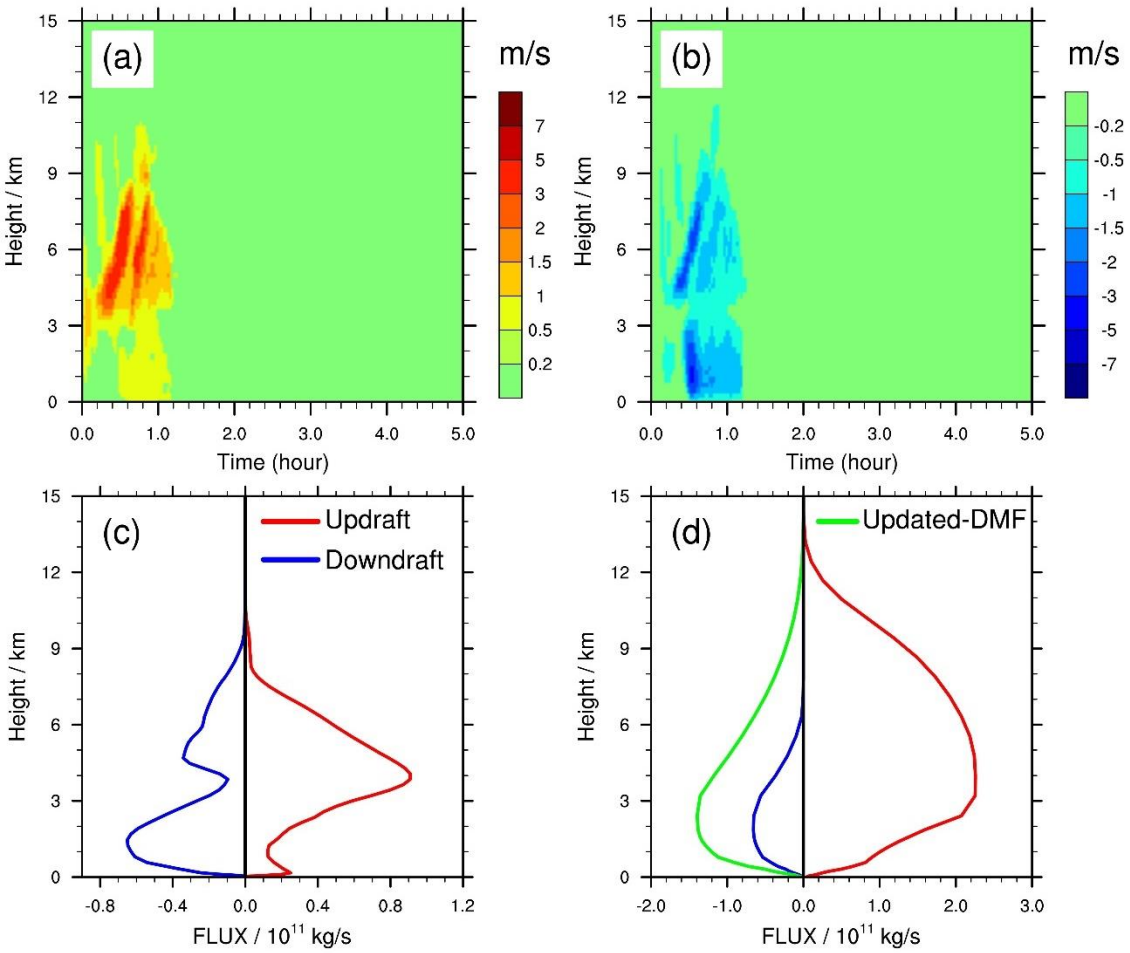

Figure 5. 7 Same as Figure 5.6, but increase the supercell initialization height to 1.5 km.

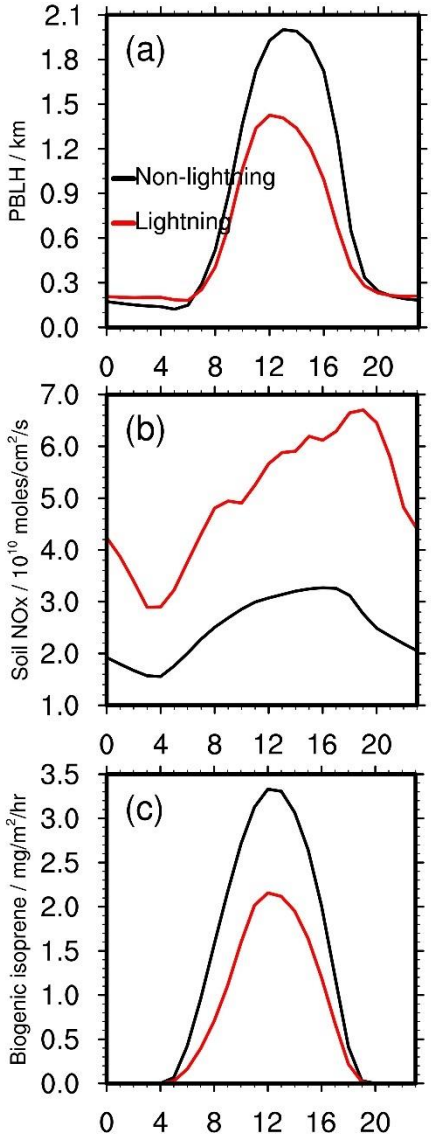

Figure 5. 8 Simulated diurnal cycles of boundary layer height, soil NO_x emissions, and biogenic isoprene emissions for non-lightning and lightning scenarios during June – August 2011 over the CONUS.

5.3.2 Impact of thunderstorms on surface O_3 and NO_x concentrations

We first examined the impact of updated downdrafts on post-convection lightning NO_x vertical distributions. As shown in Figure 5.9, the original downdrafts produced a unimodal post-convection profile peaked at around 6 km, while updated downdrafts

distributed lightning NO_x more evenly and provided a bimodal post-convection profile with another peak at about 500 m. The bimodal post-convection profile is different from *Ott et al.* [2010] but in agreement with *Pickering et al.* [1998], reflecting the importance of downdraft adjustment in this study. *Ott et al.* [2010] also found the downward transport of lightning NO_x after convection, but it seems their transport effect was not as significant as ours.

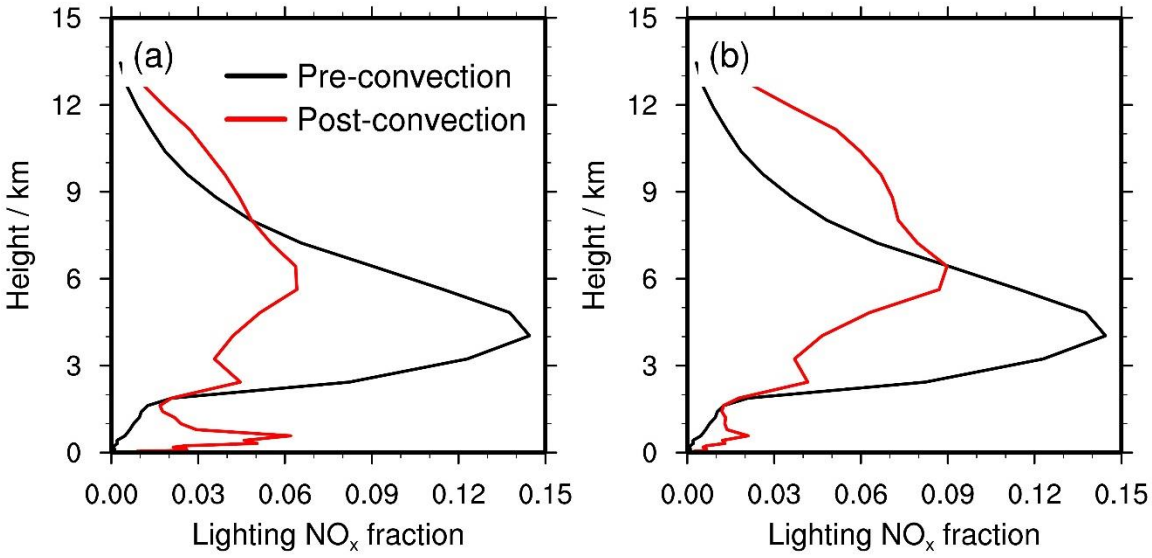

Figure 5. 9 Comparison of pre-convection and post-convection (5 minutes after pre-convection) lightning NO_x vertical profiles for (a) updated DMFs and (b) original DMFs from the KF scheme.

We ran two more REAM sensitivity simulations to investigate the impact of thunderstorms on surface O_3: one with original DMFs but turning off lightning NO_x emissions (hereafter refer to as Simulation 3) and the other one with updated DMF with no lightning NO_x emissions (hereafter referred to as Simulation 4). The simulation with

original DMF and lightning NO_x turning on is Simulation 1, while the simulation with updated DMF and lightning NO_x is denoted as Simulation 2. Figure 5.10 shows the differences in maximum daily 8-hour average (MDA8) O_3 concentrations among difference simulations. We found that updated downdrafts significantly improve MDA8 (Figures 5.10.a and 5.10.b) over regions with strong lighting activities. Without updated downdrafts, lightning NO_x emissions improve MDA8 in the southeast CONUS by only 1.2 – 16 ppb, which is consistent with *Koshak et al.* [2014] which examined the impact of lightning NO_x on O_3 concentrations through sensitivity simulations from the Community Multiscale Air Quality (CMAQ) modeling system in August 2006 and found 0.5 – 1.5 ppb increase of average O_3 concentrations in the boundary layer due to lighting NO_x. However, with our updated downdrafts, lightning NO_x increases MDA8 by 2.4 – 3.6 ppb in the southeast and generally > 4.0 ppb over the southern mountain regions (Arizona and Utah).

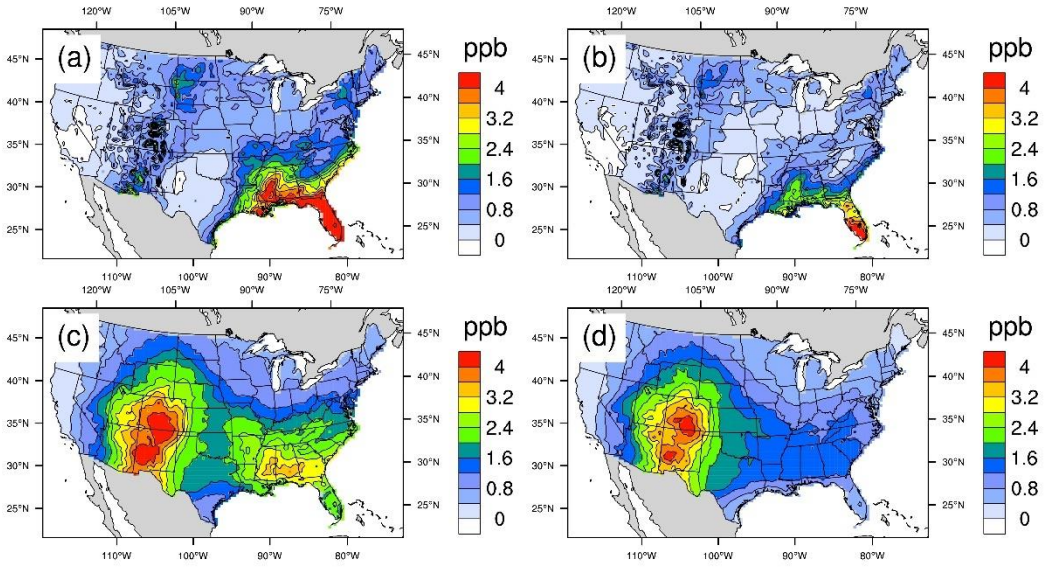

Figure 5. 10 The differences of MDA8 O_3 concentrations among different simulations during June – August 2011 over the CONUS: (a), Simulation 2 – Simulation 1; (b), Simulation 4 – Simulation 3; (c), Simulation 2 – Simulation 4; (d) Simulation 1 – Simulation 3.

5.4 Conclusion

We investigated the impact of thunderstorms on surface O_3 and NO_x concentrations during the summer of 2011 over the CONUS through observation analyses and model sensitivity simulations. We found that generally, thunderstorms decreased ΔO_3 in the daytime due to the dominant role of solar radiation reduction reaching the surface and increased ΔO_3 during the nighttime due to convective downdrafts and increased nocturnal boundary layer mixing. REAM couldn't capture the nighttime thunderstorm features due to underestimated DMFs from the KF scheme and the missing of mechanical vertical mixing during the thunderstorm events. After our adjustment of DMFs and k_{zz} during nighttime thunderstorms, REAM well reproduced the observed characteristics.

With the adjusted DMFs, post-convection NO_x shown a bimodal shape with one peak near the surface in contrast to the unimodal post-convection shape produced from the original KF DMF peaking at about 6 km. Moreover, the adjusted DMFs significantly improved the impact of thunderstorms/lightning NO_x on MDA8 over the CONUS, especially in Arizona, Utah, and the southeastern United States. We suggest the underestimated impact of thunderstorms on surface O_3 concentrations from previous studies and that the contribution of downdrafts to surface O_3 is as much as lightning NO_x

itself. We recommend further investigation of downdraft characteristics in deep convection.

CHAPTER 6. Conclusions and future work

6.1 Summary of findings

6.1.1 Evaluations of NEI anthropogenic NO_x emissions and the YL soil NO_x emissions

This study evaluated the simulated diurnal cycles of surface NO_2, NO_2 vertical profiles, and NO_2 TVCD from REAM with observations from air quality monitoring sites, aircraft, Pandora, OMI, and GOME-2A during the Discover-AQ 2011 campaign. REAM well reproduces the observed diurnal cycles of surface NO_2, NO_2 vertical profiles, and NO_2 TVCD on both weekdays and weekends at the 36-km scale but overestimates NO_2 concentrations and TVCD at the 4-km scale. We conclude that the NEI2011 may not well capture the distributions of NO_x emissions at 4 km scale but provide good estimates of NO_x emissions at the 36-km scale. The evaluation of NEI2011 NO_x emissions at the 36-km scale is further corroborated by comparisons of simulated and observed O_3 peak time and peak values in July 2011 over the CONUS. However, the underestimation of O_3 peak values in the South suggest the underestimation of soil NO_x emissions from the Yienger and Levy (YL) scheme.

Through the analyses of the nonlinear relationships among NO_x emissions, NO_2 TVCDs, and NO_2 surface concentrations, we find consistent variations among NO_2 surface concentrations, satellite NO_2 TVCDs, and EPA NO_x emissions over the CONUS urban regions from 2003 – 2017, which again validate NEI NO_x emission estimates at the 36-km scale.

6.1.2 O_3 peak time as an independent constraint on the diagnostics of NO_x and VOC emissions

This study evaluated the dependence of O_3 peak values and time on NO_x and VOC emissions through model simulations with different emission scenarios in July 2011 over the CONUS. In addition to the previously known dependence of O_3 peak values on NO_x and VOC emissions, we find that O_3 peak time is affected by NO_x and VOC emissions in a different manner. Over regions with extensive biogenic isoprene emissions, such as the Central, South, Southeast, and Northeast regions, the O_3 peak values are sensitive to the emissions of NO_x but not VOCs. However, O_3 peak time in these regions is sensitive to isoprene emissions, where an increase of isoprene emissions leads to earlier peak time of surface O_3. As such, the observations of O_3 peak time provide another useful constraint on model emissions of NO_x and VOCs. We confirm the overestimation of biogenic isoprene emissions from MEGAN on the basis of the underestimations of O_3 peak time in the Central, South, and Southeast.

6.1.3 Selection of urban regions to infer anthropogenic NO_x emission variations from satellite NO_2 TVCDs

This study illustrates the nonlinear relationships among NO_x emissions, NO_2 tropospheric vertical column densities (TVCDs), and NO_2 surface concentrations using the REAM simulations for July 2011 over the contiguous United States (CONUS). The variations of NO_2 surface concentrations and TVCDs are generally consistent and reflect well anthropogenic NO_x emission variations for high-NO_x emission regions. For low-NO_x emission regions, however, nonlinearity in the emission-TVCD relationship makes it difficult to use satellite observations to infer anthropogenic NO_x emission changes. The

finding is extended to other periods by the contrast of similar variations of NO_2 surface measurements from coincident satellite NO_2 tropospheric VCD over urban regions in comparison to large variation differences between surface and satellite observations over rural regions. We find a continuous decrease of anthropogenic NO_x emissions after 2011 by examining surface and satellite measurements in CONUS urban regions, but the decreasing rate is lower by 9% - 46% than the pre-2011 period.

6.1.4 Underestimated impact of thunderstorms on surface O_3 and NO_x

This study investigated the impact of thunderstorms on surface O_3 and NO_x concentrations during the summer of 2011 over the CONUS through observation analyses and model sensitivity simulations. We find that generally, thunderstorms decrease ΔO_3 in the daytime due to the dominant role of solar radiation reduction reaching the surface and increase ΔO_3 during the nighttime due to convective downdrafts and increased nocturnal boundary layer mixing. REAM couldn't capture the nighttime increase features due to underestimated DMFs from the KF scheme and the missing of mechanical vertical mixing during the thunderstorm events. After our adjustment of DMFs and k_{zz} during nighttime thunderstorms, REAM well reproduces the observed characteristics. With the adjusted DMFs, post-convection NO_x shown a bimodal shape with one peak near the surface in contrast to the unimodal post-convection shape produced from the original KF DMF peaking at about 6 km. Moreover, the adjusted DMFs almost double the impact of thunderstorms/lightning NO_x on MDA8 over the CONUS: lightning NO_x increases MDA8 by 2.4 – 3.6 ppb on average in the southeastern United States.

6.2 Future work

6.2.1 Further evaluations of NEI NO_x emissions with different observations

Due to significant spatial and temporal inhomogeneity of NO_x emissions, different studies have distinct evaluations of NEI NO_x emissions. I recommend further evaluations of NEI NO_x emissions with more different measurements and methods.

6.2.2 Further investigation of the relationship between O_3 peak time and NO_x and VOC emissions

This study constructed the domain-mean sensitivity of O_3 peak time to NO_x and VOC emissions. I wonder whether there exists another isopleth diagram for O_3 peak time as O_3 peak values. I recommend sensitivity simulations with box models to explore more detailed relationships between O_3 peak time and NO_x and VOC emissions.

6.2.3 Further investigation of thunderstorms' impact on surface ozone

This study investigated the impact of thunderstorms on surface O_3 through comparisons between model simulations with/without lightning NO_x, which reflected the long-term average contributions of lightning NO_x to surface O_3, which is significantly different from the impact of thunderstorms on ΔO_3 as discussed in section 5.2.1. Downdraft and solar radiation reduction from thunderstorms in the daytime produce opposite effects on surface O_3. Further research needs to explore their separate contributions to surface O_3 and whether the downdraft effect can be stronger than solar radiation reduction and under what conditions.

References

Acarreta, J. R., J. F. de Haan, and P. Stammes (2004), Cloud pressure retrieval using the O_2 - O_2 absorption band at 477 nm, *Journal of Geophysical Research: Atmospheres*, *109*(D5), doi:10.1029/2003JD003915.

Alapaty, K., J. A. Herwehe, T. L. Otte, C. G. Nolte, O. R. Bullock, M. S. Mallard, J. S. Kain, and J. Dudhia (2012), Introducing subgrid - scale cloud feedbacks to radiation for regional meteorological and climate modeling, *Geophysical Research Letters*, *39*(24), doi:10.1029/2012GL054031.

Alkuwari, F. A., S. Guillas, and Y. Wang (2013), Statistical downscaling of an air quality model using Fitted Empirical Orthogonal Functions, *Atmospheric environment*, *81*, 1-10, doi:10.1016/j.atmosenv.2013.08.031.

Allen, D. J., K. Pickering, B. Duncan, and M. Damon (2010), Impact of lightning NO emissions on North American photochemistry as determined using the Global Modeling Initiative (GMI) model, *Journal of Geophysical Research: Atmospheres*, *115*(D22), doi:10.1029/2010JD014062.

Allen, D. J., K. E. Pickering, R. W. Pinder, B. H. Henderson, K. W. Appel, and A. Prados (2012), Impact of lightning-NO on eastern United States photochemistry during the summer of 2006 as determined using the CMAQ model, *Atmospheric Chemistry and Physics*, *12*(4), 1737-1758, doi:10.5194/acp-12-1737-2012.

Anderson, D. C., C. P. Loughner, G. Diskin, A. Weinheimer, T. P. Canty, R. J. Salawitch, H. M. Worden, A. Fried, T. Mikoviny, and A. Wisthaler (2014), Measured and modeled CO and NO_y in DISCOVER-AQ: An evaluation of emissions and chemistry over the eastern US, *Atmospheric environment*, *96*, 78-87, doi:10.1016/j.atmosenv.2014.07.004.

Barth, M. C., M. M. Bela, A. Fried, P. O. Wennberg, J. D. Crounse, J. M. St. Clair, N. J. Blake, D. R. Blake, C. R. Homeyer, and W. H. Brune (2016), Convective transport and scavenging of peroxides by thunderstorms observed over the central US during DC3, *Journal of Geophysical Research: Atmospheres*, *121*(8), 4272-4295.

Barth, M. C., J. Lee, A. Hodzic, G. Pfister, W. C. Skamarock, J. Worden, J. Wong, and D. Noone (2012), Thunderstorms and upper troposphere chemistry during the early stages of the 2006 North American Monsoon, *Atmos. Chem. Phys.*, *12*(22), 11003-11026, doi:10.5194/acp-12-11003-2012.

Beaver, M., K. Kronmiller, R. Duvall, S. Kaushik, T. Morphy, P. King, and R. Long (2013), Direct and Indirect Methods for the Measurement of Ambient Nitrogen Dioxide, in *AWMA Measurement Technologies meeting*, edited, p. 6, Sacramento, CA, US.

Beaver, M., R. Long, and K. Kronmiller (2012), Characterization and Development of Measurement Methods for Ambient Nitrogen Dioxide (NO_2), in *National Air Quality Conference - Ambient Air Monitoring 2012*, edited, p. 29, Denver, CO, US.

Beirle, S., U. Platt, M. Wenig, and T. Wagner (2003), Weekly cycle of NO_2 by GOME measurements: A signature of anthropogenic sources, *Atmospheric Chemistry and Physics*, *3*(6), 2225-2232, doi:10.5194/acp-3-2225-2003.

Bharali, C., B. Pathak, and P. K. Bhuyan (2015), Spring and summer night-time high ozone episodes in the upper Brahmaputra valley of North East India and their association with lightning, *Atmospheric Environment*, *109*, 234-250, doi:10.1016/j.atmosenv.2015.03.035.

Biagi, C. J., K. L. Cummins, K. E. Kehoe, and E. P. Krider (2007), National lightning detection network (NLDN) performance in southern Arizona, Texas, and Oklahoma in 2003–2004, *Journal of Geophysical Research: Atmospheres*, *112*(D5), doi:10.1029/2006JD007341.

Bishop, G. A., and D. H. Stedman (2015), Reactive nitrogen species emission trends in three light-/medium-duty United States fleets, *Environmental science & technology*, *49*(18), 11234-11240, doi:10.1021/acs.est.5b02392.

Boersma, K. F., H. J. Eskes, and E. J. Brinksma (2004), Error analysis for tropospheric NO_2 retrieval from space, *Journal of Geophysical Research: Atmospheres*, *109*(D4), doi:10.1029/2003JD003962.

Boersma, K. F., H. J. Eskes, R. J. Dirksen, J. P. Veefkind, P. Stammes, V. Huijnen, Q. L. Kleipool, M. Sneep, J. Claas, and J. Leitão (2011), An improved tropospheric NO_2 column retrieval algorithm for the Ozone Monitoring Instrument, *Atmospheric Measurement Techniques*, *4*(9), 1905-1928, doi:10.5194/amt-4-1905-2011.

Boersma, K. F., H. J. Eskes, A. Richter, I. De Smedt, A. Lorente, S. Beirle, J. H. van Geffen, M. Zara, E. Peters, and M. V. Roozendael (2018), Improving algorithms and uncertainty estimates for satellite NO_2 retrievals: results from the quality assurance for the essential climate variables (QA4ECV) project, *Atmospheric Measurement Techniques*, *11*(12), 6651-6678, doi:10.5194/amt-11-6651-2018.

Boersma, K. F., D. J. Jacob, H. J. Eskes, R. W. Pinder, J. Wang, and R. J. Van Der A (2008), Intercomparison of SCIAMACHY and OMI tropospheric NO_2 columns: Observing the diurnal evolution of chemistry and emissions from space, *Journal of Geophysical Research: Atmospheres*, *113*(D16), doi:10.1029/2007JD008816.

Boersma, K. F., D. J. Jacob, M. Trainic, Y. Rudich, I. De Smedt, R. Dirksen, and H. J. Eskes (2009), Validation of urban NO_2 concentrations and their diurnal and seasonal variations observed from the SCIAMACHY and OMI sensors using in situ surface

measurements in Israeli cities, *Atmospheric Chemistry and Physics*, *9*(12), 3867-3879, doi:10.5194/acp-9-3867-2009.

Breuer, H., F. Ács, Á. Horváth, P. Németh, and K. Rajkai (2014), Diurnal course analysis of the WRF-simulated and observation-based planetary boundary layer height, *Advances in Science and Research*, *11*(1), 83-88, doi:10.5194/asr-11-83-2014.

Brohede, S., C. A. McLinden, G. Berthet, C. S. Haley, D. Murtagh, and C. E. Sioris (2007), A stratospheric NO_2 climatology from Odin/OSIRIS limb-scatter measurements, *Canadian Journal of Physics*, *85*(11), 1253-1274, doi:10.1139/p07-141.

Brown, S. S., J. E. Dibb, H. Stark, M. Aldener, M. Vozella, S. Whitlow, E. J. Williams, B. M. Lerner, R. Jakoubek, and A. M. Middlebrook (2004), Nighttime removal of NO_x in the summer marine boundary layer, *Geophysical Research Letters*, *31*(7), doi:10.1029/2004GL019412.

Buck, T. L., A. Nag, and M. J. Murphy (2014), Improved cloud-to-ground and intracloud lightning detection with the LS7002 advanced total lightning sensor, paper presented at WMO Technical Conference on Meteorological and Environmental Instruments and Methods of Observation, Saint Petersburg, Russian Federation.

Bucsela, E. J., E. A. Celarier, J. L. Gleason, N. A. Krotkov, L. N. Lamsal, S. V. Marchenko, and W. H. Swartz (2016), OMNO2 README Document Data Product Version 3.0*Rep.*, 38 pp, NASA.

Bucsela, E. J., N. A. Krotkov, E. A. Celarier, L. N. Lamsal, W. H. Swartz, P. K. Bhartia, K. F. Boersma, J. P. Veefkind, J. F. Gleason, and K. E. Pickering (2013), A new stratospheric and tropospheric NO_2 retrieval algorithm for nadir-viewing satellite instruments: applications to OMI, *Atmospheric Measurement Techniques*, *6*(10), 2607-2626, doi:10.5194/amt-6-2607-2013.

Canty, T., L. Hembeck, T. Vinciguerra, D. Goldberg, S. Carpenter, D. Allen, C. Loughner, R. Salawitch, and R. Dickerson (2015), Ozone and NO_x chemistry in the eastern US: evaluation of CMAQ/CB05 with satellite (OMI) data, *Atmospheric Chemistry and Physics*, *15*(19), 10965, doi:10.5194/acp-15-10965-2015.

Carlton, A. G., and K. R. Baker (2011), Photochemical modeling of the Ozark isoprene volcano: MEGAN, BEIS, and their impacts on air quality predictions, *Environmental science & technology*, *45*(10), 4438-4445, doi:10.1021/es200050x.

Chance, K. (2002), OMI Algorithm Theoretical Basis Document: OMI Trace Gas Algorithms*Rep. 2.0*, 78 pp, Smithsonian Astrophysical Observatory, Cambridge, MA, USA.

Cheng, Y., Y. Wang, Y. Zhang, G. Chen, J. H. Crawford, M. M. Kleb, G. S. Diskin, and A. J. Weinheimer (2017), Large biogenic contribution to boundary layer O_3 - CO

regression slope in summer, *Geophysical Research Letters*, *44*(13), 7061-7068, doi:10.1002/2017GL074405.

Cheng, Y., Y. Wang, Y. Zhang, J. H. Crawford, G. S. Diskin, A. J. Weinheimer, and A. Fried (2018), Estimator of surface ozone using formaldehyde and carbon monoxide concentrations over the eastern United States in summer, *Journal of Geophysical Research: Atmospheres*, *123*(14), 7642-7655, doi:10.1029/2018JD028452.

Choi, S., J. Joiner, Y. Choi, B. Duncan, A. Vasilkov, N. Krotkov, and E. Bucsela (2014), First estimates of global free-tropospheric NO_2 abundances derived using a cloud-slicing technique applied to satellite observations from the Aura Ozone Monitoring Instrument (OMI), *Atmos. Chem. Phys*, *14*(19), 10,565-510,588, doi:10.5194/acp-14-10565-2014.

Choi, Y., H. Kim, D. Tong, and P. Lee (2012), Summertime weekly cycles of observed and modeled NO_x and O_3 concentrations as a function of satellite-derived ozone production sensitivity and land use types over the Continental United States, *Atmospheric Chemistry and Physics*, *12*(14), 6291-6307, doi:10.5194/acp-12-6291-2012.

Choi, Y., Y. Wang, Q. Yang, D. Cunnold, T. Zeng, C. Shim, M. Luo, A. Eldering, E. Bucsela, and J. Gleason (2008a), Spring to summer northward migration of high O_3 over the western North Atlantic, *Geophysical Research Letters*, *35*(4), doi:10.1029/2007GL032276.

Choi, Y., Y. Wang, T. Zeng, D. Cunnold, E. S. Yang, R. Martin, K. Chance, V. Thouret, and E. Edgerton (2008b), Springtime transitions of NO_2, CO, and O_3 over North America: Model evaluation and analysis, *Journal of Geophysical Research: Atmospheres*, *113*(D20), doi:10.1029/2007JD009632.

Compton, J. C., R. Delgado, T. A. Berkoff, and R. M. Hoff (2013), Determination of planetary boundary layer height on short spatial and temporal scales: A demonstration of the covariance wavelet transform in ground-based wind profiler and lidar measurements, *Journal of Atmospheric and Oceanic Technology*, *30*(7), 1566-1575, doi:10.1175/JTECH-D-12-00116.1.

Crouse, D. L., P. A. Peters, P. Hystad, J. R. Brook, A. van Donkelaar, R. V. Martin, P. J. Villeneuve, M. Jerrett, M. S. Goldberg, and C. A. Pope III (2015), Ambient $PM_{2.5}$, O_3, and NO_2 exposures and associations with mortality over 16 years of follow-up in the Canadian Census Health and Environment Cohort (CanCHEC), *Environmental health perspectives*, *123*(11), 1180, doi:10.1289/ehp.1409276.

Dallmann, T. R., and R. A. Harley (2010), Evaluation of mobile source emission trends in the United States, *Journal of Geophysical Research: Atmospheres*, *115*(D14), doi:10.1029/2010JD013862.

David, L. M., and P. R. Nair (2011), Diurnal and seasonal variability of surface ozone and NO_x at a tropical coastal site: Association with mesoscale and synoptic

meteorological conditions, *Journal of Geophysical Research: Atmospheres*, *116*(D10), doi:10.1029/2010JD015076.

De Gouw, J. A., D. D. Parrish, G. J. Frost, and M. Trainer (2014), Reduced emissions of CO2, NO_x, and SO_2 from US power plants owing to switch from coal to natural gas with combined cycle technology, *Earth's Future*, *2*(2), 75-82, doi:10.1002/2013EF000196.

De Smedt, I., T. Stavrakou, F. Hendrick, T. Danckaert, T. Vlemmix, G. Pinardi, N. Theys, C. Lerot, C. Gielen, and C. Vigouroux (2015), Diurnal, seasonal and long-term variations of global formaldehyde columns inferred from combined OMI and GOME-2 observations, *Atmospheric Chemistry & Physics Discussions*, *15*(8), doi:10.5194/acp-15-12519-2015.

De Smedt, I., N. Theys, H. Yu, T. Danckaert, J. Van Gent, and M. Van Roozendael (2016), S5P/TROPOMI HCHO ATBD*Rep. 1.0.0*, 65 pp.

DenBleyker, A., J. Koupal, T. DeFries, and C. Palacios (2017), Improvement of Default Inputs for MOVES and SMOKE-MOVES: CRC Project A-100*Rep.*, 86 pp, Eastern Research Group, Inc., Austin, TX.

DenBleyker, A., R. E. Morris, C. E. Lindhjem, L. K. Parker, T. Shah, B. Koo, C. Loomis, and J. Dilly Temporal and Spatial Detail in Mobile Source Emission Inventories for Regional Air Quality Modeling.

Dickerson, R. R., G. J. Huffman, W. T. Luke, L. J. Nunnermacker, K. E. Pickering, A. C. D. Leslie, C. G. Lindsey, W. G. N. Slinn, T. J. Kelly, and P. H. Daum (1987), Thunderstorms: An important mechanism in the transport of air pollutants, *Science*, *235*(4787), 460-465, doi:10.1126/science.235.4787.460.

Didlake Jr, A. C., and R. A. Houze Jr (2009), Convective-scale downdrafts in the principal rainband of Hurricane Katrina (2005), *Monthly Weather Review*, *137*(10), 3269-3293, doi:10.1175/2009MWR2827.1.

Diffenbaugh, N. S., M. Scherer, and R. J. Trapp (2013), Robust increases in severe thunderstorm environments in response to greenhouse forcing, *Proceedings of the National Academy of Sciences*, *110*(41), 16361-16366, doi:10.1073/pnas.1307758110.

Dirksen, R. J., K. F. Boersma, H. J. Eskes, D. V. Ionov, E. J. Bucsela, P. F. Levelt, and H. M. Kelder (2011), Evaluation of stratospheric NO_2 retrieved from the Ozone Monitoring Instrument: Intercomparison, diurnal cycle, and trending, *Journal of Geophysical Research: Atmospheres*, *116*(D8), doi:10.1029/2010JD014943.

Drosoglou, T., A. F. Bais, I. Zyrichidou, N. Kouremeti, A. Poupkou, N. Liora, C. Giannaros, M. E. Koukouli, D. Balis, and D. Melas (2017), Comparisons of ground-based tropospheric NO_2 MAX-DOAS measurements to satellite observations with the aid of an

air quality model over the Thessaloniki area, Greece, *Atmospheric Chemistry and Physics*, *17*(9), 5829-5849, doi:10.5194/acp-17-5829-2017.

Drosoglou, T., M. E. Koukouli, N. Kouremeti, A. F. Bais, I. Zyrichidou, D. Balis, J. Xu, and A. Li (2018), MAX-DOAS NO_2 observations over Guangzhou, China; ground-based and satellite comparisons, *Atmospheric Measurement Techniques*, *11*(4), 2239-2255, doi:10.5194/amt-11-2239-2018.

Eberle, G. R. (2016), Characterizing the Effects of Convection on the Afternoon to Evening Boundary Layer Transition During Pecan 2015*Rep.*, Naval Postgraduate School Monterey United States.

EPA (2017), PROFILE OF VERSION 1 OF THE 2014 NATIONAL EMISSIONS INVENTORY*Rep.*, U.S. Environmental Protection Agency.

EPA (2018), Air Pollutant Emissions Trends Data, edited.

EUMETSAT (2015), GOME_FACTSHEET*Rep.*, 33 pp, Germany.

Fisher, J. A., D. J. Jacob, K. R. Travis, P. S. Kim, E. A. Marais, C. Chan Miller, K. Yu, L. Zhu, R. M. Yantosca, and M. P. Sulprizio (2016), Organic nitrate chemistry and its implications for nitrogen budgets in an isoprene-and monoterpene-rich atmosphere: constraints from aircraft ($SEAC^4RS$) and ground-based (SOAS) observations in the Southeast US, *Atmospheric chemistry and physics*, *16*(9), 5969-5991, doi:10.5194/acp-16-5969-2016.

Frey, M. M., N. Brough, J. L. France, P. S. Anderson, O. Traulle, M. D. King, A. E. Jones, E. W. Wolff, and J. Savarino (2013), The diurnal variability of atmospheric nitrogen oxides (NO and NO_2) above the Antarctic Plateau driven by atmospheric stability and snow emissions, *Atmospheric Chemistry and Physics*, *13*(6), 3045-3062, doi:10.5194/acp-13-3045-2013.

Gao, H. O. (2007), Day of week effects on diurnal ozone/NO_x cycles and transportation emissions in Southern California, *Transportation Research Part D: Transport and Environment*, *12*(4), 292-305, doi:10.1016/j.trd.2007.03.004.

Gaur, A., S. N. Tripathi, V. P. Kanawade, V. Tare, and S. P. Shukla (2014), Four-year measurements of trace gases (SO_2, NO_x, CO, and O_3) at an urban location, Kanpur, in Northern India, *Journal of Atmospheric Chemistry*, *71*(4), 283-301, doi:10.1007/s10874-014-9295-8.

Giangrande, S. E., T. Toto, M. P. Jensen, M. J. Bartholomew, Z. Feng, A. Protat, C. R. Williams, C. Schumacher, and L. Machado (2016), Convective cloud vertical velocity and mass‐flux characteristics from radar wind profiler observations during GoAmazon2014/5, *Journal of Geophysical Research: Atmospheres*, *121*(21), 12,891-812,913, doi:10.1002/2016JD025303.

Glowacz, M., R. Colgan, and D. Rees (2015), Influence of continuous exposure to gaseous ozone on the quality of red bell peppers, cucumbers and zucchini, *Postharvest Biology and Technology*, *99*, 1-8, doi:10.1016/j.postharvbio.2014.06.015.

Greenberg, N., R. S. Carel, E. Derazne, H. Bibi, M. Shpriz, D. Tzur, and B. A. Portnov (2016), Different effects of long-term exposures to SO_2 and NO_2 air pollutants on asthma severity in young adults, *Journal of Toxicology and Environmental Health, Part A*, *79*(8), 342-351, doi:10.1080/15287394.2016.1153548.

Greenberg, N., R. S. Carel, E. Derazne, A. Tiktinsky, D. Tzur, and B. A. Portnov (2017), Modeling long-term effects attributed to nitrogen dioxide (NO_2) and sulfur dioxide (SO_2) exposure on asthma morbidity in a nationwide cohort in Israel, *Journal of Toxicology and Environmental Health, Part A*, *80*(6), 326-337, doi:10.1080/15287394.2017.1313800.

Grewe, V. (2007), Impact of climate variability on tropospheric ozone, *Science of the Total Environment*, *374*(1), 167-181, doi:10.1016/j.scitotenv.2007.01.032.

Gu, D., Y. Wang, C. Smeltzer, and K. F. Boersma (2014), Anthropogenic emissions of NO_x over China: Reconciling the difference of inverse modeling results using GOME‐2 and OMI measurements, *Journal of Geophysical Research: Atmospheres*, *119*(12), 7732-7740, doi:10.1002/2014JD021644.

Gu, D., Y. Wang, C. Smeltzer, and Z. Liu (2013), Reduction in NO_x emission trends over China: Regional and seasonal variations, *Environmental science & technology*, *47*(22), 12912-12919, doi:10.1021/es401727e.

Gu, D., Y. Wang, R. Yin, Y. Zhang, and C. Smeltzer (2016), Inverse modelling of NO_x emissions over eastern China: uncertainties due to chemical non-linearity, *Atmos. Meas. Tech.*, *9*(10), 5193-5201, doi:10.5194/amt-9-5193-2016.

Guenther, A. B., X. Jiang, C. L. Heald, T. Sakulyanontvittaya, T. Duhl, L. K. Emmons, and X. Wang (2012), The Model of Emissions of Gases and Aerosols from Nature version 2.1 (MEGAN2.1): an extended and updated framework for modeling biogenic emissions, doi:10.5194/gmd-5-1471-2012.

Guenther, A. B., T. Karl, P. Harley, C. Wiedinmyer, P. I. Palmer, and C. Geron (2006), Estimates of global terrestrial isoprene emissions using MEGAN (Model of Emissions of Gases and Aerosols from Nature), *Atmospheric Chemistry and Physics*, *6*(11), 3181-3210, doi:10.5194/acp-6-3181-2006.

Hains, J. C., K. F. Boersma, M. Kroon, R. J. Dirksen, R. C. Cohen, A. E. Perring, E. Bucsela, H. Volten, D. P. J. Swart, and A. Richter (2010), Testing and improving OMI DOMINO tropospheric NO_2 using observations from the DANDELIONS and INTEX‐B validation campaigns, *Journal of Geophysical Research: Atmospheres*, *115*(D5), doi:10.1029/2009JD012399.

Hassler, B., B. C. McDonald, G. J. Frost, A. Borbon, D. C. Carslaw, K. Civerolo, C. Granier, P. S. Monks, S. Monks, and D. D. Parrish (2016), Analysis of long‐term observations of NO_x and CO in megacities and application to constraining emissions inventories, *Geophysical Research Letters*, *43*(18), 9920-9930, doi:10.1002/2016GL069894.

Heinrich, J., E. Thiering, P. Rzehak, U. Krämer, M. Hochadel, K. M. Rauchfuss, U. Gehring, and H.-E. Wichmann (2013), Long-term exposure to NO_2 and PM_{10} and all-cause and cause-specific mortality in a prospective cohort of women, *Occup Environ Med*, *70*(3), 179-186, doi:10.1136/oemed-2012-100876.

Herman, J., A. Cede, E. Spinei, G. Mount, M. Tzortziou, and N. Abuhassan (2009), NO_2 column amounts from ground‐based Pandora and MFDOAS spectrometers using the direct‐Sun DOAS technique: Intercomparisons and application to OMI validation, *Journal of Geophysical Research: Atmospheres*, *114*(D13), doi:10.1029/2009JD011848.

Herwehe, J. A., K. Alapaty, T. L. Spero, and C. G. Nolte (2014), Increasing the credibility of regional climate simulations by introducing subgrid‐scale cloud‐radiation interactions, *Journal of Geophysical Research: Atmospheres*, *119*(9), 5317-5330, doi:10.1002/2014JD021504.

Hong, S.-Y., Y. Noh, and J. Dudhia (2006), A new vertical diffusion package with an explicit treatment of entrainment processes, *Monthly weather review*, *134*(9), 2318-2341, doi:10.1175/MWR3199.1.

Hu, X., D. C. Doughty, K. J. Sanchez, E. Joseph, and J. D. Fuentes (2012), Ozone variability in the atmospheric boundary layer in Maryland and its implications for vertical transport model, *Atmospheric Environment*, *46*, 354-364, doi:10.1016/j.atmosenv.2011.09.054.

Hu, X., P. M. Klein, and M. Xue (2013), Evaluation of the updated YSU planetary boundary layer scheme within WRF for wind resource and air quality assessments, *Journal of Geophysical Research: Atmospheres*, *118*(18), 10,490-410,505, doi:10.1002/jgrd.50823.

Hudman, R. C., N. E. Moore, A. K. Mebust, R. V. Martin, A. R. Russell, L. C. Valin, and R. C. Cohen (2012), Steps towards a mechanistic model of global soil nitric oxide emissions: implementation and space based-constraints, *Atmospheric Chemistry and Physics*, *12*(16), 7779-7795, doi:10.5194/acp-12-7779-2012.

Huijnen, V., H. J. Eskes, A. Poupkou, H. Elbern, K. F. Boersma, G. Foret, M. Sofiev, A. Valdebenito, J. Flemming, and O. Stein (2010), Comparison of OMI NO_2 tropospheric columns with an ensemble of global and European regional air quality models, *Atmospheric Chemistry and Physics*, *10*(7), 3273-3296, doi:10.5194/acp-10-3273-2010.

Huntrieser, H., C. Feigl, H. Schlager, F. Schröder, C. Gerbig, P. Van Velthoven, F. Flatøy, C. Théry, A. Petzold, and H. Höller (2002), Airborne measurements of NO_x, tracer species, and small particles during the European Lightning Nitrogen Oxides Experiment, *Journal of Geophysical Research: Atmospheres*, *107*(D11), doi:10.1029/2000JD000209.

Ionov, D. V., Y. M. Timofeyev, V. P. Sinyakov, V. K. Semenov, F. Goutail, J. P. Pommereau, E. J. Bucsela, E. A. Celarier, and M. Kroon (2008), Ground‐based validation of EOS‐Aura OMI NO_2 vertical column data in the midlatitude mountain ranges of Tien Shan (Kyrgyzstan) and Alps (France), *Journal of Geophysical Research: Atmospheres*, *113*(D15), doi:10.1029/2007JD008659.

Irie, H., K. F. Boersma, Y. Kanaya, H. Takashima, X. Pan, and Z. Wang (2012), Quantitative bias estimates for tropospheric NO_2 columns retrieved from SCIAMACHY, OMI, and GOME-2 using a common standard for East Asia, *Atmospheric Measurement Techniques*, *5*(10), 2403-2411, doi:10.5194/amt-5-2403-2012.

Irie, H., Y. Kanaya, H. Akimoto, H. Tanimoto, Z. Wang, J. F. Gleason, and E. J. Bucsela (2008), Validation of OMI tropospheric NO_2 column data using MAX-DOAS measurements deep inside the North China Plain in June 2006: Mount Tai Experiment 2006, *Atmospheric Chemistry and Physics*, *8*(22), 6577-6586, doi:10.5194/acp-8-6577-2008.

Jaeglé, L., L. Steinberger, R. V. Martin, and K. Chance (2005), Global partitioning of NO_x sources using satellite observations: Relative roles of fossil fuel combustion, biomass burning and soil emissions, *Faraday discussions*, *130*, 407-423, doi:10.1039/B502128F.

Jaegle, L., D. J. Jacob, Y. Wang, A. J. Weinheimer, B. A. Ridley, T. L. Campos, G. W. Sachse, and D. E. Hagen (1998), Sources and chemistry of NO_x in the upper troposphere over the United States, *Geophysical Research Letters*, *25*(10), 1705-1708, doi:10.1029/97GL03591.

Jerauld, J., V. Rakov, M. Uman, K. Rambo, D. Jordan, K. Cummins, and J. Cramer (2005), An evaluation of the performance characteristics of the US National Lightning Detection Network in Florida using rocket‐triggered lightning, *Journal of Geophysical Research: Atmospheres*, *110*(D19), doi:10.1029/2005JD005924.

Jerrett, M., R. T. Burnett, C. A. Pope III, K. Ito, G. Thurston, D. Krewski, Y. Shi, E. Calle, and M. Thun (2009), Long-term ozone exposure and mortality, *New England Journal of Medicine*, *360*(11), 1085-1095, doi:10.1056/NEJMoa0803894.

Jiang, Z., B. C. McDonald, H. Worden, J. R. Worden, K. Miyazaki, Z. Qu, D. K. Henze, D. B. A. Jones, A. F. Arellano, and E. V. Fischer (2018), Unexpected slowdown of US pollutant emission reduction in the past decade, *Proceedings of the National Academy of Sciences*, 201801191, doi:10.1073/pnas.1801191115.

Jones, A. E., R. Weller, E. W. Wolff, and H. W. Jacobi (2000), Speciation and rate of photochemical NO and NO_2 production in Antarctic snow, *Geophysical Research Letters*, *27*(3), 345-348, doi:10.1029/1999GL010885.

Kain, J. S. (2004), The Kain–Fritsch convective parameterization: an update, *Journal of Applied Meteorology*, *43*(1), 170-181, doi:10.1175/1520-0450(2004)043<0170:TKCPAU>2.0.CO;2.

Kampa, M., and E. Castanas (2008), Human health effects of air pollution, *Environmental pollution*, *151*(2), 362-367, doi:10.1016/j.envpol.2007.06.012.

Kar, S. K., and Y. A. Liou (2014), Analysis of cloud-to-ground lightning and its relation with surface pollutants over Taipei, Taiwan, paper presented at Annales Geophysicae, Copernicus GmbH.

Karl, T., and W. J. Koss (1984), Regional and national monthly, seasonal, and annual temperature weighted by area, 1895-1983, *Historical climatology series*, *4*(3).

Kaynak, B., Y. Hu, R. V. Martin, C. E. Sioris, and A. G. Russell (2009), Comparison of weekly cycle of NO_2 satellite retrievals and NO_x emission inventories for the continental United States, *Journal of Geophysical Research: Atmospheres*, *114*(D5), doi:10.1029/2008JD010714.

Kebabian, P. L., S. C. Herndon, and A. Freedman (2005), Detection of nitrogen dioxide by cavity attenuated phase shift spectroscopy, *Analytical chemistry*, *77*(2), 724-728, doi:10.1021/ac048715y.

Kleipool, Q. L., M. R. Dobber, J. F. de Haan, and P. F. Levelt (2008), Earth surface reflectance climatology from 3 years of OMI data, *Journal of Geophysical Research: Atmospheres*, *113*(D18), doi:10.1029/2008JD010290.

Koo, J.-H., Y. Wang, T. P. Kurosu, K. Chance, A. Rozanov, A. Richter, S. J. Oltmans, A. M. Thompson, J. W. Hair, and M. A. Fenn (2012), Characteristics of tropospheric ozone depletion events in the Arctic spring: analysis of the ARCTAS, ARCPAC, and ARCIONS measurements and satellite BrO observations, *Atmospheric Chemistry and Physics*, *12*(20), 9909-9922, doi:10.5194/acp-12-9909-2012.

Koshak, W., H. Peterson, A. Biazar, M. Khan, and L. Wang (2014), The NASA Lightning Nitrogen Oxides Model (LNOM): application to air quality modeling, *Atmospheric research*, *135*, 363-369, doi:10.1016/j.atmosres.2012.12.015.

Krotkov, N. A., L. N. Lamsal, E. A. Celarier, W. H. Swartz, S. V. Marchenko, E. J. Bucsela, K. L. Chan, M. Wenig, and M. Zara (2017), The version 3 OMI NO_2 standard product, *Atmospheric Measurement Techniques*, *10*(9), 3133-3149, doi:10.5194/amt-10-3133-2017.

Kumar, V. V., A. Protat, C. Jakob, C. R. Williams, S. Rauniyar, G. L. Stephens, and P. T. May (2016), The estimation of convective mass flux from radar reflectivities, *Journal of Applied Meteorology and Climatology*, *55*(5), 1239-1257, doi:10.1175/JAMC-D-15-0193.1.

Kurzeja, R. J. (1975), The diurnal variation of minor constituents in the stratosphere and its effect on the ozone concentration, *Journal of the Atmospheric Sciences*, *32*(5), 899-909, doi:10.1175/1520-0469(1975)032<0899:TDVOMC>2.0.CO;2.

Lamsal, L. N., B. N. Duncan, Y. Yoshida, N. A. Krotkov, K. E. Pickering, D. G. Streets, and Z. Lu (2015), US NO_2 trends (2005–2013): EPA Air Quality System (AQS) data versus improved observations from the Ozone Monitoring Instrument (OMI), *Atmospheric Environment*, *110*, 130-143, doi:10.1016/j.atmosenv.2015.03.055.

Lamsal, L. N., N. A. Krotkov, E. A. Celarier, W. H. Swartz, K. E. Pickering, E. J. Bucsela, J. F. Gleason, R. V. Martin, S. Philip, and H. Irie (2014), Evaluation of OMI operational standard NO_2 column retrievals using in situ and surface-based NO_2 observations, *Atmospheric Chemistry and Physics*, *14*(21), 11587-11609, doi:10.5194/acp-14-11587-2014.

Lamsal, L. N., R. V. Martin, A. Padmanabhan, A. Van Donkelaar, Q. Zhang, C. E. Sioris, K. Chance, T. P. Kurosu, and M. J. Newchurch (2011), Application of satellite observations for timely updates to global anthropogenic NO_x emission inventories, *Geophysical Research Letters*, *38*(5), doi:10.1029/2010GL046476.

Langford, A. O., K. C. Aikin, C. S. Eubank, and E. J. Williams (2009), Stratospheric contribution to high surface ozone in Colorado during springtime, *Geophysical Research Letters*, *36*(12), doi:10.1029/2009GL038367.

Laughner, J. L., Q. Zhu, and R. C. Cohen (2018), The Berkeley High Resolution Tropospheric NO_2 product, *Earth System Science Data*, *10*(4), 2069-2095, doi:10.5194/essd-10-2069-2018.

Lee, C., R. V. Martin, A. van Donkelaar, A. Richter, J. P. Burrows, and Y. J. Kim (2009), Remote Sensing of Tropospheric Trace Gases (NO_2 and SO_2) from SCIAMACHY, in *Atmospheric and Biological Environmental Monitoring*, edited, pp. 63-72, Springer.

Lei, W., B. de Foy, M. Zavala, R. Volkamer, and L. T. Molina (2007), Characterizing ozone production in the Mexico City Metropolitan Area: a case study using a chemical transport model, *Atmos. Chem. Phys.*, *7*(5), 1347-1366, doi:10.5194/acp-7-1347-2007.

Lei, W., M. Zavala, B. de Foy, R. Volkamer, and L. T. Molina (2008), Characterizing ozone production and response under different meteorological conditions in Mexico City, *Atmos. Chem. Phys.*, *8*(24), 7571-7581, doi:10.5194/acp-8-7571-2008.

Levelt, P. F., E. Hilsenrath, G. W. Leppelmeier, G. H. J. van den Oord, P. K. Bhartia, J. Tamminen, J. F. de Haan, and J. P. Veefkind (2006a), Science objectives of the ozone monitoring instrument, *IEEE Transactions on Geoscience and Remote Sensing*, *44*(5), 1199-1208, doi:10.1109/TGRS.2006.872336.

Levelt, P. F., G. H. J. van den Oord, M. R. Dobber, A. Malkki, H. Visser, J. de Vries, P. Stammes, J. O. V. Lundell, and H. Saari (2006b), The ozone monitoring instrument, *IEEE Transactions on geoscience and remote sensing*, *44*(5), 1093-1101, doi:10.1109/TGRS.2006.872333.

Li, J., J. Mao, A. M. Fiore, R. C. Cohen, J. D. Crounse, A. P. Teng, P. O. Wennberg, B. H. Lee, F. D. Lopez-Hilfiker, and J. A. Thornton (2018), Decadal changes in summertime reactive oxidized nitrogen and surface ozone over the Southeast United States, *Atmospheric Chemistry and Physics*, *18*(3), 2341-2361, doi:10.5194/acp-18-2341-2018.

Li, S., P. C. Harley, and Ü. Niinemets (2017), Ozone‐induced foliar damage and release of stress volatiles is highly dependent on stomatal openness and priming by low‐level ozone exposure in Phaseolus vulgaris, *Plant, cell & environment*, *40*(9), 1984-2003, doi:10.1111/pce.13003.

Liang, S., and Z. Xiao (2012), Global land surface products: Leaf area index product data collection (1985–2010), edited, Beijing Normal University, doi:10.6050/glass863.3004.db.

Liu, Z., Y. Wang, F. Costabile, A. Amoroso, C. Zhao, L. G. Huey, R. Stickel, J. Liao, and T. Zhu (2014), Evidence of aerosols as a media for rapid daytime HONO production over China, *Environmental science & technology*, *48*(24), 14386-14391, doi:10.1021/es504163z.

Liu, Z., Y. Wang, D. Gu, C. Zhao, L. G. Huey, R. Stickel, J. Liao, M. Shao, T. Zhu, and L. Zeng (2012a), Summertime photochemistry during CAREBeijing-2007: RO_x budgets and O_3 formation, *Atmospheric Chemistry and Physics*, *12*(16), 7737-7752, doi:10.5194/acp-12-7737-2012.

Liu, Z., Y. Wang, M. Vrekoussis, A. Richter, F. Wittrock, J. P. Burrows, M. Shao, C. C. Chang, S. C. Liu, and H. Wang (2012b), Exploring the missing source of glyoxal (CHOCHO) over China, *Geophysical Research Letters*, *39*(10), doi:10.1029/2012GL051645.

Luo, C., Y. Wang, and W. J. Koshak (2017), Development of a self‐consistent lightning NO_x simulation in large‐scale 3‐D models, *Journal of Geophysical Research: Atmospheres*, *122*(5), 3141-3154, doi:10.1002/2016JD026225.

Mao, J., F. Paulot, D. J. Jacob, R. C. Cohen, J. D. Crounse, P. O. Wennberg, C. A. Keller, R. C. Hudman, M. P. Barkley, and L. W. Horowitz (2013), Ozone and organic nitrates

over the eastern United States: Sensitivity to isoprene chemistry, *Journal of Geophysical Research: Atmospheres*, *118*(19), 11,256-211,268, doi:10.1002/jgrd.50817.

Marais, E. A., D. J. Jacob, T. P. Kurosu, K. Chance, J. G. Murphy, C. Reeves, G. Mills, S. Casadio, D. B. Millet, and M. P. Barkley (2012), Isoprene emissions in Africa inferred from OMI observations of formaldehyde columns, *Atmospheric Chemistry and Physics*, *12*(14), 6219-6235, doi:10.5194/acp-12-6219-2012.

Marchenko, S., N. A. Krotkov, L. N. Lamsal, E. A. Celarier, W. H. Swartz, and E. J. Bucsela (2015), Revising the slant column density retrieval of nitrogen dioxide observed by the Ozone Monitoring Instrument, *Journal of Geophysical Research: Atmospheres*, *120*(11), 5670-5692, doi:10.1002/2014JD022913.

Marr, L. C., T. O. Moore, M. E. Klapmeyer, and M. B. Killar (2013), Comparison of NO_x Fluxes Measured by Eddy Covariance to Emission Inventories and Land Use, *Environmental science & technology*, *47*(4), 1800-1808, doi:10.1021/es303150y.

Mazzuca, G. M., X. Ren, C. P. Loughner, M. Estes, J. H. Crawford, K. E. Pickering, A. J. Weinheimer, and R. R. Dickerson (2016), Ozone production and its sensitivity to NO_x and VOCs: results from the DISCOVER-AQ field experiment, Houston 2013, *Atmos. Chem. Phys.*, *16*(22), 14463-14474, doi:10.5194/acp-16-14463-2016.

McDonald, B., S. McKeen, Y. Y. Cui, R. Ahmadov, S.-W. Kim, G. J. Frost, I. Pollack, J. Peischl, T. B. Ryerson, and J. Holloway (2018), Modeling Ozone in the Eastern US using a Fuel-Based Mobile Source Emissions Inventory, *Environmental science & technology*, doi:10.1021/acs.est.8b00778.

Millet, D. B., D. J. Jacob, K. F. Boersma, T. M. Fu, T. P. Kurosu, K. Chance, C. L. Heald, and A. Guenther (2008), Spatial distribution of isoprene emissions from North America derived from formaldehyde column measurements by the OMI satellite sensor, *Journal of Geophysical Research: Atmospheres*, *113*(D2), doi:10.1029/2007JD008950.

Miyazaki, K., H. Eskes, K. Sudo, K. F. Boersma, K. Bowman, and Y. Kanaya (2017), Decadal changes in global surface NO_x emissions from multi-constituent satellite data assimilation, *Atmos. Chem. Phys*, *17*(2), 807-837, doi:10.5194/acp-17-807-2017.

Miyazaki, K., H. Eskes, K. Sudo, and C. Zhang (2014), Global lightning NO_x production estimated by an assimilation of multiple satellite data sets, *Atmospheric Chemistry and Physics*, *14*(7), 3277-3305, doi:10.5194/acp-14-3277-2014.

Mrowiec, A. A., C. Rio, A. M. Fridlind, A. S. Ackerman, A. D. Del Genio, O. M. Pauluis, A. C. Varble, and J. Fan (2012), Analysis of cloud‐resolving simulations of a tropical mesoscale convective system observed during TWP‐ICE: Vertical fluxes and draft properties in convective and stratiform regions, *Journal of Geophysical Research: Atmospheres*, *117*(D19), doi:10.1029/2012JD017759.

Munro, R., M. Eisinger, C. Anderson, J. Callies, E. Corpaccioli, R. Lang, A. Lefebvre, Y. Livschitz, and A. P. Albinana (2006), GOME-2 on MetOp, paper presented at Proc. of The 2006 EUMETSAT Meteorological Satellite Conference, Helsinki, Finland.

Musselman, R. C., and J. L. Korfmacher (2014), Ozone in remote areas of the Southern Rocky Mountains, *Atmospheric environment*, *82*, 383-390, doi:10.1016/j.atmosenv.2013.10.051.

Myhre, G., et al. (2013), Anthropogenic and natural radiative forcing, in *Climate change 2013: The Physical Science Basis. Contribution of Working Group I to the Fifth Assessment Report of the Intergovernmental Panel on Climate Change*, edited, pp. 659-740, Cambridge University Press, Cambridge, United Kingdom and New York, NY, USA.

Nag, A., S. Mallick, V. Rakov, J. Howard, C. Biagi, J. Hill, M. Uman, D. Jordan, K. Rambo, and J. Jerauld (2011), Evaluation of US National Lightning Detection Network performance characteristics using rocket‐triggered lightning data acquired in 2004–2009, *Journal of Geophysical Research: Atmospheres*, *116*(D2), doi:10.1029/2010JD014929.

Newman, A. J., M. P. Clark, J. Craig, B. Nijssen, A. Wood, E. Gutmann, N. Mizukami, L. Brekke, and J. R. Arnold (2015), Gridded ensemble precipitation and temperature estimates for the contiguous United States, *Journal of Hydrometeorology*, *16*(6), 2481-2500, doi:10.1175/JHM-D-15-0026.1.

Ng, N. L., S. S. Brown, A. T. Archibald, E. Atlas, R. C. Cohen, J. N. Crowley, D. A. Day, N. M. Donahue, J. L. Fry, and H. Fuchs (2017), Nitrate radicals and biogenic volatile organic compounds: oxidation, mechanisms, and organic aerosol, *Atmospheric Chemistry and Physics*, *17*(3), 2103-2162, doi:10.5194/acp-17-2103-2017.

Oetjen, H., S. Baidar, N. A. Krotkov, L. N. Lamsal, M. Lechner, and R. Volkamer (2013), Airborne MAX‐DOAS measurements over California: Testing the NASA OMI tropospheric NO_2 product, *Journal of Geophysical Research: Atmospheres*, *118*(13), 7400-7413, doi:10.1002/jgrd.50550.

Ott, L. E., K. E. Pickering, G. L. Stenchikov, D. J. Allen, A. J. DeCaria, B. Ridley, R. F. Lin, S. Lang, and W. K. Tao (2010), Production of lightning NO_x and its vertical distribution calculated from three‐dimensional cloud‐scale chemical transport model simulations, *Journal of Geophysical Research: Atmospheres*, *115*(D4), doi:10.1029/2009JD011880.

Palmer, P. I., D. J. Jacob, A. M. Fiore, R. V. Martin, K. Chance, and T. P. Kurosu (2003), Mapping isoprene emissions over North America using formaldehyde column observations from space, *Journal of Geophysical Research: Atmospheres*, *108*(D6), doi:10.1029/2002JD002153.

Pandey, J. S., R. Kumar, and S. Devotta (2005), Health risks of NO_2, SPM and SO_2 in Delhi (India), *Atmospheric Environment*, *39*(36), 6868-6874, doi:10.1016/j.atmosenv.2005.08.004.

Parsons, T. L. (2000), Determining the horizontal distance distribution of cloud-to-ground lightning*Rep.*, AIR FORCE INST OF TECH WRIGHT-PATTERSONAFB OH SCHOOL OF ENGINEERING.

Peng, J., M. Hu, S. Guo, Z. Du, J. Zheng, D. Shang, M. L. Zamora, L. Zeng, M. Shao, and Y.-S. Wu (2016), Markedly enhanced absorption and direct radiative forcing of black carbon under polluted urban environments, *Proceedings of the National Academy of Sciences*, 201602310, doi:10.1073/pnas.1602310113.

Peters, E., F. Wittrock, K. Großmann, U. Frieß, A. Richter, and J. P. Burrows (2012), Formaldehyde and nitrogen dioxide over the remote western Pacific Ocean: SCIAMACHY and GOME-2 validation using ship-based MAX-DOAS observations, *Atmospheric Chemistry and Physics*, *12*(22), 11179-11197, doi:10.5194/acp-12-11179-2012.

Pickering, K. E., Y. Wang, W. K. Tao, C. Price, and J. F. Müller (1998), Vertical distributions of lightning NO_x for use in regional and global chemical transport models, *Journal of Geophysical Research: Atmospheres*, *103*(D23), 31203-31216, doi:10.1029/98JD02651.

Pierce, T., C. Geron, L. Bender, R. Dennis, G. Tonnesen, and A. Guenther (1998), Influence of increased isoprene emissions on regional ozone modeling, *Journal of Geophysical Research: Atmospheres*, *103*(D19), 25611-25629, doi:10.1029/98JD01804.

Rasool, Q. Z., R. Zhang, B. Lash, D. S. Cohan, E. J. Cooter, J. O. Bash, and L. N. Lamsal (2016), Enhanced representation of soil NO emissions in the Community Multiscale Air Quality (CMAQ) model version 5.0.2, *Geosci. Model Dev.*, *9*(9), 3177-3197, doi:10.5194/gmd-9-3177-2016.

Reddy, B. S. K., K. R. Kumar, G. Balakrishnaiah, K. R. Gopal, R. R. Reddy, V. Sivakumar, A. P. Lingaswamy, S. M. Arafath, K. Umadevi, and S. P. Kumari (2012), Analysis of diurnal and seasonal behavior of surface ozone and its precursors (NO_x) at a semi-arid rural site in Southern India, *Aerosol Air Qual Res*, *12*, 1081-1094, doi:10.4209/aaqr.2012.03.0055.

Reed, A. J., A. M. Thompson, D. E. Kollonige, D. K. Martins, M. A. Tzortziou, J. R. Herman, T. A. Berkoff, N. K. Abuhassan, and A. Cede (2015), Effects of local meteorology and aerosols on ozone and nitrogen dioxide retrievals from OMI and pandora spectrometers in Maryland, USA during DISCOVER-AQ 2011, *Journal of atmospheric chemistry*, *72*(3-4), 455-482, doi:10.1007/s10874-013-9254-9.

Reed, C., M. J. Evans, P. D. Carlo, J. D. Lee, and L. J. Carpenter (2016), Interferences in photolytic NO_2 measurements: explanation for an apparent missing oxidant?, *Atmospheric Chemistry and Physics*, *16*(7), 4707-4724, doi:10.5194/acp-16-4707-2016.

Richter, A., M. Begoin, A. Hilboll, and J. P. Burrows (2011), An improved NO_2 retrieval for the GOME-2 satellite instrument, *Atmospheric Measurement Techniques*, *4*(6), 1147-1159, doi:10.5194/amt-4-1147-2011.

Romps, D. M., J. T. Seeley, D. Vollaro, and J. Molinari (2014), Projected increase in lightning strikes in the United States due to global warming, *Science*, *346*(6211), 851-854, doi:10.1126/science.1259100.

Russell, A. R., L. C. Valin, and R. C. Cohen (2012), Trends in OMI NO_2 observations over the United States: effects of emission control technology and the economic recession, *Atmospheric Chemistry and Physics*, *12*(24), 12197-12209, doi:10.5194/acp-12-12197-2012.

Saha, S., S. Moorthi, X. Wu, J. Wang, S. Nadiga, P. Tripp, D. Behringer, Y. T. Hou, H.-y. Chuang, and M. Iredell (2011), NCEP climate forecast system version 2 (CFSv2) 6-hourly products, edited, Research Data Archive at the National Center for Atmospheric Research, Computational and Information Systems Laboratory, doi:10.5065/D61C1TXF.

Salmon, O., P. Shepson, X. Ren, H. He, D. Hall, R. Dickerson, B. Stirm, S. Brown, D. Fibiger, and E. McDuffie (2018), Top‐down Estimates of NO_x and CO Emissions from Washington, DC‐Baltimore During the WINTER Campaign, *Journal of Geophysical Research: Atmospheres*, doi:10.1029/2018JD028539.

Sawamura, P., D. Müller, R. M. Hoff, C. A. Hostetler, R. A. Ferrare, J. W. Hair, R. R. Rogers, B. E. Anderson, L. D. Ziemba, and A. J. Beyersdorf (2014), Aerosol optical and microphysical retrievals from a hybrid multiwavelength lidar data set–DISCOVER-AQ 2011, *Atmospheric Measurement Techniques*, *7*(9), 3095-3112, doi:10.5194/amt-7-3095-2014.

Schumann, U., and H. Huntrieser (2007), The global lightning-induced nitrogen oxides source, *Atmos. Chem. Phys.*, *7*(14), 3823-3907, doi:10.5194/acp-7-3823-2007.

Seinfeld, J. H., and S. N. Pandis (2016), *Atmospheric chemistry and physics: from air pollution to climate change*, John Wiley & Sons, Inc, Hoboken,New Jersey.

Sen, B., G. C. Toon, G. B. Osterman, J.-F. Blavier, J. J. Margitan, R. J. Salawitch, and G. K. Yue (1998), Measurements of reactive nitrogen in the stratosphere, *Journal of Geophysical Research: Atmospheres*, *103*(D3), 3571-3585, doi:10.1029/97JD02468.

Shim, C., Y. Wang, Y. Choi, P. I. Palmer, D. S. Abbot, and K. Chance (2005), Constraining global isoprene emissions with Global Ozone Monitoring Experiment

(GOME) formaldehyde column measurements, *Journal of Geophysical Research: Atmospheres*, *110*(D24), doi:10.1029/2004JD005629.

Shin, H. H., and S.-Y. Hong (2011), Intercomparison of planetary boundary-layer parametrizations in the WRF model for a single day from CASES-99, *Boundary-Layer Meteorology*, *139*(2), 261-281, doi:10.1007/s10546-010-9583-z.

Singh, A., and M. Agrawal (2007), Acid rain and its ecological consequences, *Journal of Environmental Biology*, *29*(1), 15.

Spinei, E., A. Cede, W. H. Swartz, J. Herman, and G. H. Mount (2014), The use of NO_2 absorption cross section temperature sensitivity to derive NO_2 profile temperature and stratospheric–tropospheric column partitioning from visible direct-sun DOAS measurements, *Atmospheric Measurement Techniques*, *7*(12), 4299-4316, doi:10.5194/amt-7-4299-2014.

Stavrakou, T., J.-F. Müller, M. Bauwens, I. De Smedt, M. Van Roozendael, A. Guenther, M. Wild, and X. Xia (2014), Isoprene emissions over Asia 1979–2012: impact of climate and land-use changes, *Atmospheric Chemistry and Physics*, *14*(9), 4587-4605, doi:10.5194/acp-14-4587-2014.

Stavrakou, T., J.-F. Müller, I. De Smedt, M. V. Roozendael, G. Van Der Werf, L. Giglio, and A. Guenther (2009), Evaluating the performance of pyrogenic and biogenic emission inventories against one decade of space-based formaldehyde columns, *Atmospheric Chemistry and Physics*, *9*(3), 1037-1060, doi:10.5194/acp-9-1037-2009.

Tilstra, L. G., O. N. E. Tuinder, P. Wang, and P. Stammes (2017), Surface reflectivity climatologies from UV to NIR determined from Earth observations by GOME‐2 and SCIAMACHY, *Journal of Geophysical Research: Atmospheres*, *122*(7), 4084-4111, doi:10.1002/2016JD025940.

Tong, D., L. Lamsal, L. Pan, C. Ding, H. Kim, P. Lee, T. Chai, K. E. Pickering, and I. Stajner (2015), Long-term NO_x trends over large cities in the United States during the great recession: Comparison of satellite retrievals, ground observations, and emission inventories, *Atmospheric Environment*, *107*, 70-84, doi:10.1016/j.atmosenv.2015.01.035.

Travis, K. R., D. J. Jacob, J. A. Fisher, P. S. Kim, E. A. Marais, L. Zhu, K. Yu, C. C. Miller, R. M. Yantosca, and M. P. Sulprizio (2016), Why do models overestimate surface ozone in the Southeast United States?, *Atmospheric chemistry and physics*, *16*(21), 13561-13577, doi:10.5194/acp-16-13561-2016.

Tsai, C., C. Wong, S. Hurlock, O. Pikelnaya, L. H. Mielke, H. D. Osthoff, J. H. Flynn, C. Haman, B. Lefer, and J. Gilman (2014), Nocturnal loss of NO_x during the 2010 CalNex‐LA study in the Los Angeles Basin, *Journal of Geophysical Research: Atmospheres*, *119*(22), 13,004-013,025, doi:10.1002/2014JD022171.

Tu, J., Z.-G. Xia, H. Wang, and W. Li (2007), Temporal variations in surface ozone and its precursors and meteorological effects at an urban site in China, *Atmospheric Research*, *85*(3-4), 310-337, doi:10.1016/j.atmosres.2007.02.003.

Turner, M. C., M. Jerrett, C. A. Pope III, D. Krewski, S. M. Gapstur, W. R. Diver, B. S. Beckerman, J. D. Marshall, J. Su, and D. L. Crouse (2016), Long-term ozone exposure and mortality in a large prospective study, *American journal of respiratory and critical care medicine*, *193*(10), 1134-1142, doi:10.1164/rccm.201508-1633OC.

VAISALA (2015), Vaisala's NLDN®U.S. National Lightning Detection Network*Rep.*

van der A, R. J., H. J. Eskes, M. V. Roozendael, I. De Smedt, N. Blond, F. Boersma, A. Weiss, and J. C. A. van Peet (2010), Algorithm Document Tropospheric NO_2*Rep. 1.0*, 23 pp.

Van Stratum, B. J. H., J. Vilà-Guerau de Arellano, H. G. Ouwersloot, K. d. Dries, T. W. Van Laar, M. Martinez, J. Lelieveld, J.-M. Diesch, F. Drewnick, and H. Fischer (2012), Case study of the diurnal variability of chemically active species with respect to boundary layer dynamics during DOMINO, *Atmospheric Chemistry and Physics*, *12*(12), 5329-5341, doi:10.5194/acp-12-5329-2012.

Veefkind, J. P., J. F. de Haan, M. Sneep, and P. F. Levelt (2016), Improvements to the OMI O_2–O_2 operational cloud algorithm and comparisons with ground-based radar–lidar observations, *Atmos. Meas. Tech.*, *9*(12), 6035-6049, doi:10.5194/amt-9-6035-2016.

Wang, L., M. B. Follette-Cook, M. J. Newchurch, K. E. Pickering, A. Pour-Biazar, S. Kuang, W. Koshak, and H. Peterson (2015), Evaluation of lightning-induced tropospheric ozone enhancements observed by ozone lidar and simulated by WRF/Chem, *Atmospheric Environment*, *115*, 185-191, doi:10.1016/j.atmosenv.2015.05.054.

Wang, L., M. Newchurch, A. Pour-Biazar, S. Kuang, M. Khan, X. Liu, W. Koshak, and K. Chance (2013), Estimating the influence of lightning on upper tropospheric ozone using NLDN lightning data and CMAQ model, *Atmospheric environment*, *67*, 219-228, doi:10.1016/j.atmosenv.2012.11.001.

Wang, P., P. Stammes, R. van der A, G. Pinardi, and M. van Roozendael (2008), FRESCO+: an improved O_2 A-band cloud retrieval algorithm for tropospheric trace gas retrievals, *Atmos. Chem. Phys.*, *8*(21), 6565-6576, doi:10.5194/acp-8-6565-2008.

Wang, Y., S. Beirle, J. Lampel, M. Koukouli, I. De Smedt, N. Theys, L. Ang, D. Wu, P. Xie, and C. Liu (2017), Validation of OMI, GOME-2A and GOME-2B tropospheric NO_2, SO_2 and HCHO products using MAX-DOAS observations from 2011 to 2014 in Wuxi, China: investigation of the effects of priori profiles and aerosols on the satellite products, *Atmospheric Chemistry and Physics*, *17*(8), 5007, doi:10.5194/acp-17-5007-2017.

Wang, Y., Y. Choi, T. Zeng, D. Davis, M. Buhr, L. G. Huey, and W. Neff (2007), Assessing the photochemical impact of snow NO_x emissions over Antarctica during ANTCI 2003, *Atmospheric Environment*, *41*(19), 3944-3958, doi:10.1016/j.atmosenv.2007.01.056.

Weinmayr, G., E. Romeo, M. De Sario, S. K. Weiland, and F. Forastiere (2009), Short-term effects of PM_{10} and NO_2 on respiratory health among children with asthma or asthma-like symptoms: a systematic review and meta-analysis, *Environmental health perspectives*, *118*(4), 449-457, doi:10.1289/ehp.0900844.

Williams, J. E., K. F. Boersma, P. L. Sager, and W. W. Verstraeten (2017), The high-resolution version of TM5-MP for optimized satellite retrievals: description and validation, *Geoscientific Model Development*, *10*(2), 721-750, doi:10.5194/gmd-10-721-2017.

Williams, J. E., M. P. Scheele, P. F. J. van Velthoven, J.-P. Cammas, V. Thouret, C. Galy-Lacaux, and A. Volz-Thomas (2009), The influence of biogenic emissions from Africa on tropical tropospheric ozone during 2006: a global modeling study, *Atmospheric Chemistry and Physics*, *9*(15), 5729-5749, doi:10.5194/acp-9-5729-2009.

Wolfe, G. M., T. F. Hanisco, H. L. Arkinson, T. P. Bui, J. D. Crounse, J. Dean‐Day, A. Goldstein, A. Guenther, S. R. Hall, and G. Huey (2015), Quantifying sources and sinks of reactive gases in the lower atmosphere using airborne flux observations, *Geophysical Research Letters*, *42*(19), 8231-8240, doi:10.1002/2015GL065839.

Xiao, Z., S. Liang, J. Wang, P. Chen, X. Yin, L. Zhang, and J. Song (2014), Use of general regression neural networks for generating the GLASS leaf area index product from time-series MODIS surface reflectance, *IEEE Transactions on Geoscience and Remote Sensing*, *52*(1), 209-223, doi:10.1109/TGRS.2013.2237780.

Xie, Y., R. Elleman, T. Jobson, and B. Lamb (2011), Evaluation of O_3‐NO_x‐VOC sensitivities predicted with the CMAQ photochemical model using Pacific Northwest 2001 field observations, *Journal of Geophysical Research: Atmospheres*, *116*(D20), doi:10.1029/2011JD015801.

Xing, J., J. Pleim, R. Mathur, G. Pouliot, C. Hogrefe, C. M. Gan, and C. Wei (2013), Historical gaseous and primary aerosol emissions in the United States from 1990 to 2010, *Atmos. Chem. Phys.*, *13*(15), 7531-7549, doi:10.5194/acp-13-7531-2013.

Yang, J., Z. Wang, A. J. Heymsfield, and J. R. French (2016), Characteristics of vertical air motion in isolated convective clouds, *Atmos. Chem. Phys.*, *16*(15), 10159-10173, doi:10.5194/acp-16-10159-2016.

Yang, Q., Y. Wang, C. Zhao, Z. Liu, W. I. Gustafson Jr, and M. Shao (2011), NO_x emission reduction and its effects on ozone during the 2008 Olympic Games, *Environmental science & technology*, *45*(15), 6404-6410, doi:10.1021/es200675v.

Yienger, J. J., and H. Levy (1995), Empirical model of global soil‐biogenic NO_x emissions, *Journal of Geophysical Research: Atmospheres*, *100*(D6), 11447-11464, doi:10.1029/95JD00370.

Yu, K., D. J. Jacob, J. A. Fisher, P. S. Kim, E. A. Marais, C. C. Miller, K. R. Travis, L. Zhu, R. M. Yantosca, and M. P. Sulprizio (2016), Sensitivity to grid resolution in the ability of a chemical transport model to simulate observed oxidant chemistry under high-isoprene conditions, *Atmospheric Chemistry and Physics*, *16*(7), 4369-4378, doi:10.5194/acp-16-4369-2016.

Zara, M., K. F. Boersma, I. De Smedt, A. Richter, E. Peters, J. H. G. M. Van Geffen, S. Beirle, T. Wagner, M. Van Roozendael, and S. Marchenko (2018), Improved slant column density retrieval of nitrogen dioxide and formaldehyde for OMI and GOME-2A from QA4ECV: intercomparison, uncertainty characterization, and trends, *Meas. Tech. Discuss*, 1-47, doi:10.5194/amt-11-4033-2018.

Zhang, R., A. Cohan, A. P. Biazar, and D. S. Cohan (2017a), Source apportionment of biogenic contributions to ozone formation over the United States, *Atmospheric environment*, *164*, 8-19, doi:10.1016/j.atmosenv.2017.05.044.

Zhang, R., Y. Wang, Q. He, L. Chen, Y. Zhang, H. Qu, C. Smeltzer, J. Li, L. Alvarado, and M. Vrekoussis (2017b), Enhanced trans-Himalaya pollution transport to the Tibetan Plateau by cut-off low systems, *Atmospheric Chemistry and Physics*, *17*(4), 3083-3095, doi:10.5194/acp-17-3083-2017.

Zhang, R., Y. Wang, C. Smeltzer, H. Qu, W. Koshak, and K. F. Boersma (2018), Comparing OMI-based and EPA AQS in situ NO_2 trends: towards understanding surface NO_x emission changes, *Atmospheric Measurement Techniques*, *11*(7), 3955-3967, doi:10.5194/amt-11-3955-2018.

Zhang, Y., and Y. Wang (2016), Climate-driven ground-level ozone extreme in the fall over the Southeast United States, *Proceedings of the National Academy of Sciences*, *113*(36), 10025-10030, doi:10.1073/pnas.1602563113.

Zhang, Y., Y. Wang, G. Chen, C. Smeltzer, J. Crawford, J. Olson, J. Szykman, A. J. Weinheimer, D. J. Knapp, and D. D. Montzka (2016), Large vertical gradient of reactive nitrogen oxides in the boundary layer: Modeling analysis of DISCOVER‐AQ 2011 observations, *Journal of Geophysical Research: Atmospheres*, *121*(4), 1922-1934, doi:10.1002/2015JD024203.

Zhao, B., K.-N. Liou, Y. Gu, C. He, W.-L. Lee, X. Chang, Q. Li, S. Wang, H.-L. R. Tseng, and L.-Y. R. Leung (2016), Impact of buildings on surface solar radiation over urban Beijing, *Atmospheric Chemistry and Physics*, *16*(9), 5841-5852, doi:10.5194/acp-16-5841-2016.

Zhao, C., and Y. Wang (2009), Assimilated inversion of NO_x emissions over east Asia using OMI NO_2 column measurements, *Geophysical Research Letters*, *36*(6), doi:10.1029/2008GL037123.

Zhao, C., Y. Wang, Y. Choi, and T. Zeng (2009a), Summertime impact of convective transport and lightning NO_x production over North America: modeling dependence on meteorological simulations, *Atmospheric Chemistry and Physics*, *9*(13), 4315-4327, doi:10.5194/acp-9-4315-2009.

Zhao, C., Y. Wang, Q. Yang, R. Fu, D. Cunnold, and Y. Choi (2010), Impact of East Asian summer monsoon on the air quality over China: View from space, *Journal of Geophysical Research: Atmospheres*, *115*(D9), doi:10.1029/2009JD012745.

Zhao, C., Y. Wang, and T. Zeng (2009b), East China plains: A "basin" of ozone pollution, *Environmental science & technology*, *43*(6), 1911-1915, doi:10.1021/es8027764.

Zheng, Y., K. Alapaty, J. A. Herwehe, A. D. Del Genio, and D. Niyogi (2016), Improving high-resolution weather forecasts using the Weather Research and Forecasting (WRF) Model with an updated Kain–Fritsch scheme, *Monthly Weather Review*, *144*(3), 833-860, doi:10.1175/MWR-D-15-0005.1.

Zhu, L., D. J. Jacob, P. S. Kim, J. A. Fisher, K. Yu, K. R. Travis, L. J. Mickley, R. M. Yantosca, M. P. Sulprizio, and I. De Smedt (2016), Observing atmospheric formaldehyde (HCHO) from space: validation and intercomparison of six retrievals from four satellites (OMI, GOME2A, GOME2B, OMPS) with SEAC^{4}RS aircraft observations over the southeast US, *Atmospheric chemistry and physics*, *16*(21), 13477-13490, doi:10.5194/acp-16-13477-2016.